博 士 論 文

Study of finite-difference time-domain analysis on sound fields
with porous materials
（多孔質材料を有する音場の時間領域有限差分解析に関する研究）

趙 静

Abstract

In this dissertation, a finite-difference time-domain algorithm based on the equivalent fluid model (EF-FDTD algorithm) is developed to study the sound fields containing porous material.

In the porous material with rigid flame, the mechanism for the sound attenuated in the porous material is by the viscous losses and thermal losses in the porous material. In the frequency-domain equations based on the equivalent fluid model, the effective bulk modulus corresponds to the thermal effects in the porous material, and the effective density corresponds to the viscous effects in the porous material. In the porous material, the effective density and the effective bulk modulus are frequency dependent, which are designed in the form of the IIR filter. By applying the Z-transform theory, the whole wave equations (containing add operation, multiplication operation and frequency dependent parameters) are transformed to Z domain, avoiding the complex convolution operation in time domain. In Z domain, the add operation and the multiplication operation are not changed. New parameters are defined, which greatly simplified the equations in Z domain. The simplified equations and the defined parameters can be easily transformed to time domain, and formulations of the EF-FDTD algorithm are obtained. In EF-FDTD algorithm, the thermal effects in the porous material are reflected by the parameters of the designed IIR filters of the effective bulk modulus. The viscous effects in the porous material are reflected by the parameters of the designed IIR filters the effective density. Once the IIR filters are designed, there is no need to design them again if the discrete time interval in the FDTD analysis is changed.

The formulations for the 1-dimensional EF-FDTD algorithm, 2-dimensional EF-FDTD algorithm and 3-dimensional EF-FDTD algorithm are presented in this dissertation. The stability conditions for the EF-FDTD algorithm are discussed.

The 1-dimensional EF-FDTD algorithm is validated under the normal incidence of the sound by comparing the numerical analysis and the experiment. In the simulation, the boundary conditions (the boundary between air and the porous material, the boundary between different porous materials) are mainly discussed. The arithmetic averaged density at the boundary is used. The calculated sound absorption coefficients of the constructed multi-layered porous material agree well to the measured values.

The 2-dimensional EF-FDTDT algorithm is validated under the oblique incidence of the sound by comparing the numerical analysis and the theoretical values. 4 regular cases of the common relative position of the porous material and the air are simulated. The methods for calculating the surface impedance for each case are discussed. The calculated surface impedances of the multi-layered porous material are very close to the theoretical values in broad frequency range.

The shaped porous material is simulated by using staircase approximation. In 2-dimensional sound field, the errors caused by using the staircase approximation are discussed. The smaller the discrete space interval is, the smaller the error introduced by the staircase approximation is.

The 2-dimensional EF-FDTDT algorithm is contrasted with the exiting Rayleigh method. The 2-dimensional EF-FDTD method is accurate in broad frequency range either at small incident angle or big incident angle. For the Rayleigh method, the errors between the calculated absorption coefficients and the theoretical values are very large.

Porous materials are commonly used to construct absorbing wedges in anechoic chambers. The method for predicting the absorption coefficient of the wedges by using 2-dimensioal EF-FDTD algorithm is discussed. For the 4 kinds of designed wedges, the calculated absorption coefficient is very close to the measured values.

Contents

List of Figures

List of Tables

Chapter 1 INTRODUCTION

1.1 Research background

With the improvement of the living standard in people's life, and with the increasing awareness of environmental protection, people pay more and more attention to the noise problems in living and working environment. The methods to control the noise are mainly from three aspects: noise source itself, the way in which the noise is transmitted and the person who receive the noise. According to the different control objects, active noise control methods and passive noise control methods are used separately. Passive noise control is adopted in the channels and media of noise propagation. Then the noise emitted by the noise source is suppressed and reduced in the process of transmission. The measures taken mainly include two aspects: sound absorption methods and sound insulation methods. Porous materials are effective in the noise reduction techniques for the merits of cheap price, easy to be processed and most importantly, the excellent broadband absorption characteristics.

When analyze the sound field containing porous materials, 3 major wave based numerical methods are exist: the finite element method (FEM), the boundary element method (BEM) and the finite difference time domain method (FDTD). Each method has its own advantages and disadvantages. FDTD method is a time domain method, simulating sound wave propagation in time domain. One advantage of FDTD method is effective in dealing with complicated time domain phenomena, such as sound diffraction, sound reflection and sound scattering. The FDTD method was firstly developed in the study fields of electromagnetics[1-7]. Then the FDTD method began to be used in various acoustical fields, such as ultrasonic[8], underwater sound[9], architectural acoustics[10-20], etc.

As mentioned above, porous materials are frequently used in many places. When simulating the sound field containing porous material by using the FDTD method, one difficult point is explained as follows. FDTD method is a time domain method. However, the characters of the porous material (such as sound absorption coefficient, reflection coefficient) are frequency dependent. Therefore, it is difficult to introduce the frequency character of the porous material in FDTD method in the time domain.

In order to solve this problem (accurately simulate the frequency character of the porous material in FDTD algorithm), some works have been published which are introduced as follows.

In some cases, a porous material can be treated as locally-reactive. Based on the local-reactive assumption, only the sound pressure and the particle velocity in front of the boundary surface are used. The sound pressures and the particle velocities in the porous material are neglected. The normal components of the particle velocity u_n at the boundary and the related sound pressure p in front of the boundary are connected by the surface impedance Z_s:

$$Z_s = \frac{p}{u_n}. \tag{1.1}$$

The surface impedance Z_s is the complex value. If the surface impedance Z_s can be treated appropriately, then the frequency character of the porous material can be simulated in the FDTD algorithm.

In the work by Yokota[16], sound propagating in 2-dimensional sound field (with the shape of concert halls) is visualized by using FDTD algorithm. In the simulation, the normal incident absorption coefficient α is used to calculate the surface impedance Z_s[16],

$$Z_s = \rho_0 c_0 \frac{1+\sqrt{1-\alpha}}{1-\sqrt{1-\alpha}}, \tag{1.2}$$

where ρ_0 is the density of the air, and c_0 is the sound speed in the air.

By using Eq.(1.2), the result of Z_s is a real value. Multiple computational calculations are needed at the whole frequency range, requiring large amount of computing time.

Chiba and Kashiwa[10] developed a method in which the surface impedance Z_s is modeled by an equivalent RCL circuit, in which the required frequency characteristics can be designed.

Botteldooren[12] studied the low frequency and middle frequency room acoustical problems by using the FDTD algorithm. When treat the boundary conditions, a simple frequency function is proposed to simulate the surface impedance Z_s.

$$Z_s = \frac{Z_{-1}}{j\omega} + Z_0 + j\omega Z_1, \tag{1.3}$$

where Z_{-1}, Z_0 and Z_1 are real constants to be decided.

Sakamoto[18] calculated the impulse response in a hall by using the FDTD algorithm. When treat the boundary conditions, the surface impedance Z_s is simulated by the equivalent mechanical system with different degrees of freedom. For the equivalent mechanical system with one degree of freedom, Z_s is expressed as:

$$Z_s = c_1 + j\left(m_1\omega - \frac{k_1}{\omega}\right), \tag{1.4}$$

where c_1 is the resistance coefficient of the system, m_1 is the mass, and k_1 is the stiffness of the spring.

In some works[21-22], the admittance can be designed as the finite impulse response (FIR) filter. Applying the Z transform theory, the equation in Z domain is obtained:

$$A(\omega) = \frac{1}{Z(\omega)} = \frac{u(\omega)}{p(\omega)}, \tag{1.5}$$

$$A(z) = a_0 + a_1 z^{-1} + a_2 z^{-2} + \cdots + a_N z^{-N}. \tag{1.6}$$

In Eq.(1.6), z^{-1} in Z domain represents one time step delay in time domain. Then the relationship between the sound pressure and the particle velocity in FDTD algorithm can be obtained:

$$u^{n+1} = a_0 p^{n+1/2} + a_1 p^{n-1/2} + \cdots + a_N p^{n-(N-1/2)}. \tag{1.7}$$

When simulate the frequency character of the admittance using the FIR filter, the order of the filter (N) is usually very large. Then in the FDTD analysis, the occupied memory in the computer and the calculation time become larger. As another treatment, an infinite impulse response (IIR) filter can be used. By using the IIR filter[22-23], the order of the filter (N) becomes smaller, reducing the occupied memory in the computer and the calculation time.

The admittance designed as infinite impulse filter (IIR) in Z domain. Applying the Z transform theory, the equation in Z domain can be obtained:

$$A(z) = \frac{\sum_{n=0}^{N} a_n z^{-n}}{1 + \sum_{m=1}^{M} b_m z^{-m}}. \tag{1.8}$$

In Eq.(1.8), z^{-1} in Z domain represents one time step delay in time domain. Then the relationship between the sound pressure and the particle velocity in FDTD algorithm can be obtained:

$$\begin{aligned} u^{n+1} = {} & a_0 p^{n+1/2} + a_1 p^{n-1/2} + \cdots + a_N p^{n-(N-1/2)} \\ & - b_0 u^n - b_1 u^{n-1} - \cdots - b_M u^{n-M}. \end{aligned} \tag{1.9}$$

By using the treatment in Eq.(1.9), there are some drawbacks such as high computational cost and uncertain instability. Then, Escolano[24] proposed a method based on the "mixing modeling strategies". This method treat the FDTD grids and the boundary condition (the impedance) separately and then joined together using an interface based on the WDF. The impedance is represented by a wave digital filter. In this method, the stability can be ensured and the computational costs can be reduced.

These above methods are based on the locally-reactive assumption of the porous materials. Sound propagation inside the porous material is neglected and not treated. Then errors would be occurred for the local reactive assumption. In addition, the effects caused by the thickness and the shape of the porous material cannot be treated by using locally-reactive assumption.

In order accurately treating porous materials, the wave equations describing sound propagation inside the porous material should be treated.

One simple model describing sound propagation inside the porous material is the Rayleigh model[25]. Suzuki[26-27] proposed FDTD formulas in porous materials based on the Rayleigh model:

$$\frac{\partial p}{\partial t}+\kappa\frac{\partial u}{\partial x}+\sigma_p p=0, \tag{1.10}$$

$$\frac{\partial u}{\partial t}+\frac{1}{\rho_0}\frac{\partial p}{\partial x}+\sigma_x u=0, \tag{1.11}$$

where σ_p is the heat reduction coefficient, and σ_x is the flow resistivity of the porous material. ρ_0 is the density of the air.

This mentioned method is used in some studies[28-30]. However, Rayleigh model is too simple, which cannot accurately simulate a common porous material.

Compared with the Rayleigh model, the Biot theory[31-32] is a more complex model. Assuming the isotropic and homogeneous fluid saturated porous material, the equations are given as:

$$-p=C\nabla\cdot u+M\nabla\cdot w, \tag{1.12}$$

$$-j\omega w=\left(-\nabla p+\omega^2\rho_f u\right)\kappa/\eta, \tag{1.13}$$

$$\nabla\cdot\tau=-\omega^2\left(\rho u+\rho_f w\right), \tag{1.14}$$

$$\tau=\left(H-2G\right)\left(\nabla\cdot u\right)I+C\left(\nabla\cdot w\right)I+G\left(\nabla u+\nabla u^T\right), \tag{1.15}$$

where p is the pressure, u is the displacement of the solid phase, and w is the relative flow between the fluid phase and the solid phase. H, C and M are parameters defined by Biot. ρ_f is the density of the pore fluid; κ is the dynamic permeability; η is the viscosity of the pore fluid; τ is the bulk stress tensor; ρ is the density of the material; I is the identity tensor.

Based on the Biot model, Hosokawa[33] analyzed the ultrasonic pulse wave propagating in bovine cancellous bone by using 2-dimensional FDTD algorithm.

The Biot theory is an effective model describing the behavior of the common porous materials, but it is very complicated to be implemented in the FDTD algorithm. In most cases, the Biot theory can be appropriately simplified.

When the frame of the material is rigid and motionless, the Biot theory could be simplified. Then the rigid-frame porous material is replaced by an equivalent fluid medium. Such a model is called the "equivalent fluid model"[34]. At 1-dimensional sound field, the equations are given as:

$$j\omega p + K_{eq}(\omega)\cdot\frac{\partial u}{\partial x} = 0, \tag{1.16}$$

$$\frac{\partial p}{\partial x} + \rho_{eq}(\omega)\cdot j\omega u = 0, \tag{1.17}$$

where $K_{eq}(\omega)$ is the effective bulk modulus, and $\rho_{eq}(\omega)$ is the effective density.

Base on the equivalent fluid model, some works treating wave propagation in rigid-frame porous materials in time domain have been published[35-46]. Fellah solves the direct and inverse scattering problems at the high and low frequency ranges for the wave propagation in time domain in rigid-frame porous materials[35-41]. Wilson treats the relaxational model for sound propagation in rigid-frame porous materials, in which a time-domain version of the relaxational model was developed[42-44]. Umnova[45] develops time-domain expressions of the complete equivalent fluid model without any restrictions on the frequency bands. Dragna[46] developed the auxiliary differential equation (ADE) method. The convolutions between the relaxation functions and acoustic variables can be computed.

For these mentioned treatments for the wave equations in rigid-frame porous materials, they are difficult to be directly implemented in the FDTD algorithm. Therefore, in this dissertation, based on the equivalent fluid model, a finite-difference time-domain algorithm (EF-FDTD algorithm) is proposed.

1.2 Objectives

In this dissertation, based on the equivalent fluid model, a finite-difference time-domain algorithm (EF-FDTD algorithm) is proposed.

The proposed EF-FDTD algorithm in this dissertation starts from the frequency-domain wave equations in an equivalent fluid medium. In the wave equations, the effective density and effective bulk modulus are frequency-dependent complex values reflecting the effect of visco-thermal dissipation in the rigid-frame porous material.

In order to obtain time domain formulas for the FDTD analysis, a series of efforts need to be paid. In the frequency-domain equations, there exists add operation, multiplication operation, and frequency-dependent complex parameters (the effective density and effective bulk modulus). In order to avoid the complex convolution operations in time domain, the frequency-domain wave equations are firstly transformed to Z-domain. Therefore, for the whole wave equations (containing add operation, multiplication operation and frequency-dependent complex parameters), how to transform them to the Z-domain is the first difficulty point. Then how to treat the wave equations in the Z-domain is another difficulty point. Finally, how to obtain the time domain formulas from the wave equations in the Z domain is the last difficult point.

As the solution, for the frequency-dependent complex parameters (the effective density and the effective bulk modulus), they are designed in the form of infinite impulse response (IIR) filters in frequency domain. The Z-transform theory is used to discretize the frequency-domain wave equations. Some measures are taken to treat the wave equations in Z-domain. By applying the relationship between the Z-domain and the time domain, the formulations in time domain for FDTD analysis can be obtained.

By applying the proposed EF-FDTD algorithm, the wideband frequency characteristic of the porous material can be quickly and accurately simulated. The accuracy of the EF-FDTD algorithm is validated not only at the normal incidence of

sound, but also at the oblique incidence of sound. The proposed EF-FDTD algorithm can simulate the sound field containing the shaped porous material, and the accuracy is also validated. As an important application, porous material is often used to construct the acoustic wedges in anechoic chambers. The method for predicting the absorption coefficients of acoustical wedges by using the proposed EF-FDTD algorithm is proposed. The accuracy is validated by the experiment.

1.3 Chapter Organization

The chapters in this dissertation are arranged as follows:

For chapter1, the background, objectives are introduced.

For chapter 2, the precedence research is introduced. The FDTD analysis method in the air is introduced in section 2.1. The FDTD analysis in the porous material using Rayleigh model is introduced in section 2.2. The necessary Z-transform theory used for chapter 3 is introduced in section 2.3.

For chapter 3, the EF-FDTD algorithm in rigid-flame porous material is introduced. The equivalent fluid model describing sound propagating in rigid-frame porous material is introduced in section 3.2.1. How to change the effective bulk modulus and the effective density to the Z domain by using the IIR filter design method and Z transform theory is introduced in section 3.2.2. The 1-dimensional EF-FDTD algorithm is introduced in section 3.2.3. The 2-dimensional EF-FDTD algorithm and the 3-dimensional EF-FDTD algorithm are introduced in section 3.2.4. The stability condition analysis is introduced in section 3.3.

For chapter 4, the validation of the EF-FDTD algorithm is introduced. The 1-dimensional EF-FDTDT algorithm is validated under the normal incidence of the sound by comparing the numerical analysis and the experiment in section 4.2. The 2-dimensional EF-FDTDT algorithm is validated under the oblique incidence of the sound by comparing the numerical analysis and the theoretical values in section 4.3.

The treatment for simulating the shaped porous material is discussed in section 4.4. The EF-FDTD algorithm is contrasted with the exiting Rayleigh method in section 4.5.

For chapter 5, the simulation of the shaped porous material is introduced. The designed 4 kinds of samples are introduced in section 5.2.1.The measurement system is introduced in section 5.2.2, and the properties of the used porous material are introduced in section 5.2.3. The measured and simulated results for sample A are given in section 5.3. In section 5.3.1, the equations for calculating the absorption coefficients from the measurement data are given. In section 5.3.2.2, the equations for calculating the absorption coefficient from the simulation data are given. In section 5.3.2.3, the factors which affect the result of the absorption coefficient are discussed in detail. The measured and simulated results for sample B, sample C and sample D are given in section 5.4, section 5.5 and section 5.6, respectively. The conclusions are introduced in section 5.7.

For chapter 6, the summaries of this dissertation are given, and the follow-up research work is introduced.

Chapter 2 PRECEDENCE RESEARCH

2.1 FDTD analysis in the air

The FDTD analysis in the air is firstly given in details[47]. The wave equations in the air are given as:

$$\rho\frac{\partial u}{\partial t}+\frac{\partial p}{\partial x}=0, \tag{2.1}$$

$$\rho\frac{\partial v}{\partial t}+\frac{\partial p}{\partial y}=0, \tag{2.2}$$

$$\rho\frac{\partial w}{\partial t}+\frac{\partial p}{\partial z}=0, \tag{2.3}$$

$$\frac{\partial p}{\partial t}+\kappa\left(\frac{\partial u}{\partial x}+\frac{\partial v}{\partial y}+\frac{\partial w}{\partial z}\right)=0, \tag{2.4}$$

where p is the sound pressure; u, v and w are the particle velocity in the x, y and z direction, respectively; κ is the volume elastic ratio in the air, which is equal to ρc^2. Here, ρ is the density of the air ; c is the sound speed in the air.

The FDTD formulations are given as:

$$u^{n+1}\left(i+1/2,j,k\right)=u^{n}\left(i+1/2,j,k\right)-\frac{\Delta t}{\rho h}\left[p^{n+1/2}\left(i+1,j,k\right)-p^{n+1/2}\left(i,j,k\right)\right], \tag{2.5}$$

$$v^{n+1}\left(i,j+1/2,k\right)=v^{n}\left(i,j+1/2,k\right)-\frac{\Delta t}{\rho h}\left[p^{n+1/2}\left(i,j+1,k\right)-p^{n+1/2}\left(i,j,k\right)\right], \tag{2.6}$$

$$w^{n+1}\left(i,j,k+1/2\right)=w^{n}\left(i,j,k+1/2\right)-\frac{\Delta t}{\rho h}\left[p^{n+1/2}\left(i,j,k+1\right)-p^{n+1/2}\left(i,j,k\right)\right], \tag{2.7}$$

$$\begin{aligned}p^{n+1/2}\left(i,j,k\right)=p^{n-1/2}\left(i,j,k\right)&-\frac{\kappa\Delta t}{h}\left[u^{n}\left(i+1/2,j,k\right)-u^{n}\left(i-1/2,j,k\right)\right]\\&-\frac{\kappa\Delta t}{h}\left[v^{n}\left(i,j+1/2,k\right)-v^{n}\left(i,j-1/2,k\right)\right]\\&-\frac{\kappa\Delta t}{h}\left[w^{n}\left(i,j,k+1/2\right)-w^{n}\left(i,j,k-1/2\right)\right].\end{aligned} \tag{2.8}$$

2.2 FDTD analysis in the porous material based on the Rayleigh model

As the existing method, Suzuki[26-27] proposed the FDTD formulas in porous material based on Rayleigh model. In Rayleigh model, the porous material is simplified by a group of thin pipes with perfectly rigid bodies, as illustrated in Fig.2.1.

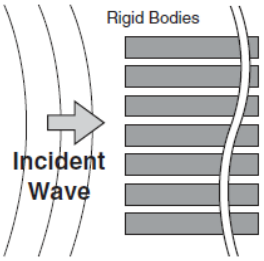

Fig.2.1 The image of the Rayleigh model.

In 1-dimensional sound field, the equations in Rayleigh model are given by:

$$\frac{\partial p}{\partial t}+\kappa\frac{\partial u}{\partial x}+\sigma_p p=0, \tag{2.9}$$

$$\frac{\partial u}{\partial t}+\frac{1}{\rho_0}\frac{\partial p}{\partial x}+\sigma_x u=0, \tag{2.10}$$

where σ_p is the heat reduction coefficient, and σ_x is the flow resistivity of the porous material. ρ_0 is the density of the air.

The FDTD formulations are expressed as:

$$\begin{aligned} p^{n+1/2}(i,j,k)=&\left(1-\frac{\Delta t\sigma_p}{\rho}\right)p^{n-1/2}(i,j,k)\\ &-\frac{\Delta t\kappa}{\Delta x}\left[u^n(i+1/2,j,k)-u^n(i-1/2,j,k)\right], \end{aligned} \tag{2.11}$$

$$\begin{aligned} u^{n+1}(i+1/2,j,k)=&\left(1-\frac{\Delta t\sigma_x}{\rho}\right)u^n(i+1/2,j,k)\\ &-\frac{\Delta t}{\rho\Delta x}\left[p^{n+1/2}(i+1,j,k)-p^{n+1/2}(i,j,k)\right]. \end{aligned} \tag{2.12}$$

2.3 Z-transform theory

In this thesis, Z-transform is used to fit into the FDTD analysis, which has a little difference from what is used in the signal processing and system theory literature. For the most part, they are similar. The specific theorems can be found in the reference[48-50]. Here, only the theorems used in this thesis are listed.

(1) One of the most important properties of the Z-transform theory used in this thesis is the convolution theorem, which is given as

$$y(t)=\int_0^{\infty} h(\tau)\cdot x(t-\tau)\,d\tau \Leftrightarrow Y(\omega)=H(\omega)\cdot X(\omega) \Leftrightarrow Y(z)=\Delta t\cdot H(z)\cdot X(z). \tag{2.13}$$

In Eq.(2.19), Δt is the discrete time interval for the FDTD analysis. It can be found that the theorem used here is different from that used in the signal processing and system theory literature, which is

$$Y(z)=H(z)\cdot X(z). \tag{2.14}$$

The detailed analysis for this difference can be found in the reference[5], which is not given here. This property is the main motivation for using the Z-transform theory into FDTD analysis.

(2) The other important properties of the Z-transform are:

$$j\omega \Leftrightarrow \frac{1-z^{-1}}{\Delta t}, \tag{2.15}$$

$$\frac{1}{j\omega+\alpha} \Leftrightarrow \frac{1}{1-z^{-1}e^{-\alpha\Delta t}}, \tag{2.16}$$

$$\frac{\beta}{\left(\alpha^2+\beta^2\right)+j2\alpha\omega-\omega^2} \Leftrightarrow \frac{e^{-\alpha\Delta t}\cdot\sin\left(\beta\Delta t\right)\cdot z^{-1}}{1-2e^{-\alpha\Delta t}\cos\left(\beta\Delta t\right)\cdot z^{-1}+e^{-2\alpha\Delta t}\cdot z^{-2}}, \tag{2.17}$$

$$\frac{\alpha+j\omega}{\left(\alpha^2+\beta^2\right)+j2\alpha\omega-\omega^2} \Leftrightarrow \frac{1-e^{-\alpha\Delta t}\cdot\cos\left(\beta\Delta t\right)\cdot z^{-1}}{1-2e^{-\alpha\Delta t}\cos\left(\beta\Delta t\right)\cdot z^{-1}+e^{-2\alpha\Delta t}\cdot z^{-2}}, \tag{2.18}$$

constant in frequency domain $\Leftrightarrow$ constant in Z domain.

Chapter 3 EF-FDTD ALGORITHM IN POROUS MATERIAL

3.1 Introduction

In this section, the EF-FDTD algorithm in the rigid-flame porous material and the analysis for the stability conditions are introduced. In section 3.2.1, the equivalent fluid model describing the sound wave propagating in porous material with rigid frame is introduced. In section 3.2.2, how to change the effective bulk modulus and the effective density to Z domain by using the IIR filter design method and Z transform theory is introduced. In section 3.2.3, the 1-dimensional EF-FDTD algorithm is introduced. In section 3.2.4, the 2-dimensional EF-FDTD algorithm and the 3-dimensional EF-FDTD algorithm are introduced. In section 3.3, the stability condition analysis is introduced.

3.2 The EF-FDTD algorithm in the rigid-frame porous materials

3.2.1 The equivalent fluid model

When a sound wave propagates in the rigid-frame porous material, the sound wave is attenuated by the viscous effects and thermal effects in the porous material. These two mechanisms of attenuation are assumed to be decoupled and can be treated independently. When the frame is not moved, the rigid-frame porous material could be replaced by an equivalent fluid medium. The frequency-domain wave equations in 3-dimensional sound field are expressed as[51]:

$$j\omega p + K_{eq}(\omega)\cdot\left(\frac{\partial u}{\partial x}+\frac{\partial v}{\partial y}+\frac{\partial w}{\partial z}\right)=0, \tag{3.1}$$

$$\frac{\partial p}{\partial x}+\rho_{eq}(\omega)\cdot j\omega u=0, \tag{3.2}$$

$$\frac{\partial p}{\partial y}+\rho_{eq}(\omega)\cdot j\omega v=0, \tag{3.3}$$

$$\frac{\partial p}{\partial z}+\rho_{eq}(\omega)\cdot j\omega w=0. \tag{3.4}$$

In the equations, p is the sound pressure; u, v and ω are the particle velocities in x, y and z direction, respectively; $j\omega$ can be seen as the differential operator with respect to the time, and ω is the angular frequency; $K_{eq}(\omega)$ is the effective bulk modulus, corresponding to the thermal effects in porous material; $\rho_{eq}(\omega)$ is the effective density, corresponding to the viscous effects in porous material.

$K_{eq}(\omega)$ and $\rho_{eq}(\omega)$ are mostly described by the JCAL model. Johnson[52-53] treated the visco-inertial effect in the porous materials from macroscopic parameters, Champoux and Allard[54] treated the thermal effect, and Lafarage[55] improved the thermal response. The detailed presentation can be found in the book by Allard[34], which is given as follows.

The effective density described by Johnson is given as:

$$\rho_{eq}(\omega)=\rho_0\alpha(\omega), \tag{3.5}$$

$$\alpha(\omega)=\frac{\upsilon\phi}{j\omega q_0}\left[1+\left(\frac{2\alpha_\infty q_0}{\phi\Lambda}\right)^{1/2}\frac{j\omega}{\upsilon}\right]^{1/2}+\alpha_\infty. \tag{3.6}$$

The effective bulk modulus by the simplified Lafrarge model is given as:

$$K_{eq}(\omega)=\frac{P_0}{1-\dfrac{\gamma-1}{\gamma\alpha'(\omega)}}, \tag{3.7}$$

$$\alpha'(\omega)=\frac{\nu'\phi}{j\omega q_0'}\left[1+\left(\frac{2q_0'}{\phi\Lambda'}\right)^{2}\frac{j\omega}{\nu'}\right]^{1/2}+1. \tag{3.8}$$

In these above equations, $\nu=\eta/\rho_0=B^2\nu'$, B^2 is the Prandtl number; q_0 is the viscous static permeability; q_0' is the permeability; ϕ is the porosity; α_∞ is the tortuosity; Λ and Λ' are the viscous characteristic length and the thermal characteristic length, respectively.

It can be found that the wave equations of Eqs.(3.1)-(3.4) are in frequency domain. The effective density $\rho_{eq}(\omega)$ represented by Eqs. (3.5)-(3.6) and the effective bulk modulus $K_{eq}(\omega)$ represented by Eqs. (3.7)-(3.8) are frequency dependent. It is complicated if these equations are directly transformed to the time domain.

In Eqs.(3.1)-(3.4), there exists the add operation, multiplication operation and frequency dependent parameters. The multiplication operation in frequency domain becomes a complicated convolution operation in time domain, but remains the multiplication operation in Z domain. From this point, the following idea is considered: why not transform the whole wave equations firstly to Z domain, and then transformed to time domain?

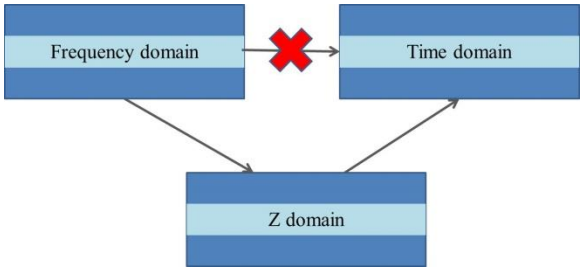

Fig. 3.1 The producre for deducing the EF-FDTD algorithm.

In the process of deducing the EF-FDTD algorithm, the difficulty points are:

(1) How to transform the whole wave equations (containing add operation, multiplication operation, and frequency dependent parameters) to the Z domain;

(2) How to treat the wave equations in the Z domain;

(3) How to obtain the time domain formulas from the wave equations in the Z domain;

In the following sections, how to solve these difficulty points are introduced in detail.

3.2.2 Change the effective bulk modulus and the effective density to Z domain

3.2.2.1 IIR filter design

When transform the whole wave equations to the Z domain, one difficult point is how to change the frequency dependent parameters (the effective bulk modulus $K_{eq}(\omega)$ and the effective density $\rho_{eq}(\omega)$) to Z domain. For example, when the effective density is expressed by Eqs.(3.5)-(3.6), the Z transform of $(1+coefficient\cdot j\omega)^{\frac{1}{2}}$ is difficult to be handled. In some cases, the parameters for the JCAL model are very difficult to be obtained. As an alternative method, the effective bulk modulus $K_{eq}(\omega)$ and the effective density $\rho_{eq}(\omega)$ are measured in an Impedance tube. In this case, only some discrete data at specific frequency points are obtained. These discrete data do not have mathematic expressions. Therefore, when

transforming the effective bulk modulus $K_{eq}(\omega)$ and the effective density $\rho_{eq}(\omega)$ to Z domain, an easy to be processed expressions need to be constructed.

Based on the Z-transform theories in section 2.3, the following transformations are known:

$$\frac{1}{j\omega+\alpha} \Leftrightarrow \frac{1}{1-z^{-1}e^{-\alpha\Delta t}}, \tag{3.9}$$

$$\frac{\beta}{\left(\alpha^2+\beta^2\right)+j2\alpha\omega-\omega^2} \Leftrightarrow \frac{e^{-\alpha\Delta t}\cdot\sin\left(\beta\Delta t\right)\cdot z^{-1}}{1-2e^{-\alpha\Delta t}\cos\left(\beta\Delta t\right)\cdot z^{-1}+e^{-2\alpha\Delta t}\cdot z^{-2}}, \tag{3.10}$$

$$\frac{\alpha+j\omega}{\left(\alpha^2+\beta^2\right)+j2\alpha\omega-\omega^2} \Leftrightarrow \frac{1-e^{-\alpha\Delta t}\cdot\cos\left(\beta\Delta t\right)\cdot z^{-1}}{1-2e^{-\alpha\Delta t}\cos\left(\beta\Delta t\right)\cdot z^{-1}+e^{-2\alpha\Delta t}\cdot z^{-2}}, \tag{3.11}$$

constant in frequency domain $\Leftrightarrow$ constant in Z domain.

In Eq.(3.9)-Eq.(3.11), $1/j\omega+\alpha$ is one pole filter in the frequency domain, $\beta/\left(\alpha^2+\beta^2\right)+j2\alpha\omega-\omega^2$ and $\alpha+j\omega/\left(\alpha^2+\beta^2\right)+j2\alpha\omega-\omega^2$ are two kinds of two poles filter. The constant in frequency domain is not changed in Z domain.

Therefore, it is a wise choice to reconstruct the effective bulk modulus $K_{eq}(\omega)$ and the effective density $\rho_{eq}(\omega)$ by using the above 4 frequency domain expressions in Eq.(3.9)-Eq.(3.11). The transfer function of the IIR filter could be solved to contain the above 4 frequency domain expressions.

The transfer function of the IIR filter is represented as[56-57]:

$$H(j\omega)=\frac{B(j\omega)}{A(j\omega)}=\frac{b_1(j\omega)^n+b_2(j\omega)^{n-1}+\cdots b_{n+1}}{a_1(j\omega)^m+a_2(j\omega)^{m-1}+\cdots a_{m+1}}. \tag{3.12}$$

By using the pole-residue form, Eq.(3.12) can be rewritten as:

$$H(\omega)=k_0+\sum_{l=1}^{N}\frac{r_l}{j\omega-q_l}, \tag{3.13}$$

where k_0 is a real number, equal to b_1/a_1; $q_1, q_2, \cdots$ and q_N are the poles of the IIR filter; $r_1, r_2, \cdots$ and r_N are the residues of the IIR filter. N is the total number of the poles. In Eq.(3.13), The values of the poles and residues can be real or complex numbers, so they are also written as:

$$H_1(\omega)=\sum_{l=1}^{N_1}\frac{r_l}{j\omega-q_l}, \tag{3.14}$$

$$H_2(\omega)=\sum_{k=1}^{N_2}\frac{r_k}{j\omega-q_k}+\frac{r_k^*}{j\omega-q_k^*}. \tag{3.15}$$

In Eq.(3.14), q_l and r_l are real numbers, and N_1 is the number of the real poles. In Eq.(3.15), q_k, q_k^*, r_k and r_k^* are complex numbers, and N_2 is the number of the pair of the complex poles. The relationship between N, N_1 and N_2 is :

$$N=N_1+2N_2. \tag{3.16}$$

In Eq.(3.15), q_k, q_k^*, r_k and r_k^* are given as:

$$q_k=-\alpha_k+j\beta_k, \tag{3.17}$$

$$q_k^*=-\alpha_k-j\beta_k, \tag{3.18}$$

$$r_k=\lambda_k+j\mu_k, \tag{3.19}$$

$$r_k^*=\lambda_k-j\mu_k. \tag{3.20}$$

Input Eqs.(3.17)-(3.20) to Eq.(3.15), the following equation is obtained:

$$H_2(\omega)=\sum_{k=1}^{N_2}\frac{2\lambda_k(\alpha_k+j\omega)-2\mu_k\beta_k}{{\alpha_k}^2+{\beta_k}^2+j2\alpha_k\omega-\omega^2}. \tag{3.21}$$

3.2.2.2 Z transform of the IIR filter

Firstly, Z transform theory is applied to the IIR filters. According to the properties of the Z transform theory in chapter 2.3, the Z transform of $H_1(\omega)$ is:

$$H_1(z)=\sum_{l=1}^{N_1}r_l+\frac{a_l\cdot z^{-1}}{1-b_l\cdot z^{-1}}, \tag{3.22}$$

$$a_l=r_l\cdot e^{q_l\Delta t}, \tag{3.23}$$

$$b_l=e^{q_l\Delta t}. \tag{3.24}$$

The Z transform of $H_2(\omega)$ is:

$$H_2(z)=\sum_{k=1}^{N_2}2\lambda_k+\frac{X1_k\cdot z^{-1}-X2_k\cdot z^{-2}}{1-X3_k\cdot z^{-1}+X4_k\cdot z^{-2}}, \tag{3.25}$$

$$X1_k=2\lambda_k\cdot e^{-\alpha_k\Delta t}\cdot\cos(\beta_k\Delta t)-2\mu_k\cdot e^{-\alpha_k\Delta t}\cdot\sin(\beta_k\Delta t), \tag{3.26}$$

$$X2_k=2\lambda_k\cdot e^{-2\alpha_k\Delta t}, \tag{3.27}$$

$$X3_k=2e^{-\alpha_k\Delta t}\cdot\cos(\beta_k\Delta t), \tag{3.28}$$

$$X4_k=e^{-2\alpha_k\Delta t}. \tag{3.29}$$

In these above equations, Δt is the discrete time interval in the FDTD analysis; The IIR filter for $K_{eq}(\omega)$ and $\rho_{eq}(\omega)$ are given by:

$$K_{eq}(\omega)=k_0+H_1(\omega)+H_2(\omega), \tag{3.30}$$

$$\rho_{eq}(\omega)=k_0'+H_1'(\omega)+H_2'(\omega). \tag{3.31}$$

The Z transforms of $H_1'(\omega)$ has the same expressions as $H_1(z)$. The Z transforms of $H_2'(\omega)$ has the same expressions as $H_2(z)$.

3.2.3 1-dimensional EF-FDTD algorithm

3.2.3.1 Z transform of the 1-dimensional wave equations

In 1-dimensioanl sound field, the wave equations are:

$$j\omega p+K_{eq}(\omega)\cdot\frac{\partial u}{\partial x}=0, \tag{3.32}$$

$$\frac{\partial p}{\partial x}+\rho_{eq}(\omega)\cdot j\omega u=0. \tag{3.33}$$

Then, Z transform theory is applied to wave equations. Eq.(3.32) and Eq.(3.33) are transformed to the Z domain:

$$\frac{1-z^{-1}}{\Delta t}P_z(i)+\left[k_0+H_1(z)\Delta t+H_2(z)\Delta t\right]\cdot\frac{1}{\Delta x}\cdot\left[U_z\left(i+\frac{1}{2}\right)-U_z\left(i-\frac{1}{2}\right)\right]=0, \tag{3.34}$$

$$\frac{1-z^{-1}}{\Delta t}\cdot\left[k_0{}'+H_1{}'(z)\Delta t+H_2{}'(z)\Delta t\right]\cdot U_z\left(i+\frac{1}{2}\right)+\frac{1}{\Delta x}\cdot\left[P_z(i+1)-P_z(i)\right]=0,$$

(3.35)

where P_z and U_z are the expressions in Z domain for the sound pressure p and the particle velocity u, respectively; In FDTD analysis, Δx is the discrete spatial interval, and Δt is the discrete time interval.

Inserting Eq.(3.22) and Eq.(3.25) into Eqs.(3.34)-(3.35) yields:

$$\frac{1-z^{-1}}{\Delta t}P_z(i)+\left[k_0+\sum_{l=1}^{N_1}\left(r_l\Delta t+\frac{a_l\Delta t\cdot z^{-1}}{1-b_l\cdot z^{-1}}\right)+\sum_{k=1}^{N_2}\left(2\lambda_k\Delta t+\frac{X1_k\Delta t\cdot z^{-1}-X2_k\Delta t\cdot z^{-2}}{1-X3_k\cdot z^{-1}+X4_k\cdot z^{-2}}\right)\right]\cdot \frac{1}{\Delta x}\cdot\left[U_z\left(i+\frac{1}{2}\right)-U_z\left(i-\frac{1}{2}\right)\right]=0,$$

(3.36)

$$\frac{1-z^{-1}}{\Delta t}\cdot\left[k_0{}'+\sum_{l=1}^{N_1'}\left(r_l{}'\Delta t+\frac{a_l{}'\Delta t\cdot z^{-1}}{1-b_l{}'\cdot z^{-1}}\right)+\sum_{k=1}^{N_2'}\left(2\lambda_k{}'\Delta t+\frac{X1_k{}'\Delta t\cdot z^{-1}-X2_k{}'\Delta t\cdot z^{-2}}{1-X3_k{}'\cdot z^{-1}+X4_k{}'\cdot z^{-2}}\right)\right]\cdot U_z\left(i+\frac{1}{2}\right)+\frac{1}{\Delta x}\cdot\left[P_z(i+1)-P_z(i)\right]=0.$$

(3.37)

It can be found that Eqs.(3.36)-(3.37) are very complicated. In order to simplify these equations, the following parameters are defined:

$$D(i)=\frac{U_z\left(i+\frac{1}{2}\right)-U_z\left(i-\frac{1}{2}\right)}{\Delta x},\tag{3.38}$$

$$I_l(i)=\frac{D(i)}{1-b_l\cdot z^{-1}},\quad l=1,2\cdots N_1,\tag{3.39}$$

$$Q_k(i)=\frac{D(i)}{1-X3_k\cdot z^{-1}+X4_k\cdot z^{-2}},\quad k=1,2\cdots N_2,\tag{3.40}$$

$$M_l\left(i+\frac{1}{2}\right)=\frac{1}{1-b_l{}'\cdot z^{-1}}\cdot U_z\left(i+\frac{1}{2}\right),\quad l=1,2\cdots N_1{}',\tag{3.41}$$

$$R_k\left(i+\frac{1}{2}\right)=\frac{1}{1-X3_k'\cdot z^{-1}+X4_k'\cdot z^{-2}}\cdot U_z\left(i+\frac{1}{2}\right),\quad k=1,2\cdots N_2'. \tag{3.42}$$

Substituting Eqs.(3.38)-(3.42) into Eqs. (3.36)-(3.37) yields:

$$P_z(i)=z^{-1}P_z(i)-K_e\Delta t\cdot D(i)-\Delta t^2\sum_{l=1}^{N_1}a_l\cdot z^{-1}I_l(i) \tag{3.43}$$
$$-\Delta t^2\sum_{k=1}^{N_2}X1_k\cdot z^{-1}Q_k(i)-X2_k\cdot z^{-2}Q_k(i),$$

$$U_z\left(i+\frac{1}{2}\right)=z^{-1}U_z\left(i+\frac{1}{2}\right)-\frac{\Delta t}{\rho_e\Delta x}\left[P_z(i+1)-P_z(i)\right] \tag{3.44}$$
$$-\frac{\Delta t}{\rho_e}\sum_{l=1}^{N_1'}a_l'\left[z^{-1}M_l\left(i+\frac{1}{2}\right)-z^{-2}M_l\left(i+\frac{1}{2}\right)\right]$$
$$-\frac{\Delta t}{\rho_e}\sum_{k=1}^{N_2'}X1_k'\left[z^{-1}R_k\left(i+\frac{1}{2}\right)-z^{-2}R_k\left(i+\frac{1}{2}\right)\right]$$
$$+\frac{\Delta t}{\rho_e}\sum_{k=1}^{N_2'}X2_k'\left[z^{-2}R_k\left(i+\frac{1}{2}\right)-z^{-3}R_k\left(i+\frac{1}{2}\right)\right],$$

where

$$K_e=k_0+\sum_{l=1}^{N_1}r_l\Delta t+\sum_{k=1}^{N_2}2\lambda_k\Delta t, \tag{3.45}$$

$$\rho_e=k_0'+\sum_{l=1}^{N_1'}r_l'\Delta t+\sum_{k=1}^{N_2'}2\lambda_k'\Delta t. \tag{3.46}$$

3.2.3.2 1-dimensional EF-FDTD formulae in time domain

Finally, the equations in Z domain are transformed to time domain. z^{-1} in Z domain represents one time delay in time domain. The distributions of the discrete points of sound pressure p, the particle velocity u and the defined parameters $I\left(I_1\cdots I_{N_1}\right)$, $Q\left(Q_1\cdots Q_{N_2}\right)$, $M\left(M_1\cdots M_{N_1'}\right)$ and $R\left(R_1\cdots R_{N_2'}\right)$ are shown in Fig.3.2.

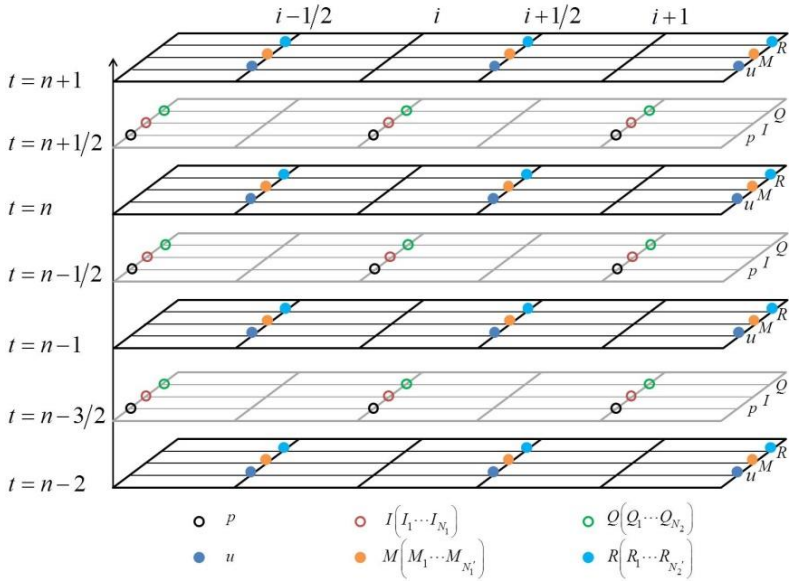

Fig.3.2 The discretized points for the sound pressure, the particle velocities and defined parameters.

Finally, the EF-FDTD formulas are:

$$D(i)=\frac{1}{\Delta x}\left[u^{n}(i+1/2)-u^{n}(i-1/2)\right], \tag{3.47}$$

$$\begin{aligned} p^{n+\frac{1}{2}}(i) &= p^{n-\frac{1}{2}}(i)-K_e\Delta t\cdot D(i) \\ &\quad -\Delta t^2\sum_{l=1}^{N_1}a_l\cdot {I_l}^{n-\frac{1}{2}}(i) \\ &\quad -\Delta t^2\sum_{k=1}^{N_2}X1_k\cdot {Q_k}^{n-\frac{1}{2}}(i)-X2_k\cdot {Q_k}^{n-\frac{3}{2}}(i), \end{aligned} \tag{3.48}$$

$${I_l}^{n+\frac{1}{2}}(i)=b_l\cdot {I_l}^{n-\frac{1}{2}}(i)+D(i),\quad l=1,2\cdots N_1, \tag{3.49}$$

$$\begin{aligned} {Q_k}^{n+\frac{1}{2}}(i) &= X3_k\cdot {Q_k}^{n-\frac{1}{2}}(i)-X4_k\cdot {Q_k}^{n-\frac{3}{2}}(i)+D(i), \\ & k=1,2\cdots N_2, \end{aligned} \tag{3.50}$$

$$\begin{aligned} u^{n+1}\left(i+\frac{1}{2}\right) &= u^{n}\left(i+\frac{1}{2}\right)-\frac{\Delta t}{\rho_e\Delta x}\left[{p}^{n+\frac{1}{2}}(i+1)-{p}^{n+\frac{1}{2}}(i)\right] \\ &\quad -\frac{\Delta t}{\rho_e}\sum_{l=1}^{N_1'}a_l'\cdot\left[{M_l}^{n}\left(i+\frac{1}{2}\right)-{M_l}^{n-1}\left(i+\frac{1}{2}\right)\right] \\ &\quad -\frac{\Delta t}{\rho_e}\sum_{k=1}^{N_2'}X1_k'\cdot\left[{R_k}^{n}\left(i+\frac{1}{2}\right)-{R_k}^{n-1}\left(i+\frac{1}{2}\right)\right] \\ &\quad +\frac{\Delta t}{\rho_e}\sum_{k=1}^{N_2'}X2_k'\cdot\left[{R_k}^{n-1}\left(i+\frac{1}{2}\right)-{R_k}^{n-2}\left(i+\frac{1}{2}\right)\right], \end{aligned} \tag{3.51}$$

$$M_l^{n+1}\left(i+\frac{1}{2}\right)=u^{n+1}\left(i+\frac{1}{2}\right)+b_l'\cdot M_l^{n}\left(i+\frac{1}{2}\right), \tag{3.52}$$

$$l=1,2\cdots N_1',$$

$$R_k^{n+1}\left(i+\frac{1}{2}\right)=u^{n+1}\left(i+\frac{1}{2}\right)+X3_k'\cdot R_k^{n}\left(i+\frac{1}{2}\right)-X4_k'\cdot R_k^{n-1}\left(i+\frac{1}{2}\right), \tag{3.53}$$

$$k=1,2\cdots N_2'.$$

It should be noted that the forms of the EF-FDTD algorithm equations in this thesis is different from that published paper written by the author[59]. Essentially, both of them are correct. In this dissertation, the new parameter D is defined. The reason for using this new parameter is that the equations of the 2-dimensional EF-FDTD algorithm and 2-dimensional EF-FDTD algorithm can be easily obtained by only changing the parameter D. And the high accuracy algorithm can also be easily introduced (given in Appendix C), especially if the discrete space interval $\Delta x \neq \Delta y \neq \Delta z$, no need to change the other parameters in the algorithm.

The thermal effects and the viscous effects in the rigid-frame porous materials are reflected in EF-FDTD equations. The thermal effects are reflected in Eqs.(3.48) -(3.50), because the coefficients of K_e, a_l, b_l, $X1_k$, $X2_k$, $X3_k$ and $X4_k$ are related to the IIR filter of the effective bulk modulus $K_{eq}(\omega)$. The viscous effects in the porous material are reflected in Eqs.(3.51)-(3.53), because the coefficients of ρ_e, a_l', b_l', $X1_k'$, $X2_k'$, $X3_k'$ and $X4_k'$ are related to the IIR filter of the effective density $\rho_{eq}(\omega)$.

Once the IIR filters for the effective bulk modulus $K_{eq}(\omega)$ and the effective density $\rho_{eq}(\omega)$ is determined, there is no need to design them again if Δt changed.

In Eqs.(3.47)-(3.53), the IIR filters designed for the effective bulk modulus $K_{eq}(\omega)$ and the effective density $\rho_{eq}(\omega)$ have both real poles and complex poles. N_1 is the number of the real poles of the designed IIR filter for the effective bulk modulus, and correspondingly there exits I_1, $I_2,\cdots I_{N_1}$; N_2 is the number of the pair of complex poles of the designed IIR filter for the effective bulk modulus, and correspondingly there exits Q_1, $Q_2,\cdots Q_{N_2}$; N_1' is the number of the real poles of

the designed IIR filter for the effective density, and correspondingly there exits M_1, $M_2, \cdots M_{N_1'}$; N_2' is the number of the pair of complex poles of the designed IIR filter for the effective density, and there exits R_1, $R_2, \cdots R_{N_2'}$.

In some cases, the IIR filters can be designed to only have real poles. Then the algorithm can be significantly simplified.

When the IIR filter for $K_{eq}(\omega)$ is designed to only have real poles, the coefficients $X1_k$, $X2_k$, $X3_k$ and $X4_k$ are all 0, and Eq.(3.48) becomes:

$$p^{n+\frac{1}{2}}(i) = p^{n-\frac{1}{2}}(i) - K_e \Delta t \cdot D(i) - \Delta t^2 \sum_{l=1}^{N_1} a_l \cdot I_l^{n-\frac{1}{2}}(i). \tag{3.54}$$

When the IIR filter for $\rho_{eq}(\omega)$ is designed to only have real poles, the coefficients $X1_k'$, $X2_k'$, $X3_k'$ and $X4_k'$ are all 0, and Eq.(3.51) becomes:

$$\begin{aligned} u^{n+1}\left(i+\frac{1}{2}\right) = u^n\left(i+\frac{1}{2}\right) - \frac{\Delta t}{\rho_e \Delta x}\left[p^{n+\frac{1}{2}}(i+1) - p^{n+\frac{1}{2}}(i)\right] \\ - \frac{\Delta t}{\rho_e}\sum_{l=1}^{N_1'} a_l' \cdot \left[M_l^{\,n}\left(i+\frac{1}{2}\right) - M_l^{\,n-1}\left(i+\frac{1}{2}\right)\right]. \end{aligned} \tag{3.55}$$

3.2.4 2-dimensional EF-FDTD algorithm and 3-dimensional EF-FDTD algorithm

The derivation for the 2-dimensional EF-FDTD algorithm and 3-dimensional EF-FDTD algorithm is the same as that for the 1-dimensional EF-FDTD algorithm. For the 2-dimensional EF-FDTD algorithm, the only place need to be changed is D. $D(i)$ is replaced by $D(i,j)$:

$$\begin{aligned} D(i,j) = &\frac{1}{\Delta x}\left[u^n(i+1/2,j)-u^n(i-1/2,j)\right] \\ &+\frac{1}{\Delta y}\left[v^n(i,j+1/2)-v^n(i,j-1/2)\right]. \end{aligned} \tag{3.56}$$

For the 3-dimensional EF-FDTD algorithm, $D(i)$ is replaced by $D(i,j,k)$:

$$\begin{aligned} D(i,j,k) = &\frac{1}{\Delta x}\left[u^n(i+1/2,j,k)-u^n(i-1/2,j,k)\right] \\ &+\frac{1}{\Delta y}\left[v^n(i,j+1/2,k)-v^n(i,j-1/2,k)\right] \\ &+\frac{1}{\Delta z}\left[w^n(i,j,k+1/2)-w^n(i,j,k-1/2)\right]. \end{aligned} \tag{3.57}$$

It can be seen by using the parameter D, the algorithm becomes easy to be coded.

The other parameters ($K_e, a_l, b_l, X1_k, X2_k, X3_k, X4_k$) are the same as that used in 1-dimensional EF-FDTD algorithm.

The other formulas for updating p, $I(I_1, I_2 \cdots I_{N1})$ and $Q(Q_1, Q_2 \cdots Q_{N2})$ are the same as Eqs.(3.48)-(3.50).

3.3 Stability condition analysis

3.3.1 Stability condition for 1-dimensional EF-FDTD algorithm

For the proposed EF-FDTD algorithm, the stability condition needs to be discussed. The procedure of deducing the stability condition for the EF-FDTD algorithm is similar as that for the FDTD algorithm in the air[45].

Firstly, the stability condition for the 1-dimensional EF-FDTD algorithm is discussed. The sound pressure p, the particle velocity u, and the defined parameters are expressed as:

$$p^{n+\frac{1}{2}}(i)=p_0 Z^{n+\frac{1}{2}}\cdot e^{-jk(i\Delta x)}, \tag{3.58}$$

$$u^{n}\left(i+\frac{1}{2}\right)=u_0 Z^{n}\cdot e^{-jk\left(i+\frac{1}{2}\right)\Delta x}, \tag{3.59}$$

$$I_l^{n+\frac{1}{2}}(i)=I_{l\_0} Z^{n+\frac{1}{2}}\cdot e^{-jk(i)\Delta x},\ l \text{ is from 1 to } N_1, \tag{3.60}$$

$$Q_k^{n+\frac{1}{2}}(i)=Q_{k\_0} Z^{n+\frac{1}{2}}\cdot e^{-jk(i)\Delta x},\ k \text{ is from 1 to } N_2, \tag{3.61}$$

$$M_l^{n+1}\left(i+\frac{1}{2}\right)=M_{l\_0} Z^{n+1}\cdot e^{-jk\left(i+\frac{1}{2}\right)\Delta x},\ l \text{ is from 1 to } N_1', \tag{3.62}$$

$$R_k^{n+1}\left(i+\frac{1}{2}\right)=R_{k\_0} Z^{n+1}\cdot e^{-jk\left(i+\frac{1}{2}\right)\Delta x},\ k \text{ is from 1 to } N_2', \tag{3.63}$$

where Z represents the complex amplification ratio per time step, p_0, u_0, I_{l_0}, Q_{k_0}, M_{l_0} and R_{k_0} are initial values.

Put the above equations into Eqs.(3.47)-(3.53) leads to:

$$p_0\left(Z^{\frac{1}{2}}-Z^{-\frac{1}{2}}\right)+u_0\frac{K_e\Delta t}{\Delta x}\left[-j2\sin\left(\frac{k\Delta x}{2}\right)\right]+\Delta t^2\sum_{l=1}^{N_1}I_{l0}\cdot Z^{-\frac{1}{2}}a_l \tag{3.64}$$
$$+\Delta t^2\sum_{k=1}^{N_2}Q_{k0}\cdot\left(X1_k Z^{-\frac{1}{2}}-X2_k Z^{-\frac{3}{2}}\right)=0,$$

$$I_{l\_0}=\frac{u_0}{\Delta x}\cdot\frac{-j2\sin\left(\frac{k\Delta x}{2}\right)}{Z^{\frac{1}{2}}-b_l Z^{-\frac{1}{2}}},\ l \text{ is from 1 to } N_1, \tag{3.65}$$

$$Q_{k\_0}=\frac{u_0}{\Delta x}\cdot\frac{-j2\sin\left(\frac{k\Delta x}{2}\right)}{Z^{\frac{1}{2}}-X3_k\cdot Z^{-\frac{1}{2}}+X4_k\cdot Z^{-\frac{3}{2}}},\ k\ \text{is from 1 to}\ N_2, \tag{3.66}$$

$$\frac{\Delta t}{\rho_e\Delta x}p_0Z^{\frac{1}{2}}\left[-j2\sin\left(\frac{k\Delta x}{2}\right)\right]+u_0\left(Z-1\right)+\frac{\Delta t}{\rho_e}\sum_{l=1}^{N_1'}a_l'\cdot M_{l\_0}\left[1-Z^{-1}\right] \tag{3.67}$$
$$+\frac{\Delta t}{\rho_e}\sum_{k=1}^{N_2'}R_{k\_0}\cdot\left[X1_k'\cdot\left(1-Z^{-1}\right)-X2_k'\cdot\left(Z^{-1}-Z^{-2}\right)\right]=0,$$

$$M_{l\_0}=u_0\frac{Z}{Z-b_l'}\ ,\ l\ \text{is from 1 to}\ N_1', \tag{3.68}$$

$$R_{k\_0}=u_0\frac{Z}{Z-X3_k'+X4_k'\cdot Z^{-1}},\ k\ \text{is from 1 to}\ N_2'. \tag{3.69}$$

Put Eqs.(3.65)-(3.66) into Eq.(3.64) leads to:

$$p_0\left(Z^{\frac{1}{2}}-Z^{-\frac{1}{2}}\right)+u_0\left[-j2\sin\left(\frac{k\Delta x}{2}\right)\right]\cdot \tag{3.70}$$
$$\left[\frac{K_e\Delta t}{\Delta x}+\frac{\Delta t^2}{\Delta x}\sum_{l=1}^{N_1}\frac{a_l}{Z-b_l}+\frac{\Delta t^2}{\Delta x}\sum_{k=1}^{N_2}\frac{X1_k-X2_kZ^{-1}}{Z-X3_k+X4_k\cdot Z^{-1}}\right]=0.$$

Put Eqs.(3.68)-(3.69) into Eq.(3.67) leads to:

$$\frac{\Delta t}{\rho_e\Delta x}p_0\left[-j2\sin\left(\frac{k\Delta x}{2}\right)\right]+u_0\left(Z^{\frac{1}{2}}-Z^{-\frac{1}{2}}\right)\cdot \tag{3.71}$$
$$\left[1+\frac{\Delta t}{\rho_e}\sum_{l=1}^{N_1'}\frac{a_l'}{Z-b_l'}+\frac{\Delta t}{\rho_e}\sum_{k=1}^{N_2'}\frac{X1_k'-X2_k'\cdot Z^{-1}}{Z-X3_k'+X4_k'\cdot Z^{-1}}\right]=0.$$

In a matrix form of Eqs.(3.70)-(3.71):

$$\mathrm{MX}=0, \tag{3.72}$$

$$\mathrm{M}=\begin{bmatrix} Z^{\frac{1}{2}}-Z^{-\frac{1}{2}} & -j2\sin\left(\frac{k\Delta x}{2}\right)\cdot\left[\frac{K_e\Delta t}{\Delta x}+Ca+Cb\right] \\ -j2\sin\left(\frac{k\Delta x}{2}\right)\cdot\frac{\Delta t}{\rho_e\Delta x} & \left(Z^{\frac{1}{2}}-Z^{-\frac{1}{2}}\right)\left(1+Cd+Ce\right) \end{bmatrix}, \tag{3.73}$$

$$X=\begin{Bmatrix} p_0 & u_0 \end{Bmatrix}^{\mathrm{T}}, \tag{3.74}$$

where

$$Ca = \frac{\Delta t^2}{\Delta x} \sum_{l=1}^{N_1} \frac{a_l}{Z - b_l}, \tag{3.75}$$

$$Cb = \frac{\Delta t^2}{\Delta x} \sum_{k=1}^{N_2} \frac{X1_k - X2_k Z^{-1}}{Z - X3_k + X4_k \cdot Z^{-1}}, \tag{3.76}$$

$$Cd = \frac{\Delta t}{\rho_e} \sum_{l=1}^{N_1'} \frac{a_l'}{Z - b_l'}, \tag{3.77}$$

$$Ce = \frac{\Delta t}{\rho_e} \sum_{k=1}^{N_2'} \frac{X1_k' - X2_k' \cdot Z^{-1}}{Z - X3_k' + X4_k' \cdot Z^{-1}}. \tag{3.78}$$

The matrix M is a 4×4 matrix. When the coefficients Ca, Cb, Cd, Ce are all zeros, the matrix M is the same as the matrix for the stability condition in the air.

The matrix X is not the zero vector, which leads to the value of the determinant for the matrix M are zeros. Therefore, the following equation which regards the complex amplification ratio Z are obtained:

$$\begin{aligned} &\left(Z^{\frac{1}{2}} - Z^{-\frac{1}{2}}\right)^2 \left(1 + \frac{\Delta t}{\rho_e} \sum_{l=1}^{N_1'} \frac{a_l'}{Z - b_l'} + \frac{\Delta t}{\rho_e} \sum_{k=1}^{N_2'} \frac{X1_k' - X2_k' \cdot Z^{-1}}{Z - X3_k' + X4_k' \cdot Z^{-1}}\right) \\ &- j^2 4 \sin^2\left(\frac{k\Delta x}{2}\right) \cdot \frac{\Delta t}{\rho_e \Delta x} \\ &\cdot \left[\frac{K_e \Delta t}{\Delta x} + \frac{\Delta t^2}{\Delta x} \sum_{l=1}^{N_1} \frac{a_l}{Z - b_l} + \frac{\Delta t^2}{\Delta x} \sum_{k=1}^{N_2} \frac{X1_k - X2_k Z^{-1}}{Z - X3_k + X4_k \cdot Z^{-1}}\right] = 0. \end{aligned} \tag{3.79}$$

It can be found that the stability of the algorithm is related with the parameters of the designed IIR filters, especially related with the number of the poles. The poles can be real poles or complex poles, and the values of N_1, N_2, N_1' and N_2' can be different. It is difficult to discuss the stability of the algorithm for different kinds of poles and different values of N_1, N_2, N_1' and N_2'.

As a preliminary discussion, how the parameters of the designed IIR filters affect the stability of the algorithm, the following cases are discussed:

(Case A) $N_1 = 1, \quad N_2 = N_1' = N_2' = 0;$

(Case B) $N_2=1,\quad N_1=N_1'=N_2'=0;$

(Case C) $N_1'=1,\quad N_1=N_2=N_2'=0;$

(Case D) $N_2'=1,\quad N_1=N_2=N_1'=0;$

(Case E) $N_1=N_1'=2,\quad N_2=N_2'=0;$

(Case F) $N_1=N_2=N_1'=N_2'=1;$

3.3.2 Stability discussion for Case A

The designed IIR filters for the effective bulk modulus $K_{eq}(\omega)$ and the effective density $\rho_{eq}(\omega)$ are given as:

$$K_{eq}(\omega)=k_0+\sum_{l=1}^{N_1}\frac{r_l}{j\omega-q_l}+\sum_{k=1}^{N_2}\frac{r_k}{j\omega-q_k}+\frac{r_k^*}{j\omega-q_k^*}, \tag{3.80}$$

$$\rho_{eq}(\omega)=k_0'+\sum_{l=1}^{N_1'}\frac{r_l'}{j\omega-q_l'}+\sum_{k=1}^{N_2'}\frac{r_k'}{j\omega-q_k'}+\frac{r_k'^*}{j\omega-q_k'^*}. \tag{3.81}$$

For case A, $N_1=1$, and $N_2=N_1'=N_2'=0$. Then the effective bulk modulus $K_{eq}(\omega)$ and the effective density $\rho_{eq}(\omega)$ are changed to:

$$K_{eq}(\omega)=k_0+\frac{r_1}{j\omega-q_1}, \tag{3.82}$$

$$\rho_{eq}(\omega)=k_0'. \tag{3.83}$$

Then Eq.(3.79) becomes:

$$\begin{aligned}&Z^3-\left(b_1+2-4\sin^2\left(\frac{k\Delta x}{2}\right)\cdot\frac{K_e\Delta t}{\Delta x}\cdot\frac{\Delta t}{\rho_e\Delta x}\right)Z^2\\&+\left(2b_1+1-4b\sin^2\left(\frac{k\Delta x}{2}\right)\cdot\frac{K_e\Delta t}{\Delta x}\cdot\frac{\Delta t}{\rho_e\Delta x}+4\sin^2\left(\frac{k\Delta x}{2}\right)\cdot\frac{\Delta t^3}{\rho_e\Delta x^2}a_1\right)Z-b_1=0,\end{aligned} \tag{3.84}$$

where $a_1=r_1\cdot e^{q_1\Delta t}$, $b_1=e^{q_1\Delta t}$, $K_e=k_0+r_1\Delta t$, $\rho_e=k_0'$.

In Eq.(3.84), the roots are Z_1, Z_2 and Z_3. Here, $-1<Z_1<1$, $-1<Z_2<1$ and $-1<Z_3<1$, which satisfy that the solutions is not increased and diverged at last.

From the Vieta's formulas, the following equations can be obtained:

$$Z_1Z_2Z_3=(-1)^3(-b_1), \tag{3.85}$$

$$Z_1 + Z_2 + Z_3 = -\left[-\left(b_1 + 2 - 4\sin^2\left(\frac{k\Delta x}{2} \right) \cdot \frac{K_e \Delta t}{\Delta x} \cdot \frac{\Delta t}{\rho_e \Delta x} \right) \right]. \tag{3.86}$$

Then the following equations can be obtained:

$$-1 < e^{q_1 \Delta t} < 1, \tag{3.87}$$

$$-3 < e^{q_1 \Delta t} + 2 - 4\sin^2\left(\frac{k\Delta x}{2} \right) \cdot \frac{K_e \Delta t}{\Delta x} \cdot \frac{\Delta t}{\rho_e \Delta x} < 3. \tag{3.88}$$

Eq.(3.87) yields the stability condition in designing the IIR filter for the effective bulk modulus $K_{eq}(\omega)$: the real part of the pole (q_1) should be smaller than 0.

Eq.(3.88) yields the stability condition in the FDTD analysis: the discrete time interval Δt and the discrete spatial interval Δx need to be satisfied as:

$$0 < \sqrt{\frac{K_e}{\rho_e}} \cdot \frac{\Delta t}{\Delta x} < 1. \tag{3.89}$$

3.3.3 Stability discussion for Case B

The designed IIR filters for the effective bulk modulus $K_{eq}(\omega)$ and the effective density $\rho_{eq}(\omega)$ are given as:

$$K_{eq}(\omega) = k_0 + \sum_{l=1}^{N_1} \frac{r_l}{j\omega - q_l} + \sum_{k=1}^{N_2} \frac{r_k}{j\omega - q_k} + \frac{r_k^*}{j\omega - q_k^*}, \tag{3.90}$$

$$\rho_{eq}(\omega) = k_0' + \sum_{l=1}^{N_1'} \frac{r_l'}{j\omega - q_l'} + \sum_{k=1}^{N_2'} \frac{r_k'}{j\omega - q_k'} + \frac{r_k'^*}{j\omega - q_k'^*}. \tag{3.91}$$

For case B, $N_2 = 1$, $N_1 = N_1' = N_2' = 0$. Then the effective bulk modulus $K_{eq}(\omega)$ and the effective density $\rho_{eq}(\omega)$ are changed to:

$$K_{eq}(\omega) = k_0 + \frac{r_1}{j\omega - q_1} + \frac{r_1^*}{j\omega - q_1^*}, \tag{3.92}$$

$$\rho_{eq}(\omega) = k_0', \tag{3.93}$$

where $q_1 = -\alpha_1 + j\beta_1$, $q_1^* = -\alpha_1 - j\beta_1$, $r_1 = \lambda_1 + j\mu_1$, and $r_1^* = \lambda_1 - j\mu_1$.

Then Eqs.(3.79) becomes:

$$Z^4-\left(X3_1+2-4\sin^2\left(\frac{k\Delta x}{2}\right)\cdot\frac{K_e\Delta t}{\Delta x}\cdot\frac{\Delta t}{\rho_e\Delta x}\right)\cdot Z^3$$
$$+\left[X4_1+1+X3_1\cdot\left(2-4\sin^2\left(\frac{k\Delta x}{2}\right)\cdot\frac{K_e\Delta t}{\Delta x}\cdot\frac{\Delta t}{\rho_e\Delta x}\right)+4\sin^2\left(\frac{k\Delta x}{2}\right)\cdot\frac{\Delta t^3}{\rho_e\Delta x^2}\cdot X1_1\right]\cdot Z^2$$
$$-\left[X3_1+X4_1\cdot\left(2-4\sin^2\left(\frac{k\Delta x}{2}\right)\cdot\frac{K_e\Delta t}{\Delta x}\cdot\frac{\Delta t}{\rho_e\Delta x}\right)+4\sin^2\left(\frac{k\Delta x}{2}\right)\cdot\frac{\Delta t^3}{\rho_e\Delta x^2}\cdot X2_1\right]\cdot Z$$
$$+X4_1=0, \tag{3.94}$$

where $X1_1=2\lambda_1\cdot e^{-\alpha_1\Delta t}\cdot\cos(\beta_1\Delta t)-2\mu_1\cdot e^{-\alpha_1\Delta t}\cdot\sin(\beta_1\Delta t)$, $X2_1=2\lambda_1\cdot e^{-2\alpha_1\Delta t}$, $X3_1=2e^{-\alpha_1\Delta t}\cdot\cos(\beta_1\Delta t)$, $X4_1=e^{-2\alpha_1\Delta t}$, $K_e=K_0+2\lambda_1\Delta t$, and $\rho_e=k_0'$.

In Eq.(3.94), the roots are Z_1, Z_2, Z_3 and Z_4. From the Vieta's formulas, the following equations can be obtained:

$$Z_1Z_2Z_3Z_4=(-1)^4\,X4_1, \tag{3.95}$$

$$Z_1+Z_2+Z_3+Z_4=-(-1)\left[X3_1+2-4\sin^2\left(\frac{k\Delta x}{2}\right)\cdot\frac{K_e\Delta t}{\Delta x}\cdot\frac{\Delta t}{\rho_e\Delta x}\right]. \tag{3.96}$$

For each root, $-1<Z_1<1$, $-1<Z_2<1$, $-1<Z_3<1$ and $-1<Z_4<1$. Then the following equations can be obtained:

$$-1<e^{-2\alpha_1\Delta t}<1, \tag{3.97}$$

$$-4<2e^{-\alpha_1\Delta t}\cdot\cos(\beta_1\Delta t)+2-4\sin^2\left(\frac{k\Delta x}{2}\right)\cdot\frac{K_e\Delta t}{\Delta x}\cdot\frac{\Delta t}{\rho_e\Delta x}<4. \tag{3.98}$$

Eq.(3.97) yields the stability condition in designing the IIR filter for the effective bulk modulus $K_{eq}(\omega)$: the real part of the complex poles ($-\alpha_1$) should be smaller than 0.

Eq.(3.87) yields the stability condition in designing the IIR filter: the discrete time interval Δt and the discrete spatial interval Δx need to be satisfied as:

$$0<\sqrt{\frac{K_e}{\rho_e}}\cdot\frac{\Delta t}{\Delta x}<1. \tag{3.99}$$

3.3.4 Stability discussion for Case C

The designed IIR filters for the effective bulk modulus $K_{eq}(\omega)$ and the effective density $\rho_{eq}(\omega)$ are given as:

$$K_{eq}(\omega)=k_0+\sum_{l=1}^{N_1}\frac{r_l}{j\omega-q_l}+\sum_{k=1}^{N_2}\frac{r_k}{j\omega-q_k}+\frac{r_k^*}{j\omega-q_k^*}, \tag{3.100}$$

$$\rho_{eq}(\omega)=k_0'+\sum_{l=1}^{N_1'}\frac{r_l'}{j\omega-q_l'}+\sum_{k=1}^{N_2'}\frac{r_k'}{j\omega-q_k'}+\frac{r_k'^*}{j\omega-q_k'^*}. \tag{3.101}$$

For case C, $N_1'=1$, $N_1=N_2=N_2'=0$. Then the effective bulk modulus $K_{eq}(\omega)$ and the effective density $\rho_{eq}(\omega)$ are changed to:

$$K_{eq}(\omega)=k_0, \tag{3.102}$$

$$\rho_{eq}(\omega)=k_0'+\frac{r_1'}{j\omega-q_1'}. \tag{3.103}$$

Then Eq.(3.79) becomes:

$$\begin{aligned}&Z^3-\left[2-\left(\frac{\Delta t}{\rho_e}a_1'-b_1'\right)-4\sin^2\left(\frac{k\Delta x}{2}\right)\cdot\frac{K_e\Delta t}{\Delta x}\cdot\frac{\Delta t}{\rho_e\Delta x}\right]Z^2\\&+\left[1-2\left(\frac{\Delta t}{\rho_e}a_1'-b_1'\right)-4\sin^2\left(\frac{k\Delta x}{2}\right)\cdot\frac{K_e\Delta t}{\Delta x}\cdot\frac{\Delta t}{\rho_e\Delta x}\cdot b_1'\right]Z\\&+\left(\frac{\Delta t}{\rho_e}a_1'-b_1'\right)=0,\end{aligned} \tag{3.104}$$

where $a_1'=r_1'\cdot e^{q_1'\Delta t}$, $b_1'=e^{q_1'\Delta t}$, $K_e=k_0$, $\rho_e=k_0'+r_1'\Delta t$.

In Eq.(3.104), the roots are Z_1, Z_2 and Z_3. From the Vieta's formulas, the following equations can be obtained:

$$Z_1Z_2Z_3=(-1)^3\left(\frac{\Delta t}{\rho_e}a_1'-b_1'\right), \tag{3.105}$$

$$Z_1+Z_2+Z_3=-(-1)\left[2-\left(\frac{\Delta t}{\rho_e}a_1'-b_1'\right)-4\sin^2\left(\frac{k\Delta x}{2}\right)\cdot\frac{K_e\Delta t}{\Delta x}\cdot\frac{\Delta t}{\rho_e\Delta x}\right]. \tag{3.106}$$

Here, $-1<Z_1<1$, $-1<Z_2<1$ and $-1<Z_3<1$. Then the following equations can be obtained:

$$-1 < e^{q_1'\Delta t} \cdot \left(\frac{r_1'\Delta t}{k_0' + r_1'\Delta t} - 1 \right) < 1, \tag{3.107}$$

$$-4 < 2 - \left(\frac{\Delta t}{\rho_e} a_1' - b_1' \right) - 4\sin^2\left(\frac{k\Delta x}{2} \right) \cdot \frac{K_e \Delta t}{\Delta x} \cdot \frac{\Delta t}{\rho_e \Delta x} < 4. \tag{3.108}$$

Eq.(3.107) yields the stability condition in designing the IIR filter for the effective density $\rho_{eq}(\omega)$: the real part of the pole (q_1') should be smaller than 0;

Eq.(3.108) yields the stability condition in the FDTD analysis, the discrete time interval Δt and the discrete spatial interval Δx need to be satisfied as:

$$0 < \sqrt{\frac{K_e}{\rho_e}} \cdot \frac{\Delta t}{\Delta x} < 1. \tag{3.109}$$

3.3.5 Stability discussion for Case D

The designed IIR filters for the effective bulk modulus $K_{eq}(\omega)$ and the effective density $\rho_{eq}(\omega)$ are given as:

$$K_{eq}(\omega) = k_0 + \sum_{l=1}^{N_1} \frac{r_l}{j\omega - q_l} + \sum_{k=1}^{N_2} \frac{r_k}{j\omega - q_k} + \frac{r_k^*}{j\omega - q_k^*}, \tag{3.110}$$

$$\rho_{eq}(\omega) = k_0' + \sum_{l=1}^{N_1'} \frac{r_l'}{j\omega - q_l'} + \sum_{k=1}^{N_2'} \frac{r_k'}{j\omega - q_k'} + \frac{r_k'^*}{j\omega - q_k'^*}. \tag{3.111}$$

For case D, $N_2' = 1$, $N_1 = N_2 = N_1' = 0$. Then the effective bulk modulus $K_{eq}(\omega)$ and the effective density $\rho_{eq}(\omega)$ are changed to:

$$K_{eq}(\omega) = k_0, \tag{3.112}$$

$$\rho_{eq}(\omega) = k_0' + \frac{r_1'}{j\omega - q_1'} + \frac{r_1'^*}{j\omega - q_1'^*}, \tag{3.113}$$

where $q_1' = -\alpha_1' + j\beta_1'$, $q_1'^* = -\alpha_1' - j\beta_1'$, $r_1' = \lambda_1' + j\mu_1'$, $r_1'^* = \lambda_1' - j\mu_1'$.

Then Eq.(3.79) becomes:

$$
\begin{aligned}
&Z^4-\left[2-\left(\frac{\Delta t}{\rho_e}X1_1'-X3_1'\right)-A\right]Z^3\\
&+\left[\left(X4_1'-\frac{\Delta t}{\rho_e}X2_1'\right)-2\left(\frac{\Delta t}{\rho_e}X1_1'-X3_1'\right)-X3_1'A+1\right]Z^2\\
&+\left[X4_1'A-2\left(X4_1'-\frac{\Delta t}{\rho_e}X2_1'\right)+\left(\frac{\Delta t}{\rho_e}X1_1'-X3_1'\right)\right]Z\\
&+\left(X4_1'-\frac{\Delta t}{\rho_e}X2_1'\right)=0,
\end{aligned}
\tag{3.114}
$$

where $X1_1'=2\lambda_1'\cdot e^{-\alpha_1'\Delta t}\cdot\cos\left(\beta_1'\Delta t\right)-2\mu_1'\cdot e^{-\alpha_1'\Delta t}\cdot\sin\left(\beta_1'\Delta t\right)$, $X2_1'=2\lambda_1'\cdot e^{-2\alpha_1'\Delta t}$, $X3_1'=2e^{-\alpha_1'\Delta t}\cdot\cos\left(\beta_1'\Delta t\right)$, $X4_1'=e^{-2\alpha_1'\Delta t}$, $K_e=k_0$, $\rho_e=k_0'+2\lambda_1'\Delta t$.

In Eq.(3.114):

$$
A=4\sin^2\left(\frac{k\Delta x}{2}\right)\cdot\frac{K_e\Delta t}{\Delta x}\cdot\frac{\Delta t}{\rho_e\Delta x}. \tag{3.115}
$$

In Eq.(3.114), the roots are Z_1, Z_2, Z_3 and Z_4. Here, $-1<Z_1<1$, $-1<Z_2<1$, $-1<Z_3<1$ and $-1<Z_4<1$. From the Vieta's formulas, the following equations can be obtained:

$$
-4<2-\left(\frac{\Delta t}{\rho_e}X1_1'-X3_1'\right)-A<4, \tag{3.116}
$$

$$
-6<\left(X4_1'-\frac{\Delta t}{\rho_e}X2_1'\right)-2\left(\frac{\Delta t}{\rho_e}X1_1'-X3_1'\right)-X3_1'A+1<6, \tag{3.117}
$$

$$
-4<X4_1'A-2\left(X4_1'-\frac{\Delta t}{\rho_e}X2_1'\right)+\left(\frac{\Delta t}{\rho_e}X1_1'-X3_1'\right)<4, \tag{3.118}
$$

$$
-1<X4_1'-\frac{\Delta t}{\rho_e}X2_1'=e^{-2\alpha_1'\Delta t}\cdot\left(\frac{k_0'}{k_0'+2\lambda_1'\Delta t}\right)<1. \tag{3.119}
$$

Eq.(3.119) yields the stability condition in designing the IIR filter for the effective density: the real part of the complex poles ($-\alpha_1'$) should be smaller than 0;

From (3.116)-(3.118), the following equation can be obtained:

$$
-20<\left(X4_1'-2X3_1'+3\right)A<32. \tag{3.120}
$$

In Eq.(3.120), $-8<X4_1'-2X3_1'+3<8$, so $A<4$.

The stability condition in the FDTD analysis: the discrete time interval Δt and the discrete spatial interval Δx need to be satisfied as:

$$0 < \sqrt{\frac{K_e}{\rho_e}} \cdot \frac{\Delta t}{\Delta x} < 1. \tag{3.121}$$

3.3.6 Stability discussion for Case E

The designed IIR filters for the effective bulk modulus $K_{eq}(\omega)$ and the effective density $\rho_{eq}(\omega)$ are given as:

$$K_{eq}(\omega) = k_0 + \sum_{l=1}^{N_1} \frac{r_l}{j\omega - q_l} + \sum_{k=1}^{N_2} \frac{r_k}{j\omega - q_k} + \frac{r_k^*}{j\omega - q_k^*}, \tag{3.122}$$

$$\rho_{eq}(\omega) = k_0' + \sum_{l=1}^{N_1'} \frac{r_l'}{j\omega - q_l'} + \sum_{k=1}^{N_2'} \frac{r_k'}{j\omega - q_k'} + \frac{r_k'^*}{j\omega - q_k'^*}. \tag{3.123}$$

For case E, $N_1 = N_1' = 2$, and $N_2 = N_2' = 0$. Then the effective bulk modulus and the effective density are changed to:

$$K_{eq}(\omega) = k_0 + \frac{r_1}{j\omega - q_1} + \frac{r_2}{j\omega - q_2}, \tag{3.124}$$

$$\rho_{eq}(\omega) = k_0' + \frac{r_1'}{j\omega - q_1'} + \frac{r_2'}{j\omega - q_2'}. \tag{3.125}$$

Then Eq.(3.79) becomes:

$$\begin{aligned}
&\left(Z^2 - 2Z + 1\right)\left[Z^2 - \left(b_1 + b_2\right)Z + b_1 b_2\right] \cdot \\
&\left[Z^2 + \left(\frac{a_1'\Delta t}{\rho_e} + \frac{a_2'\Delta t}{\rho_e} - b_1' - b_2'\right)Z + \left(b_1' b_2' - \frac{a_1' b_2' \Delta t}{\rho_e} - \frac{a_2' b_1' \Delta t}{\rho_e}\right)\right] \\
&- AZ \times \left[Z^2 - \left(b_1' + b_2'\right)Z + b_1' b_2'\right] \cdot \\
&\left[\frac{K_e \Delta t}{\Delta x} Z^2 + \left(\frac{a_1 \Delta t^2}{\Delta x} + \frac{a_2 \Delta t^2}{\Delta x} - \frac{K_e \Delta t b_1}{\Delta x} - \frac{K_e \Delta t b_2}{\Delta x}\right)Z + \left(\frac{K_e \Delta t}{\Delta x} b_1 b_2 - \frac{a_1 \Delta t^2}{\Delta x} b_2 - \frac{a_2 \Delta t^2}{\Delta x} b_1\right)\right] = 0,
\end{aligned} \tag{3.126}$$

where $a_1 = r_1 \cdot e^{q_1 \Delta t}$, $b_1 = e^{q_1 \Delta t}$, $a_2 = r_2 \cdot e^{q_2 \Delta t}$, $b_2 = e^{q_2 \Delta t}$, $a_1' = r_1' \cdot e^{q_1' \Delta t}$, $b_1' = e^{q_1' \Delta t}$, $a_2' = r_2' \cdot e^{q_2' \Delta t}$, $b_2' = e^{q_2' \Delta t}$, $K_e = k_0 + r_1 \Delta t + r_2 \Delta t$, $\rho_e = k_0' + r_1' \Delta t + r_2' \Delta t$.

In Eq.(3.126), the roots are $Z_1,\ Z_2,\ Z_3,\ Z_4,\ Z_5,\ Z_6$. Here, $-1<Z_1<1$, $-1<Z_2<1,\ -1<Z_3<1,\ -1<Z_4<1,\ -1<Z_5<1,\ -1<Z_6<1$. From the Vieta's formulas, the following equations can be obtained:

$$Z_1+Z_2+Z_3+Z_4+Z_5+Z_6 = -\left(\frac{a_1'\Delta t}{\rho_e}+\frac{a_2'\Delta t}{\rho_e}-b_1'-b_2'-b_1-b_2+4\sin^2\left(\frac{k\Delta x}{2}\right)\cdot\frac{K_e\Delta t^2}{\rho_e\Delta x^2}-2\right), \tag{3.127}$$

$$Z_1Z_2Z_3Z_4Z_5Z_6 = b_1b_2\left(b_2'b_1'-\frac{a_1'b_2'\Delta t}{\rho_e}-\frac{a_2'b_1'\Delta t}{\rho_e}\right). \tag{3.128}$$

From Eq.(3.128), the following equation can be obtained:

$$-1\le e^{q_1\Delta t}\ e^{q_2\Delta t}e^{q_1'\Delta t}\ e^{q_2'\Delta t}\left(\frac{k_0'}{k_0'+r_1'\Delta t+r_2'\Delta t}\right)\le 1. \tag{3.129}$$

Eq.(3.129) yields the stability condition in designing the IIR filter for the effective bulk modulus and the effective density: the real part of the poles ($q_1,\ q_2,\ q_1',\ q_2'$) should be smaller than 0.

From Eq.(3.127), the following equation can be obtained:

$$\sin^2\left(\frac{k\Delta x}{2}\right)\cdot\frac{K_e\Delta t^2}{\rho_e\Delta x^2}\le 1. \tag{3.130}$$

Eq.(3.130) yields the stability condition in the FDTD analysis, the discrete time interval Δt and the discrete spatial interval Δx need to be satisfied as:

$$0<\sqrt{\frac{K_e}{\rho_e}}\cdot\frac{\Delta t}{\Delta x}<1. \tag{3.131}$$

3.3.7 Stability discussion for Case F

The designed IIR filters for the effective bulk modulus $K_{eq}(\omega)$ and the effective density $\rho_{eq}(\omega)$ are given as:

$$K_{eq}(\omega)=k_0+\sum_{l=1}^{N_1}\frac{r_l}{j\omega-q_l}+\sum_{k=1}^{N_2}\frac{r_k}{j\omega-q_k}+\frac{r_k^*}{j\omega-q_k^*}, \tag{3.132}$$

$$\rho_{eq}(\omega)=k_0'+\sum_{l=1}^{N_1'}\frac{r_l'}{j\omega-q_l'}+\sum_{k=1}^{N_2'}\frac{r_k'}{j\omega-q_k'}+\frac{r_k'^*}{j\omega-q_k'^*}. \tag{3.133}$$

For case F, $N_1=N_2=N_1'=N_2'=1$. Then the effective bulk modulus and the effective density are changed to:

$$K_{eq}(\omega)=k_0+\frac{r_1}{j\omega-q_1}+\frac{r_2}{j\omega-q_2}+\frac{r_2^*}{j\omega-q_2^*}, \tag{3.134}$$

$$\rho_{eq}(\omega)=k_0'+\frac{r_1'}{j\omega-q_1'}+\frac{r_2'}{j\omega-q_2'}+\frac{r_2'^*}{j\omega-q_2'^*}, \tag{3.135}$$

where $q_2=-\alpha_1+j\beta_1$, $q_2^*=-\alpha_1-j\beta_1$, $r_2=\lambda_1+j\mu_1$, $r_2^*=\lambda_1-j\mu_1$, $q_2'=-\alpha_1'+j\beta_1'$, $q_2'^*=-\alpha_1'-j\beta_1'$, $r_2'=\lambda_1'+j\mu_1'$, $r_2'^*=\lambda_1'-j\mu_1'$.

Then Eq.(3.79) becomes:

$$\begin{aligned}
&\left(Z^2-2Z+1\right)\left(Z-b_1\right)\left(Z^2-X3_1Z+X4_1\right)\cdot\\
&\left[\begin{array}{l}\left(Z-b_1'\right)\left(Z^2-X3_1'Z+X4_1'\right)+\dfrac{a_1'\Delta t}{\rho_e}\left(Z^2-X3_1'Z+X4_1'\right)\\ +\dfrac{\Delta t}{\rho_e}\left(X1_1'Z-X2_1'\right)\left(Z-b_1'\right)\end{array}\right]\\
&-AZ\left(Z-b_1'\right)\left(Z^2-X3_1'Z+X4_1'\right)\cdot\\
&\left[\begin{array}{l}\dfrac{K_e\Delta t}{\Delta x}\left(Z-b_1\right)\left(Z^2-X3_1Z+X4_1\right)+\dfrac{a_1\Delta t^2}{\Delta x}\left(Z^2-X3_1Z+X4_1\right)\\ +\dfrac{\Delta t^2}{\Delta x}\left(X1_1Z-X2_1\right)\left(Z-b_1\right)\end{array}\right]=0,
\end{aligned} \tag{3.136}$$

where $a_1=r_1\cdot e^{q_1\Delta t}$, $b_1=e^{q_1\Delta t}$; $a_1'=r_1'\cdot e^{q_1'\Delta t}$, $b_1'=e^{q_1'\Delta t}$;
$X1_1=2\lambda_1\cdot e^{-\alpha_1\Delta t}\cdot\cos(\beta_1\Delta t)-2\mu_1\cdot e^{-\alpha_1\Delta t}\cdot\sin(\beta_1\Delta t)$, $X2_1=2\lambda_1\cdot e^{-2\alpha_1\Delta t}$,
$X3_1=2e^{-\alpha_1\Delta t}\cdot\cos(\beta_1\Delta t)$, $X4_1=e^{-2\alpha_1\Delta t}$;
$X1_1'=2\lambda_1'\cdot e^{-\alpha_1'\Delta t}\cdot\cos(\beta_1'\Delta t)-2\mu_1'\cdot e^{-\alpha_1'\Delta t}\cdot\sin(\beta_1'\Delta t)$, $X2_1'=2\lambda_1'\cdot e^{-2\alpha_1'\Delta t}$,
$X3_1'=2e^{-\alpha_1'\Delta t}\cdot\cos(\beta_1'\Delta t)$, $X4_1'=e^{-2\alpha_1'\Delta t}$; $K_e=k_0+r_1\Delta t+2\lambda_1\Delta t$,
$\rho_e=k_0'+r_1'\Delta t+2\lambda_1'\Delta t$.

In Eq.(3.136), the roots are $Z_1,Z_2,Z_3,Z_4,Z_5,Z_6,Z_7,Z_8$. Here, $-1<Z_1<1$, $-1<Z_2<1$, $-1<Z_3<1$, $-1<Z_4<1$, $-1<Z_5<1$, $-1<Z_6<1$, $-1<Z_7<1$, $-1<Z_8<1$. From the Vieta's formulas, the following equations can be obtained:

$$Z_1 + Z_2 + Z_3 + Z_4 + Z_5 + Z_6 + Z_7 + Z_8 = b_1' - \frac{a_1'\Delta t}{\rho_e} + X3_1' - X1_1'\frac{\Delta t}{\rho_e} + X3_1 + b_1 + 2 - 4\sin^2\left(\frac{k\Delta x}{2}\right)\cdot\frac{K_e\Delta t^2}{\rho_e\Delta x^2}, \tag{3.137}$$

$$Z_1Z_2Z_3Z_4Z_5Z_6Z_7Z_8 = X4_1b_1 \times \left(-X4_1'b_1' + \frac{a_1'\Delta t}{\rho_e}X4_1' + X2_1'\frac{\Delta t}{\rho_e}b_1'\right). \tag{3.138}$$

From Eq.(3.138), the following equation can be obtained:

$$-1 \le e^{q_1\Delta t}\cdot e^{q_1'\Delta t}\cdot e^{-2\alpha_1\Delta t}\cdot e^{-2\alpha_1'\Delta t}\left(\frac{k_0'}{k_0' + r_1'\Delta t + 2\lambda_1'\Delta t}\right) \le 1. \tag{3.139}$$

Eq.(3.139) yields the stability condition in designing the IIR filter for the effective bulk modulus and the effective density: the real part of the poles (q_1, q_1', $-\alpha_1$, $-\alpha_1'$) should be smaller than 0.

From Eq.(3.137), the following equations can be obtained:

$$-10 \le b_1' - \frac{a_1'\Delta t}{\rho_e} + X3_1' - X1_1'\frac{\Delta t}{\rho_e} + X3_1 + b_1 - 4\sin^2\left(\frac{k\Delta x}{2}\right)\cdot\frac{K_e\Delta t^2}{\rho_e\Delta x^2} \le 6, \tag{3.140}$$

$$-1 \le b' - \frac{a_1'\Delta t}{\rho_e} = \left(1 - \frac{r_1'\Delta t}{k_0' + r_1'\Delta t + 2\lambda_1'\Delta t}\right)e^{q_1'\Delta t} \le 1, \tag{3.141}$$

$$-2 \le X3_1 = 2e^{-\alpha_1\Delta t}\cdot\cos\left(\beta_1\Delta t\right) \le 2, \tag{3.142}$$

$$-1 \le b_1 = e^{q_1\Delta t} \le 1, \tag{3.143}$$

$$X3_1' - X1_1'\frac{\Delta t}{\rho_e} = 2e^{-\alpha_1'\Delta t}\left[\frac{\mu_1'\Delta t}{k_0' + r_1'\Delta t + 2\lambda_1'\Delta t}\sin\left(\beta_1'\Delta t\right) + \frac{k_0' + r_1'\Delta t + \lambda_1'\Delta t}{k_0' + r_1'\Delta t + 2\lambda_1'\Delta t}\cos\left(\beta_1'\Delta t\right)\right]. \tag{3.144}$$

Set:

$$A = a\sin\left(\beta_1'\Delta t\right) + b\cos\left(\beta_1'\Delta t\right), \tag{3.145}$$

$$a = \frac{\mu_1'\Delta t}{k_0' + r_1'\Delta t + 2\lambda_1'\Delta t},\quad b = \frac{k_0' + r_1'\Delta t + \lambda_1'\Delta t}{k_0' + r_1'\Delta t + 2\lambda_1'\Delta t},\quad t = \sin^{-1}\left(\frac{b}{\sqrt{a^2 + b^2}}\right). \tag{3.146}$$

Then:

$$A = \sqrt{a^2 + b^2}\,\sin\left(\beta_1'\Delta t + t\right), \tag{3.147}$$

$$\sqrt{a^2+b^2}=\sqrt{\frac{\left(\mu_1'\Delta t\right)^2+\left(k_0'+r_1'\Delta t+\lambda_1'\Delta t\right)^2}{\left(k_0'+r_1'\Delta t+2\lambda_1'\Delta t\right)^2}}. \tag{3.148}$$

In Eq.(3.148), Δt is the discrete time in the FDTD analysis, the order of which is near 10^{-6}. λ_1 and μ_1 are the real part and imaginary part of r_2', and the order of these two values are close. The examples can be found in table 4-3 and table 4-10. Therefore, the following equation can be obtained:

$$-2\le X3_1'-X1_1'\frac{\Delta t}{\rho_e}=2e^{-\alpha_1'\Delta t}\sqrt{a^2+b^2}\sin\left(\beta_1'\Delta t+t\right)\le 2. \tag{3.149}$$

Then Eq.(3.140) can be simplified:

$$\sin^2\left(\frac{k\Delta x}{2}\right)\cdot\frac{K_e\Delta t^2}{\rho_e\Delta x^2}\le 1. \tag{3.150}$$

Eq.(3.150) yields the stability condition in the FDTD analysis, the discrete time interval Δt and the discrete spatial interval Δx need to be satisfied as:

$$0<\sqrt{\frac{K_e}{\rho_e}}\cdot\frac{\Delta t}{\Delta x}<1. \tag{3.151}$$

3.3.8 Conclusion

It can be concluded that for the EF-FDTD algorithm, the stability conditions are given as:

(1) The stability condition in designing the IIR filter for the effective bulk modulus and the effective density:

The real part of the poles (the real poles and the complex poles) should be smaller than 0;

(2) The stability condition in the FDTD analysis:

For 1-dimensinal EF-FDTD algorithm, the discrete time interval Δt and the discrete spatial interval Δx need to be satisfied as:

$$0<\sqrt{\frac{K_e}{\rho_e}}\cdot\frac{\Delta t}{\Delta x}<1. \tag{3.152}$$

For 2-dimensinal EF-FDTD algorithm, the discrete time interval Δt and the discrete spatial interval Δx need to be satisfied as:

$$0 < \sqrt{\frac{K_e}{\rho_e}} \cdot \frac{\Delta t}{\Delta x} < \frac{1}{\sqrt{2}}. \tag{3.153}$$

For 3-dimensinal EF-FDTD algorithm, the discrete time interval Δt and the discrete spatial interval Δx need to be satisfied as:

$$0 < \sqrt{\frac{K_e}{\rho_e}} \cdot \frac{\Delta t}{\Delta x} < \frac{1}{\sqrt{3}}. \tag{3.154}$$

3.4 Conclusion

In this chapter, the EF-FDTD algorithm in the porous material with rigid flame is proposed. The IIR filters for the effective bulk modulus and the effective density are designed. Based on the equivalent fluid model, the wave equations in frequency domain are firstly changed to Z domain by using the Z-transform theory, and then transformed to time domain. Then, the equations for the EF-FDTD algorithm are obtained. The equations for the 1-dimensional EF-FDTD algorithm, 2-dimensional EF-FDTD algorithm and 3-dimensional EF-FDTD algorithm are introduced. The stability condition of the proposed EF-FDTD algorithm is discussed.

Chapter 4 VALIDATION OF THE EF_FDTD ALGORITHM

4.1 Introduction

In this chapter, the proposed EF-FDTD algorithm is validated. In section 4.2, the 1-dimensional EF-FDTDT algorithm is validated by comparing the numerical analysis and the experiment. Multiple-layered materials are measured and simulated by using 1-dimensional EF-FDTDT algorithm. In section 4.3, the 2-dimensional EF-FDTDT algorithm is validated under the oblique incidence of the sound. 4 layers of the porous material are simulated. How to treat the boundary condition and how to calculate the surface impedance are discussed. In section 4.4, treatment for shaped porous material in FDTD analysis is discussed. The errors caused by the staircase approximation method are also discussed. In section 4.5, the EF-FDTD algorithm is contrasted with the exiting Rayleigh method.

4.2 Validation of the 1-dimensional EF-FDTD algorithm

4.2.1 Configuration for the simulation cases

Firstly, the proposed EF-FDTD algorithm is validated at the normal incidence of the sound. Numerical analysis and acoustical measurement of multi-layer porous materials are conducted to validate the 1-dimensional EF-FDTD algorithm. In order to construct the multi-layer material samples, 2 separate porous materials are used: one is glasswool 24k (GW 24k) with thickness of 0.05m, and the other one is glasswool 32k (GW 32k) with thickness of 0.025m.

As shown in Fig.4.1, two simulation cases are set. In the first configuration, the multi-layered porous material (constructed by one layer of GW 32k and one layer of GW 24k) is set backed by a rigid wall. In case (b), an air gap of 2cm is set between the multi-layered porous material and the backed rigid wall. The thickness of GW 32k is 0.025m and that for GW 24k is 0.05m.

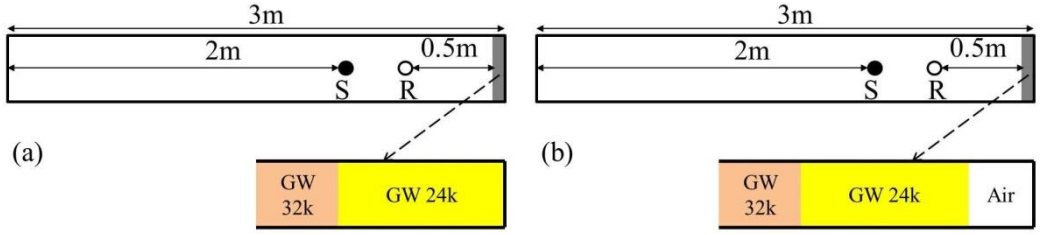

Fig.4.1 Two simulation cases: S represents the sound source, R represents the receiving point;

The sound field is computed within the distance of 3m from the rigid termination. At the receiving point R, the incident wave directly from the sound source S and the reflected wave from the surface of the porous materials can be separated.

The discrete spatial interval Δx is 0.001m, and the discrete time interval Δt is 1.0339×10^{-6}s. Δx and Δt satisfy the following equations:

$$\frac{c_0\Delta t}{\Delta x}\le\frac{1}{\sqrt{2}}\quad\text{and}\quad\frac{\Delta t}{\Delta x}\sqrt{\frac{K_e}{\rho_e}}\le\frac{1}{\sqrt{2}}. \tag{4.1}$$

For the initial condition, the spatial distribution of the sound source is [26]:

$$p=\begin{cases}0.5+0.5\cdot\cos\left(\pi r/R\right) & if \quad r\le R\\ 0 & if \quad r>R\end{cases}. \tag{4.2}$$

Here, the radius of the sound source is represented as R, which is set to be "$100\cdot\Delta x$". r represents the distance between the position of the grid and the center of the sound source.

4.2.2 The boundary condition

In the two simulation cases shown in Fig.4.1, there exist the following boundary conditions:

(1) The boundary between porous material and the rigid wall;

(2) The boundary between air and the rigid wall;

(3) The boundary between the air and the porous material;

(4) The boundary between the porous material and the porous material;

For boundary condition (1) and (2), the particle velocity is set on the boundary, and is equal to 0. For boundary condition (3) and (4), the configuration is shown in Fig.4.2.

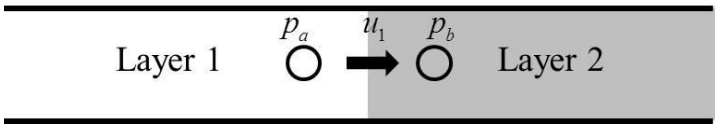

Fig.4.2 Boundary condition setting for (3) and (4)

In Fig.4.2, layer 1 and layer 2 can be different combinations of different porous materials, or combinations of the air and porous materials. p_a is the sound pressure in layer 1, adjacent to the boundary interface; p_b is the sound pressure in layer 2, adjacent to the boundary interface; u_1 is the is the particle velocity, at the boundary between layer 1 and layer 2, which can be calculated by:

$$u_1^{n+1}=u_1^{n}-\frac{\Delta t}{\tilde{\rho}\Delta x}\left[p_b^{n+\frac{1}{2}}-p_a^{n+\frac{1}{2}}\right]. \tag{4.3}$$

In Eq.(4.3), $\tilde{\rho}$ is the arithmetic averaged density[61]. If layer 1 is the porous material A and layer 2 is the air, or layer 1 is the air and layer 2 is the porous material A, $\tilde{\rho}$ is determined by:

$$\tilde{\rho} = \frac{\rho_0 + \rho_e(A)}{2}. \tag{4.4}$$

If layer 1 is the porous material A and layer 2 is the porous material B, or layer 1 is porous material B and layer 2 is porous material A, $\tilde{\rho}$ is determined by:

$$\tilde{\rho} = \frac{\rho_e(A) + \rho_e(B)}{2}. \tag{4.5}$$

4.2.3 The IIR filter design

The testing samples are circular with diameter of 29mm, prepared for the measurement in the B&K impedance tube (Type: 4206). The measurement system is illustrated in Fig.4.3.

Fig.4.3 The measurement system

The characteristic impedance $Z_c(\omega)$ and the wave number $k(\omega)$ for GW 24k and GW 32k are measured in the B&K impedance tube by using the 2-cavity method[62]. Figure 4.4 shows the characteristic impedances of two porous materials, normalized by the characteristic impedance of the air.

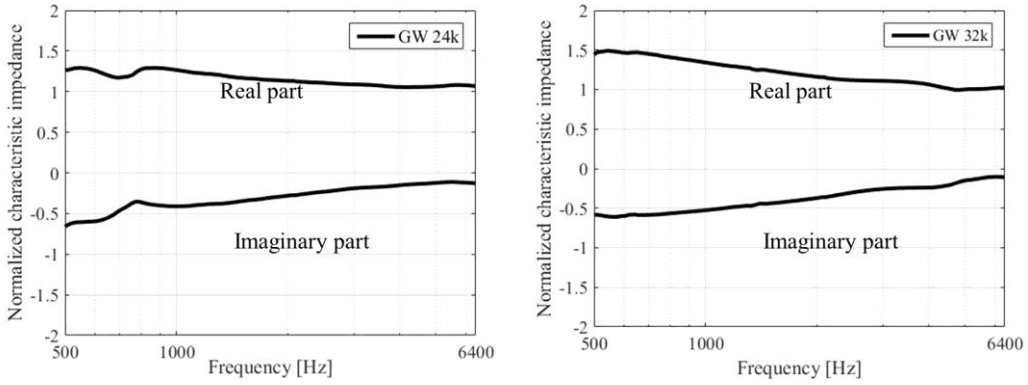

Fig.4.4 The normalized characteristic impedance.

In Fig.4.5, the wave numbers for GW 24k and GW 32k are plotted, normalized by the wave number of the air.

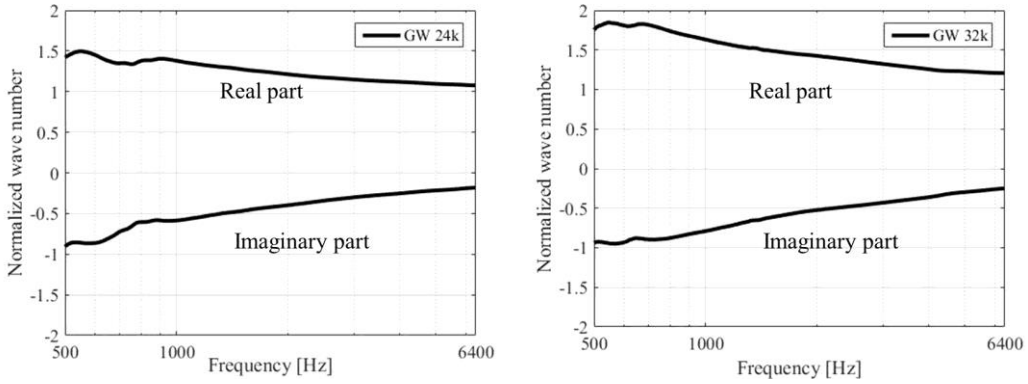

Fig.4.5 The normalized wave number.

In above figures, the measured values fluctuate at the low frequency. The reason is that the two samples are measured in small impedance tube, and the effective frequency range is from 500 Hz to 6400 Hz.

Based on the measured characteristic impedance and the wave number, the effective bulk modulus $K_{eq}(\omega)$ and the effective density $\rho_{eq}(\omega)$ are calculated by:

$$K_{eq}(\omega) = \omega Z_c(\omega)/k(\omega), \tag{4.6}$$

$$\rho_{eq}(\omega) = Z_c(\omega)k(\omega)/\omega. \tag{4.7}$$

The effective bulk modulus $K_{eq}(\omega)$ is designed as the form of the IIR filter, whose form is given in Eq.(4.7). An example of designing IIR filter by using MATLAB program can be found in appendix A.

$$K_{eq}(\omega) = k_0 + \sum_{l=1}^{N_1} \frac{r_l}{j\omega - q_l} + \sum_{k=1}^{N_2} \left(\frac{r_k}{j\omega - q_k} + \frac{r_k^*}{j\omega - q_k^*} \right). \tag{4.8}$$

The designed IIR filters for GW 24K and GW 32K are given in Fig.4.6. The parameters in the designed IIR filter are presented in table 4-1 and table 4-2. For GW 24K, The IIR filter is designed having two real poles. That is $N_1 = 2$. For GW 32K, The IIR filter is designed having one real pole and two complex poles. That is $N_1 = 1$, and $N_2 = 1$.

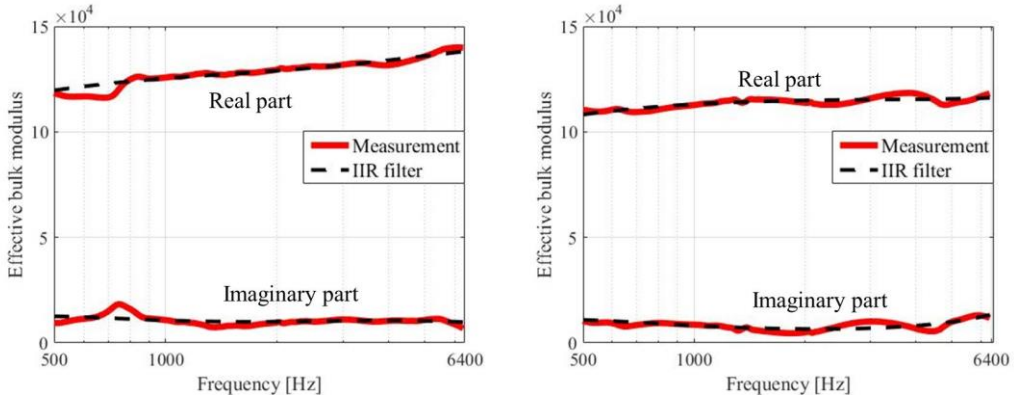

Fig.4.6 The measured effective bulk modulus and the designed IIR filters. The left is for GW 24k, and the right is for GW 32k.

Table 4-1 Designed IIR filter for the effective bulk modulus of GW 24k

k_0	q	r
144930.2897	-31600.5677	-555723999.1887
	-2265.6325	-51982576.3129

Table 4-2 Designed IIR filter for the effective bulk modulus of GW 32k

k_0	q	r
120138.0785	-2260.1676	-48588745.3601
	-10117.7281+j 73553.2044	558688111.1862+j248129940.9187
	-10117.7281-j 73553.2044	558688111.1862-j248129940.9187

The effective bulk modulus $\rho_{eq}(\omega)$ is designed as IIR filter, whose form is:

$$\rho_{eq}(\omega) = k_0' + \sum_{l=1}^{N_1'} \frac{r_l'}{j\omega - q_l'} + \sum_{k=1}^{N_2'} \left(\frac{r_k'}{j\omega - q_k'} + \frac{r_k'^*}{j\omega - q_k'^*} \right). \tag{4.9}$$

The designed IIR filters for GW 24K and GW 32K are given in Fig.4.7. The parameters in the designed IIR filters are presented in table 4-3 and table 4-4. For GW 24K, The IIR filter is designed having one real pole and two complex poles. That is $N_1' = 1$, and $N_2' = 1$. For GW 32K, The IIR filter is designed having two real poles. That is $N_1' = 2$.

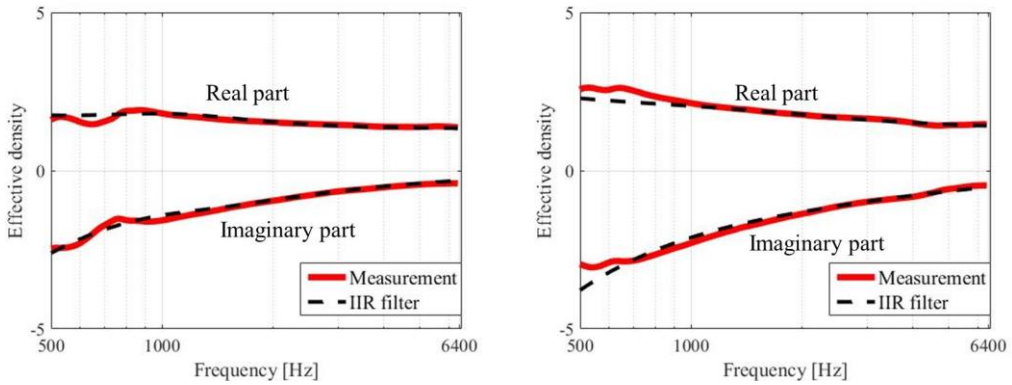

Fig.4.7 The measured effective density and the designed IIR filters. The left is for GW 24k, and the right is for GW 32k.

Table 4-3 Designed IIR filter for the effective density of GW 24k

k_0'	q'	r'
1.3196	-187.0139	8618.4141
	-4737.5433+j5196.6259	2051.1203+j1211.0797
	-4737.5433-j5196.6259	2051.1203-j1211.0797

Table 4-4 Designed IIR filter for the effective density of GW 32k

k_0'	q'	r'
1.3364	-13242.8538	10695.5419
	-161.4689	11325.7349

4.2.4 The results

The sound pressure and the particle velocity are both calculated in air and in porous materials. In the air, the FDTD formulations can be found in section 2.1. In porous materials, the EF-FDTD formulations can be found in section 3.2.4.2. For the boundary conditions, the EF-FDTD formulations can be found in section 4.2.2. In Fig.4.8, for two simulation cases, the calculated sound pressures at the receiving point R are plotted.

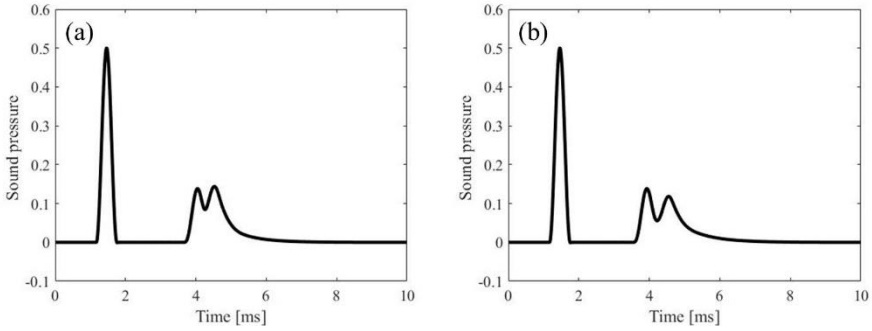

Fig.4.8 The calculated sound pressures at the receive point R for simulation cases.

As shown in Fig.4.8, the directly incident sound pressure (from 1ms to 3ms) and the reflected sound pressure (from 3ms to 7ms) are completely separated. Then, the absorption coefficient can be calculated by:

$$\alpha(\omega) = 1 - \left| \frac{P_{ref}(\omega)}{P_{inc}(\omega)} \right|^2, \tag{4.10}$$

where $P_{inc}(\omega)$ and $P_{ref}(\omega)$ are the frequency responses of the incident sound pressure and the reflected sound pressure, respectively.

In Fig.4.9, the calculated absorption coefficients for two samples are compared with the measurement. The calculated absorption coefficient generally agrees well with the measured result from 500 Hz to 6.4 kHz.

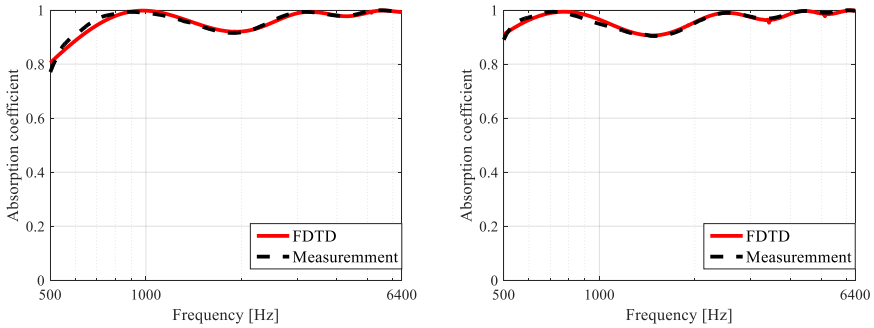

Fig.4.9 The calculated absorption coefficient, compared with the measurement.

4.2.5 Discussion of the IIR filter design

4.2.5.1 Designing different IIR filters

The IIR filter can be designed having different kinds of real poles and different kinds of complex poles. When using different IIR filters in the EF-FDTD algorithm, the accuracy is different, and the calculation time is different. In this section, how the IIR filter affects the accuracy of the EF-FDTD algorithm, and how the IIR filter affects the calculation time are discussed.

The porous material of glass wool 24k (GW 24k) is used in the discussion. As shown in Fig.4.10, 3 kinds of the IIR filters for the effective bulk modulus are designed. In Fig.4.10, the total number of the poles is N ($N = N_1 + 2N_2$), N_1 is the total number of real poles, and N_2 is the total number of the pair of complex poles. The first one is designed having one real poles, that is $N = 1\left(N_1 = 1, N_2 = 0\right)$; The second one is designed having two real poles, that is $N = 2\left(N_1 = 2, N_2 = 0\right)$; The third one is designed having one real pole and two complex poles, that is $N = 3\left(N_1 = 1, N_2 = 1\right)$;

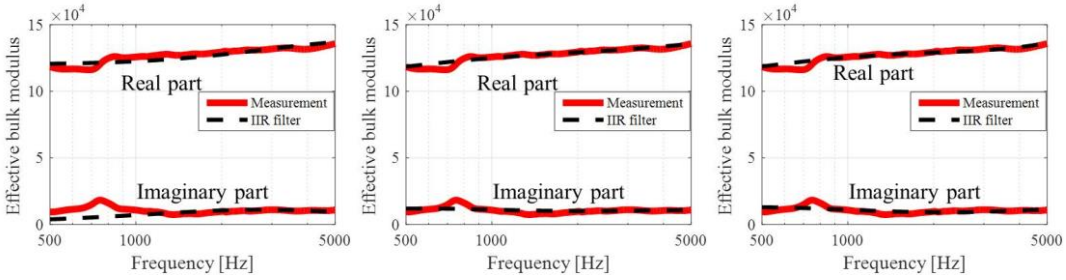

Fig.4.10 3 kinds of the IIR filters for the effective bulk modulus of GW 24k

Table 4-5 For the effective bulk modulus, parameters of the designed IIR filter

k_0	q	r
139964.4015	-12654.2418	-297555528.3745

Table 4-6 For the effective bulk modulus, parameters of the designed IIR filter with two real poles

k_0	q	r
145885.0072	-35234.3977	-635833268.3042
	-2409.5776	-55217477.0634

Table 4-7 For the effective bulk modulus, parameters of designed IIR filter with one real pole and two complex poles

k_0	q	r
135115.3640	-2873.6165	-68685389.4420
	-24504.4073+j 39219.5372	195185042.5799+j276730808.7809
	-24504.4073-j 39219.5372	195185042.5799-j276730808.7809

As shown in Fig.4.11, 3 kinds of the IIR filters for the effective density are designed. In the figure, the total number of the poles is N' ($N' = N_1' + 2N_2'$), N_1' is the total number of real poles, and N_2' is the number of the pair of complex poles. The first one is designed having one real pole, that is $N' = 1\left(N_1' = 1, N_2' = 0\right)$; The second one is designed having two real poles, that is $N' = 2\left(N_1' = 2, N_2' = 0\right)$; The third one is designed having one real pole and two complex poles, that is $N' = 3\left(N_1' = 1, N_2' = 1\right)$;

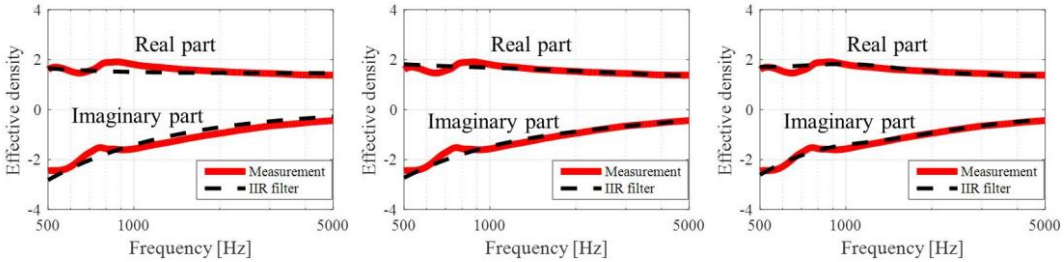

Fig.4.11 3 kinds of the IIR filters for the effective density of GW 24k

Table 4-8 For the effective density, the designed IIR filter with one real pole

k_0'	q'	r'
1.4563	-225.5857	8910.1182

Table 4-9 For the effective density, the designed IIR filter with two real poles

k_0'	q'	r'
1.2635	-15831.9455	7097.6779
	-143.4454	8334.4139

Table 4-10 For the effective density, the designed IIR filter with one real pole and two complex pole

k_0'	q'	r'
1.3271	-210.8527	8861.0697
	-3974.1786+j 5150.2429	1798.7949+j 1242.1857
	-3974.1786-j 5150.2429	1798.7949-j 1242.1857

The errors are expressed as follows:

$$E_{br}=\frac{\sum_{f=500\mathrm{Hz}}^{5000\mathrm{Hz}}\left|1-\frac{real\left(K_{IIR}\right)}{real\left(K_{meas}\right)}\right|}{N},\qquad E_{bi}=\frac{\sum_{f=5000\mathrm{Hz}}^{5000\mathrm{Hz}}\left|1-\frac{imaginary\left(K_{IIR}\right)}{imaginary\left(K_{meas}\right)}\right|}{N},\tag{4.11}$$

$$E_{dr}=\frac{\sum_{f=500\mathrm{Hz}}^{5000\mathrm{Hz}}\left|1-\frac{real\left(\rho_{IIR}\right)}{real\left(\rho_{meas}\right)}\right|}{N},\qquad E_{di}=\frac{\sum_{f=500\mathrm{Hz}}^{5000\mathrm{Hz}}\left|1-\frac{imaginary\left(\rho_{IIR}\right)}{imaginary\left(\rho_{meas}\right)}\right|}{N},\tag{4.12}$$

where N is the number of the discrete frequency points from 100Hz to 5000Hz. K_{IIR} and ρ_{IIR} are the designed IIR filters for the effective bulk modulus and the effective density, respectively. K_{meas} and ρ_{meas} are the measured values for the effective bulk modulus and the effective density, respectively.

The errors between the designed IIR filter for the effective bulk modulus and the measured value are given in table 4-11. It can be found that E_{br} is smallest when $N=3$, and E_{bi} is smallest when $N=2$.

Table 4-11 The errors between the designed IIR filter for the effective bulk modulus and the measured value.

	$N=1$ $(N_1=1, N_2=0)$	$N=2$ $(N_1=2, N_2=0)$	$N=3$ $(N_1=1, N_2=1)$
E_{br}	0.0146	0.0081	0.0074
E_{bi}	0.1393	0.0761	0.0830

The errors between the designed IIR filter for the effective density and the measured value are given in table 4-12. It can be found that E_{dr} is smallest when $N'=3$, and E_{di} is smallest when $N'=2$.

Table 4-12 The errors between the designed IIR filter for the effective density and the measured values.

	$N'=1$ $(N_1'=1, N_2'=0)$	$N'=2$ $(N_1'=2, N_2'=0)$	$N'=3$ $(N_1'=1, N_2'=1)$
E_{dr}	0.0560	0.0302	0.0296
E_{di}	0.2675	0.0378	0.0635

4.2.5.2 Discuss how the IIR filter affects the accuracy

The following simulation is set. The sound field is computed within the distance of 3m from the rigid termination. The thickness of the GW 24k is 0.05m. The discrete spatial interval Δx is set to be 0.001m, and the discrete time interval Δt is set to be 1.02×10^{-6}s. the sound source is added by using Eq.(4.2).

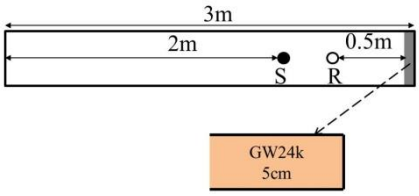

Fig. 4.12 The sound field for the simulation: S represents the sound source, R represents the receiving point;

The calculated sound absorption coefficient coefficients α_{FDTD} are contrasted with the measured values α_{meas}.The errors are calculated by:

$$E_{ab}=\frac{\sum_{f=500\,\mathrm{Hz}}^{5000\,\mathrm{Hz}}\left|1-\frac{\alpha_{FDTD}}{\alpha_{meas}}\right|}{N}. \tag{4.13}$$

In Fig.4.13, the calculated sound absorption coefficients are compared with the measured values. The errors are given in table 4-13. It can be found that the error is largest when $N=1,N'=1$.The error is smallest when $N=3,N'=2$. The errors are close when $N=2,N'=2$, $N=3,N'=2$ and $N=3,N'=3$.

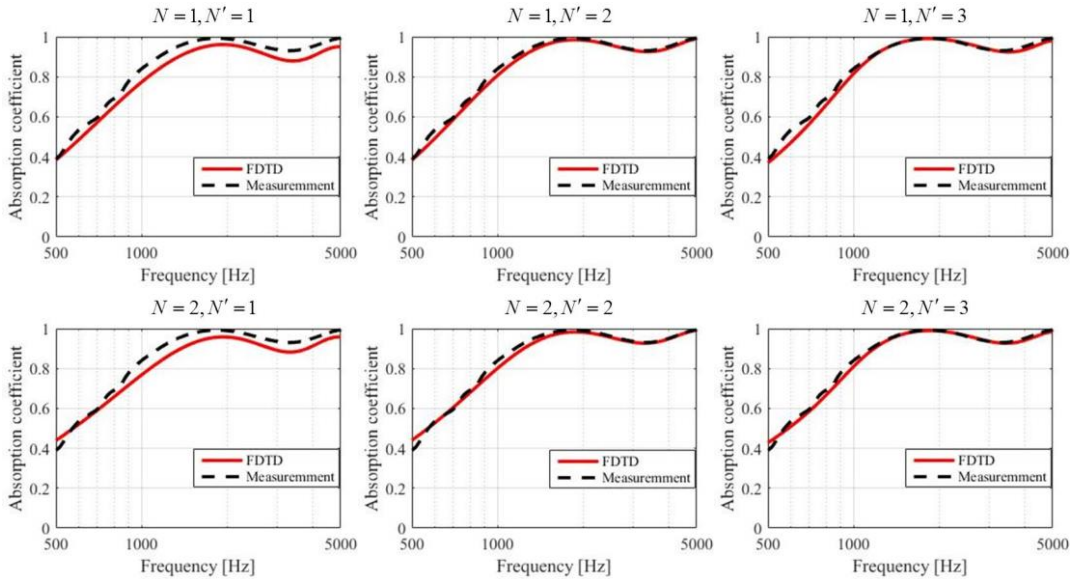

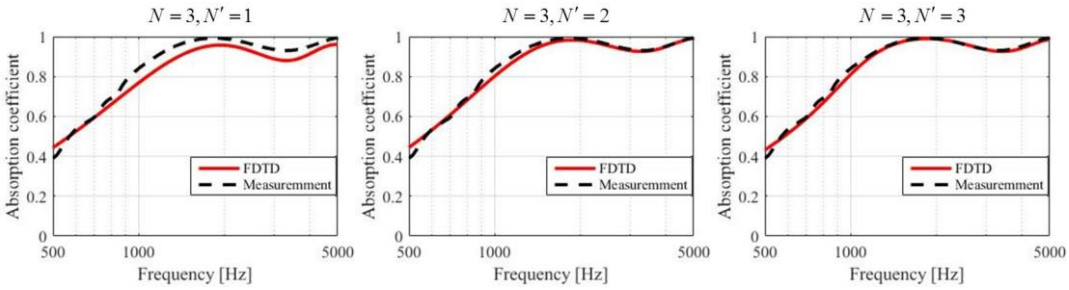

Fig.4.13 The calculated absorption coefficients and the measured values.

Table 4-13 The errors between the calculated absorption coefficients and the measured values.

	$N=1$ $(N_1=1, N_2=0)$	$N=2$ $(N_1=2, N_2=0)$	$N=3$ $(N_1=1, N_2=1)$
$N'=1$ $(N_1'=1, N_2'=0)$	0.0638	0.0275	0.0307
$N'=2$ $(N_1'=1, N_2'=0)$	0.0432	0.0102	0.0101
$N'=3$ $(N_1'=1, N_2'=0)$	0.0439	0.0113	0.0104

4.2.5.3 Discuss how the IIR filter affects the calculation time

The following simulation is set. The discrete spatial interval Δx is set to be 0.01m, and the discrete time interval Δt is set to be 9×10^{-6}s. the sound source is added by using Eq.(4.2).

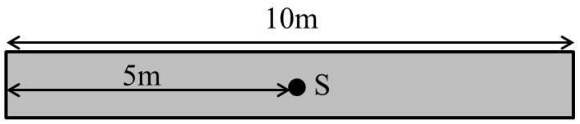

Fig.4.14 The sound field for the simulation: S represents the sound source, PM represents the porous material of GW 24k;

The calculation time and the occupied memory of the computer are given in table 4-14. It can be seen the calculation time is shortest when $N=1, N'=1$. The calculation time is largest when $N=3, N'=3$.

Table 4-14 The calculation time and the occupied memory in the computer.

	$N=1$ $(N_1=1, N_2=0)$	$N=2$ $(N_1=2, N_2=0)$	$N=3$ $(N_1=1, N_2=1)$
$N'=1$ $(N_1'=1, N_2'=0)$	76KB 36s	98KB 43s	111KB 56s
$N'=2$ $(N_1'=1, N_2'=0)$	84KB 40s	106KB 48s	118KB 61s
$N'=3$ $(N_1'=1, N_2'=0)$	107KB 53s	129KB 66s	141KB 76s

4.2.5.4 Conclusion

From the results in table 4-13 and table 4-14, considering the calculation time, the occupied memory in the computer and the accuracy of the calculated absorption coefficient, the directions of designing the best IIR filters are given as follows:

(1) For the effective bulk modulus, the best IIR filter is having two real poles;

(2) For the effective density, the best IIR filter is having two real poles;

4.3 Validation of the 2-dimensional EF-FDTD algorithm

4.3.1 Configuration for the simulation case

In section 4.3, the 2-dimensional EF-FDTD algorithm is validated under the oblique incidence of the sound. As shown in Fig.4.15. There are 4 layers of the porous materials. The angle of oblique incidence is θ. R is located at the surface of the first layer (layer 1).

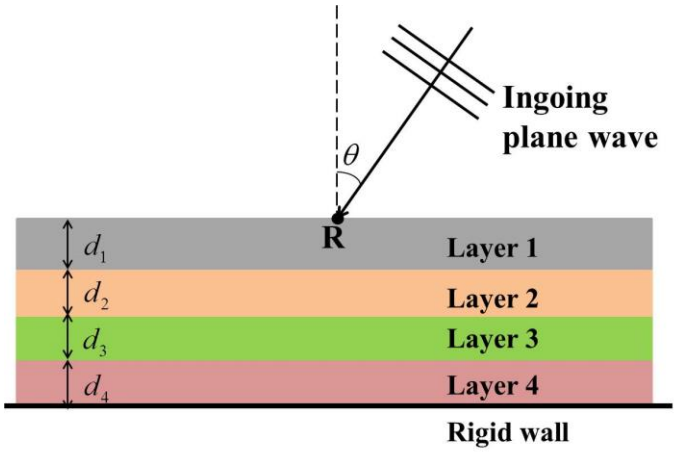

Fig.4.15 Configuration of the simulation case.

The surface impedance is used to validate the algorithm. For the theory, the surface impedance $Z(R)$ can be calculated as follows[32].

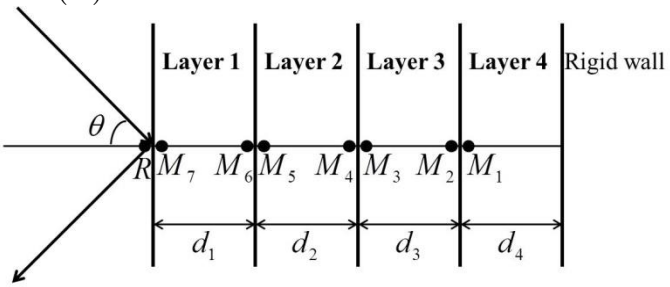

Fig.4.16 layers of the porous material backed by a rigid wall.

The characteristic impedance (layer 1: $Z_c(1)$, layer 2: $Z_c(2)$, layer 3: $Z_c(3)$, layer 4: $Z_c(4)$) and the wave number (layer 1: $k(1)$, layer 2: $k(2)$, layer 3: $k(3)$, layer 4: $k(4)$) are calculated by using Miki model.

The point M_1 is on the surface of the porous material layer 4. The theoretical value of the surface impedance $Z(M_1)$ is given by:

$$Z(M_1) = -j\frac{Z_c(4)k(4)}{k_3}\cot(k_3 d_4), \tag{4.14}$$

$$k_3 = \sqrt{k(4)^2 - (k_0 \sin\theta)^2}. \tag{4.15}$$

In Eq.(4.15), k_0 is the wave number in the air ($k_0 = \omega/c_0$).

The point M_2 is in the porous material layer 4, and adjacent to the boundary surface between layer 3 and layer 4. The value of $Z(M_2)$ is equal to the value of $Z(M_1)$. The point M_3 is on the surface of layer 3, and adjacent to the boundary surface between layer 2 and layer 3. The surface impedance $Z(M_3)$ is calculated by

$$Z(M_3) = \frac{Z_c(3)k(3)}{k_3}\left[\frac{-jZ(M_2)\cot(k_3 d_3) + Z_c(3)k(3)/k_3}{Z(M_2) - j(Z_c(3)k(3)/k_3)\cot(k_3 d_3)}\right], \tag{4.16}$$

$$k_3 = \sqrt{k(3)^2 - (k_0 \sin\theta)^2}. \tag{4.17}$$

The point M_4 is in the porous material layer 2, and adjacent to the boundary surface between layer 2 and layer 3. The value of $Z(M_4)$ is equal to the value of $Z(M_3)$. The point M_5 is on the surface of layer 2. The value of $Z(M_5)$ is calculated by using Eq.(4.16), $Z(M_2)$ being replaced by $Z(M_4)$, d_3 being replaced by d_2, $Z_c(3)$ being replaced by $Z_c(2)$, and $k(3)$ being replaced by $k(2)$.

In the same way, the values of $Z(M_6)$ and $Z(M_7)$ can be calculated. Finally, the surface impedance $Z(R)$ can be obtained, which is equal to $Z(M_7)$.

In this simulation, 4 layers of the porous material are constructed from the following porous materials. The parameters of the designed IIR filters are given in Appendix B.

PM A: the porous material A (flow resistivity: $5000\ \mathrm{Nm^{-4}s}$);

PM B: the porous material B (flow resistivity: $10000\ \mathrm{Nm^{-4}s}$);

PM C: the porous material C (flow resistivity: $15000\ \mathrm{Nm^{-4}s}$);

PM D: the porous material D (flow resistivity: $20000\ \mathrm{Nm^{-4}s}$);

4.3.2 Case (1) for the simulation

4.3.2.1 FDTD setting and the boundary condition

For case (1), the sound field setting for the FDTD analysis is shown in Fig.4.17. The four boundaries of the computation domain are set to be rigid wall. 4 layers of the porous material are constructed by PM A, PM B, PM C and PM D. The flow resistivity of the different layer is: $\sigma(A)=5000\ \mathrm{Nm^{-4}s}$, $\sigma(B)=10000\ \mathrm{Nm^{-4}s}$, $\sigma(C)=15000\ \mathrm{Nm^{-4}s}$, $\sigma(D)=20000\ \mathrm{Nm^{-4}s}$. The thickness of the different porous material layer is both 3cm.

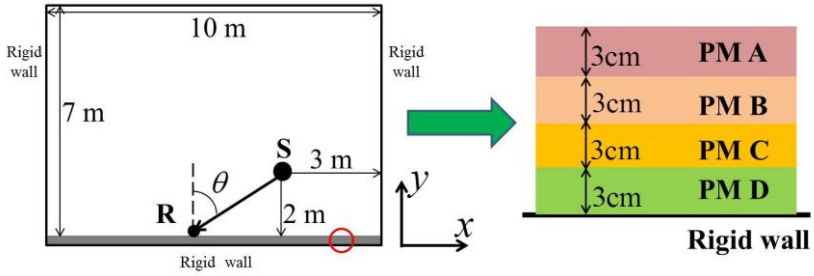

Fig.4.17 The 2-dimensional computation domain for case (1).

In the FDTD analysis, the discrete time interval Δt is 1.75×10^{-6} s, and the discrete space intervals Δx and Δy are both 0.002m. The stability conditions are satisfied:

$$\frac{c_0\Delta t}{\Delta x}\le\frac{1}{\sqrt{2}}\quad\text{and}\quad\frac{\Delta t}{\Delta x}\sqrt{\frac{K_e}{\rho_e}}\le\frac{1}{\sqrt{2}},\tag{4.18}$$

where c_0 is the sound speed in the air.

The sound source S is given in Eq.(4.19), where α and τ_0 are the constants for determining the frequency characteristics of the sound source[63]. Here, τ_0 is set to be $180\times\Delta t$, and α is set to be $(4/\tau_0)^2$.

$$S(t)=\begin{cases}\exp\left(-\alpha(t-\tau_0)^2\right), & 0\le t\le 2\tau_0\\ 0, & \text{others}\end{cases}.\tag{4.19}$$

The sound pressure at the position of the sound source (sx,sy) is updated by[61]:

$$p^{n+1/2}(sx,sy)=p^{n-1/2}(sx,sy)+S\left[(n-1/2)\Delta t\right].\tag{4.20}$$

At the boundary between the air and the porous material A, the particle velocities in y direction are continuous. In Fig.4.18, the particle velocity v at the boundary surface is calculated by Eq.(4.21).

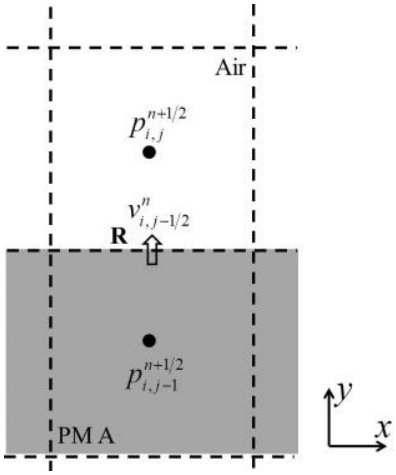

Fig. 4.18 The boundary condition for Case (1); R is the receiving point at the boundary between air and porous material layer A.

$$v_{i,j-1/2}^{n+1} = v_{i,j-1/2}^{n} - \frac{\Delta t}{\tilde{\rho}\Delta x}\left[p_{i,j}^{n+1/2} - p_{i,j-1}^{n+1/2} \right], \tag{4.21}$$

where $\tilde{\rho}$ is the averaged density of the air and the porous material layer A, calculated by using (4.4).

4.3.2.2 Impedance calculating method

Based on the calculated results, the surface impedance $Z(R)$ is calculated by:

$$Z(R) = -\frac{P_{i,j-1/2}^{n+1/2}(\omega)}{V_{i,j-1/2}^{n}(\omega)}, \tag{4.22}$$

where $V_{i,j-1/2}^{n}(\omega)$ is the frequency response of the particle velocity $v_{i,j-1/2}^{n}$ (shown in Fig.4.18); $P_{i,j\text{-}1/2}^{n+1/2}(\omega)$ is the frequency response of the averaged sound pressure, which is calculated by:

$$P_{i,j-1/2}^{n+1/2}(\omega) = \frac{P_{i,j}^{n+1/2}(\omega) + P_{i,j-1}^{n+1/2}(\omega)}{2}, \tag{4.23}$$

where $P_{i,j}^{n+1/2}(\omega)$ and $P_{i,j-1}^{n+1/2}(\omega)$ are the frequency responses of the sound pressure $p_{i,j}^{n+1/2}$ and $p_{i,j-1}^{n+1/2}$ (shown in Fig.4.18), respectively;

4.3.2.3 The results

At the receiving point R, for different incident angles (0°, 20°, 40°, 50°,60°,70°), the calculated averaged sound pressures and the calculated particle velocities are given in are plotted in Fig.4.19 and Fig.4.20, respectively.

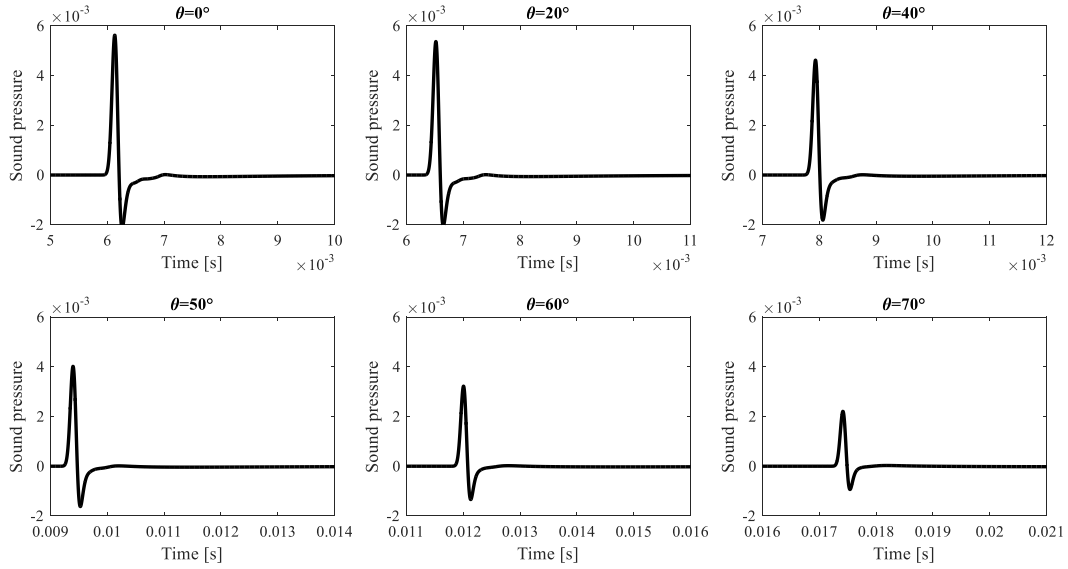

Fig.4.19 Case (1): the averaged sound pressures at different incident angle θ.

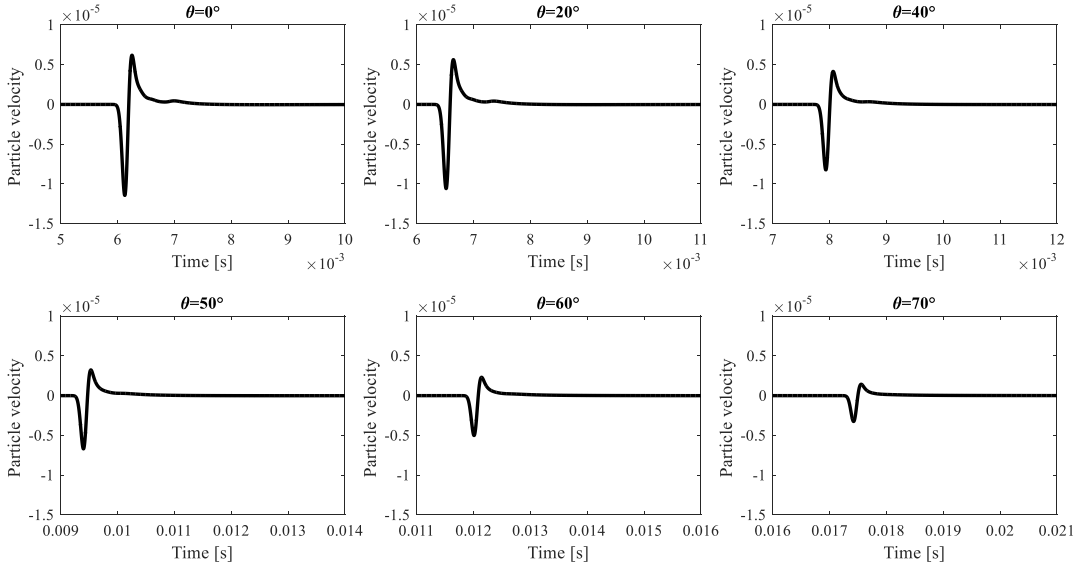

Fig.4.20 Case (1): the particle velocities at different incident angle θ.

At the receiving point R, for different incident angles (0°, 20°, 40°, 50°,60°,70°), the calculated surface impedances (normalized by the characteristic impedance of the air) are compared with the theoretical values, as shown in Fig.4.21.

At all calculated incident angles, the calculated surface impedances agrees well with the theoretical values from 100Hz to 5000Hz.

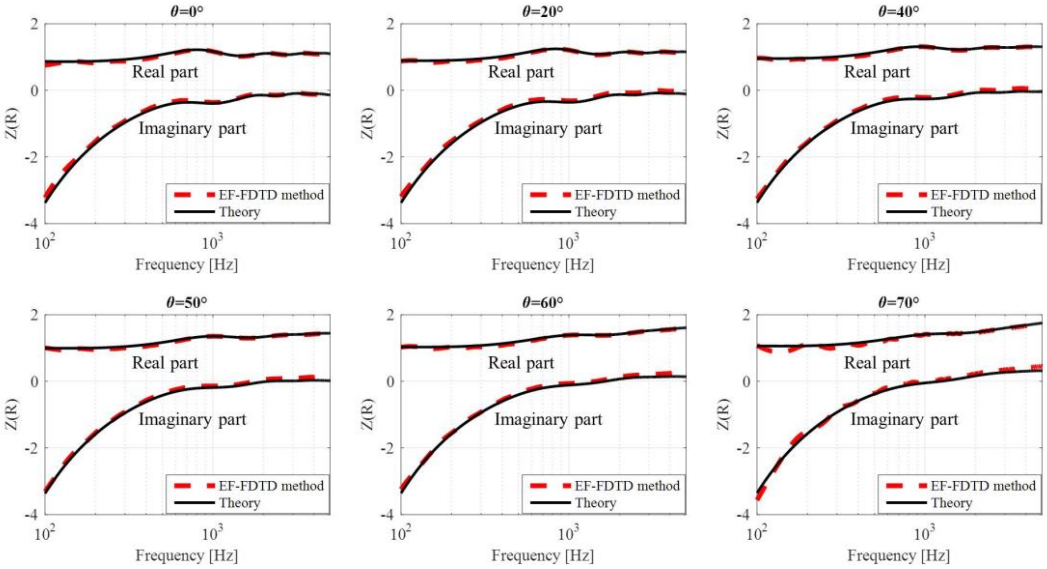

Fig.4.21 Case (1): the calculated and theoretical surface impedance at different incident angle.

4.3.3 Case (2) for the simulation

For case (2), the sound field setting for the FDTD analysis is shown in Fig.4.22. The four boundaries of the computation domain are set to be rigid wall. 4 layers of the porous material are constructed by PM D, PM C, PM B and PM A. The flow resistivity of the different porous material layer is: $\sigma(D)=20000\ \mathrm{Nm^{-4}s}$, $\sigma(C)=15000\ \mathrm{Nm^{-4}s}$, $\sigma(B)=10000\ \mathrm{Nm^{-4}s}$, $\sigma(A)=5000\ \mathrm{Nm^{-4}s}$. The thickness of the different porous material layer is both 3cm.

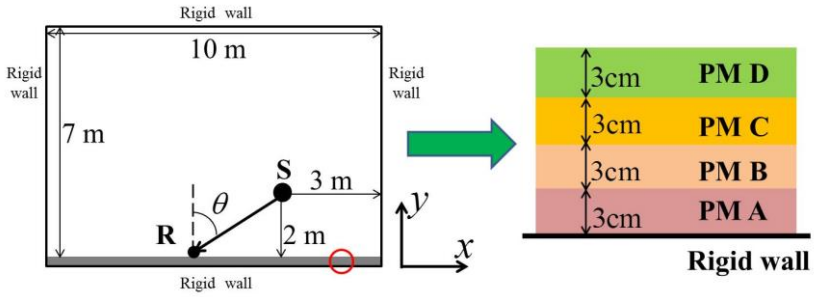

Fig.4.22 The computation domain for Case (2) in the FDTD analysis.

For the boundary between the air and the porous material D, the normal particle velocity components in the y direction are continuous. The particle velocity v is set on the boundary surface, which is calculated by Eq.(4.21), where $\tilde{\rho}$ is the arithmetic averaged density of the air and the porous material layer D.

At the receiving point R, for different incident angles (0°, 20°, 40°, 50°,60°,70°), the calculated averaged sound pressures and the calculated particle velocities are given in Fig.4.23 and Fig.4.24, respectively.

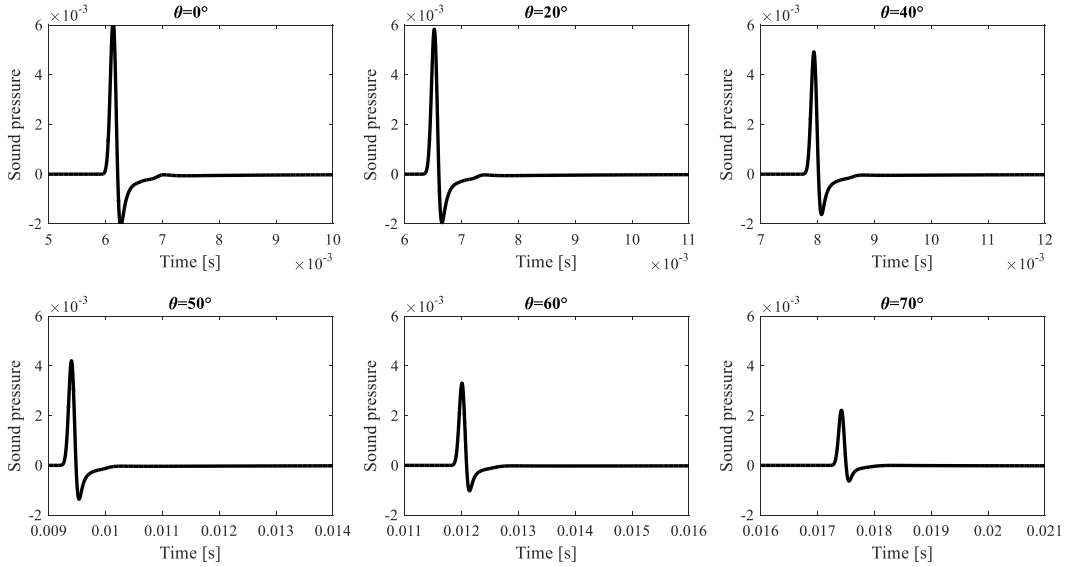

Fig.4.23 Case (2): the averaged sound pressure at different incident angle θ.

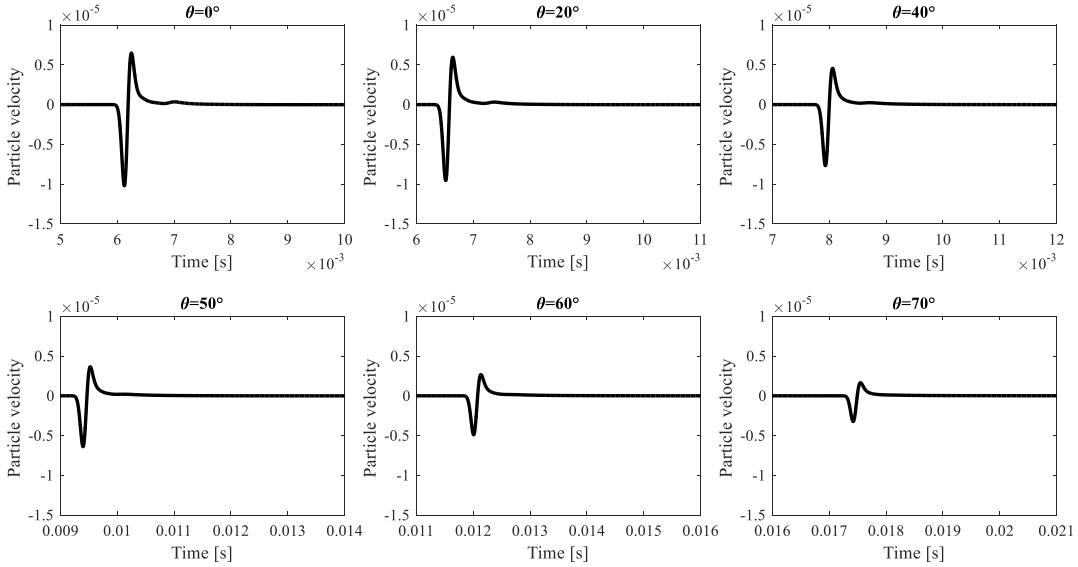

Fig.4.24 Case (2): the particle velocity at different incident angle θ.

At the receiving point R, for different incident angles (0°, 20°, 40°, 50°,60°,70°), the calculated surface impedances (normalized by the characteristic

impedance of the air) are compared with the theoretical values, as shown in Fig.4.25. At all calculated incident angles, the calculated surface impedances agrees well with the theoretical values from 100Hz to 5000Hz.

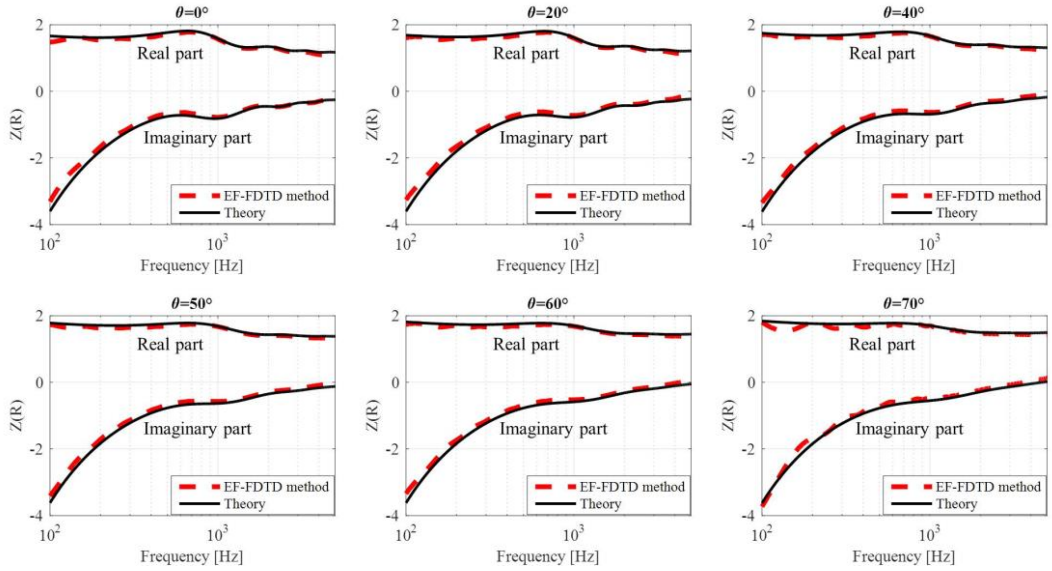

Fig.4.25 Case (2): the calculated and theoretical surface impedance at different incident angle.

4.3.4 Case (3) for the simulation

For case (3), the sound field setting for the FDTD analysis is shown in Fig.4.26. The four boundaries of the computation domain are set to be rigid wall. 4 layers of the porous material are constructed by PM C, PM A, PM D and PM B. The flow resistivity for the different layer is: $\sigma(C)=15000\ \mathrm{Nm^{-4}s}$, $\sigma(A)=5000\ \mathrm{Nm^{-4}s}$, $\sigma(D)=20000\ \mathrm{Nm^{-4}s}$, $\sigma(B)=10000\ \mathrm{Nm^{-4}s}$. The thickness for the different porous material layer is both 3cm.

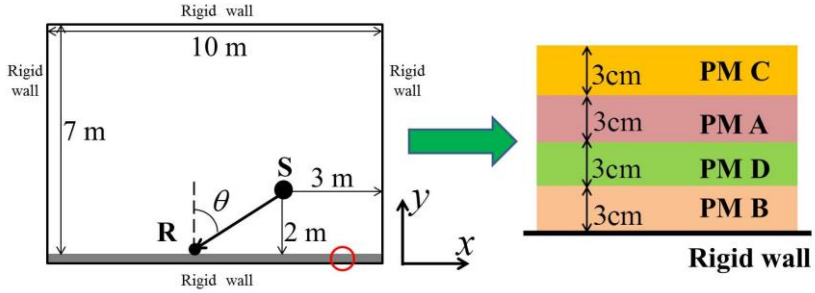

Fig.4.26 The computation domain for Case (3) in the FDTD analysis.

For the boundary between the air and the porous material, the normal particle velocity components in the y direction are continuous. The particle velocity v is set on the boundary, which is calculated by Eq.(4.21), where $\tilde{\rho}$ is the arithmetic averaged density of the air and the porous material layer C.

At the receiving point R, for different incident angles (0°, 20°, 40°, 50°,60°,70°), the calculated averaged sound pressures and the calculated particle velocities are given in Fig.4.27 and Fig.4.28, respectively.

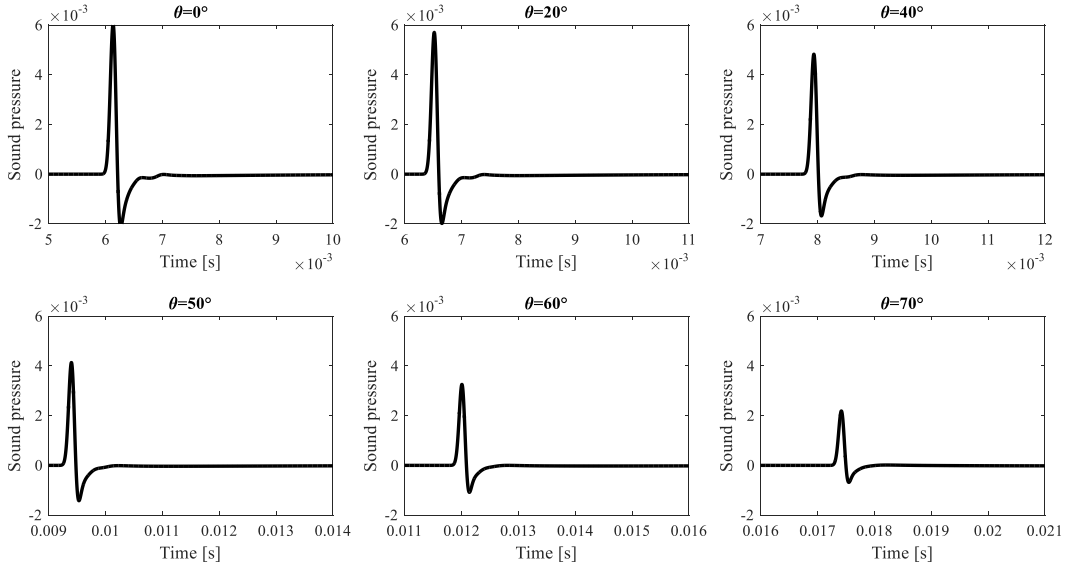

Fig.4.27 Case (3): the averaged sound pressure at different incident angle θ.

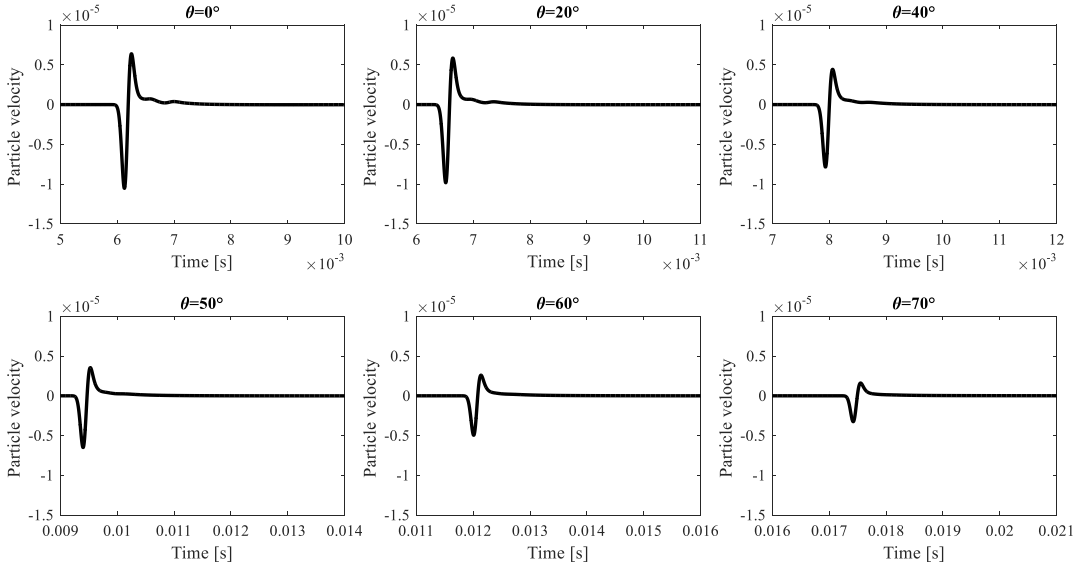

Fig.4.28 Case (3): the particle velocity at different incident angle θ.

At the receiving point R, for different incident angles (0°, 20°, 40°, 50°,60°,70°), the calculated surface impedances (normalized by the characteristic

impedance of the air) are compared with the theoretical values, as shown in Fig.4.29. At all calculated incident angles, the calculated surface impedances agrees well with the theoretical values from 100Hz to 5000Hz.

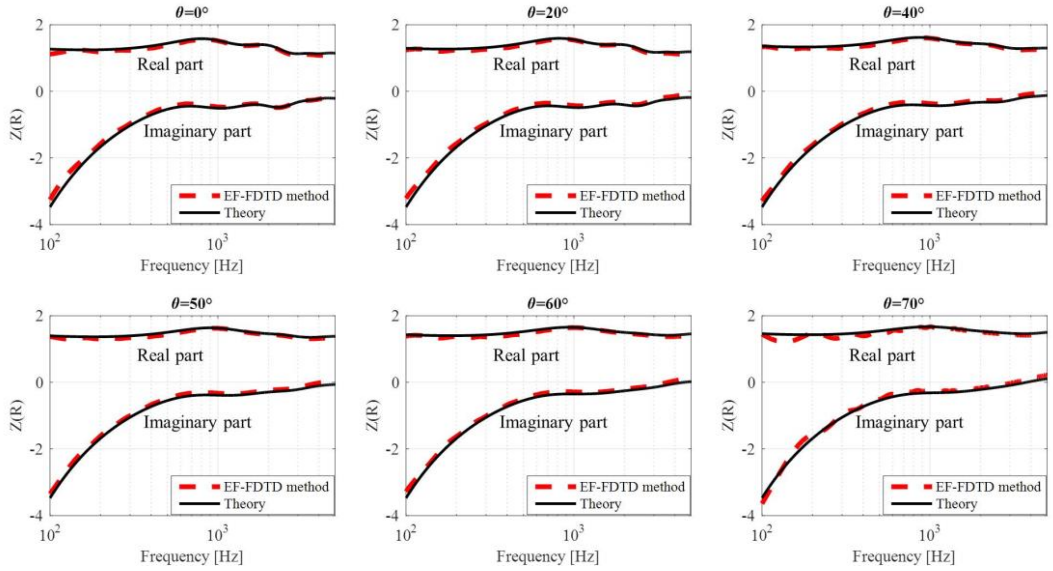

Fig.4.29 Case (3): At the receiving point R, the calculated and theoretical surface impedance at different incident angle.

4.3.5 Case (4) for the simulation

For case (4), the sound field setting for the FDTD analysis is shown in Fig.4.30. The four boundaries of the computation domain are set to be rigid wall. 4 layers of the porous materials are constructed by PM B, PM D, PM A and PM C. The flow resistivity for each porous materials is: $\sigma(B)=10000\ \mathrm{Nm^{-4}s}$, $\sigma(D)=20000\ \mathrm{Nm^{-4}s}$, $\sigma(A)=5000\ \mathrm{Nm^{-4}s}$, $\sigma(C)=15000\ \mathrm{Nm^{-4}s}$. The thickness of the different porous material layer is both 3cm.

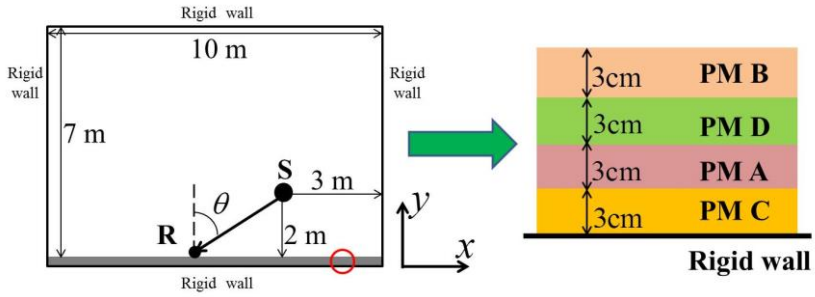

Fig.4.30 The computation domain for Case (4) in the FDTD analysis.

For the boundary between porous material layer B and air, the particle velocity v is set at the boundary surface, which is calculated by Eq.(4.21), where $\tilde{\rho}$ is the averaged density for the porous material layer B and the air.

At the receiving point R, for different incident angles (0°, 20°, 40°, 50°,60°,70°), the calculated averaged sound pressures are given in Fig.4.31.

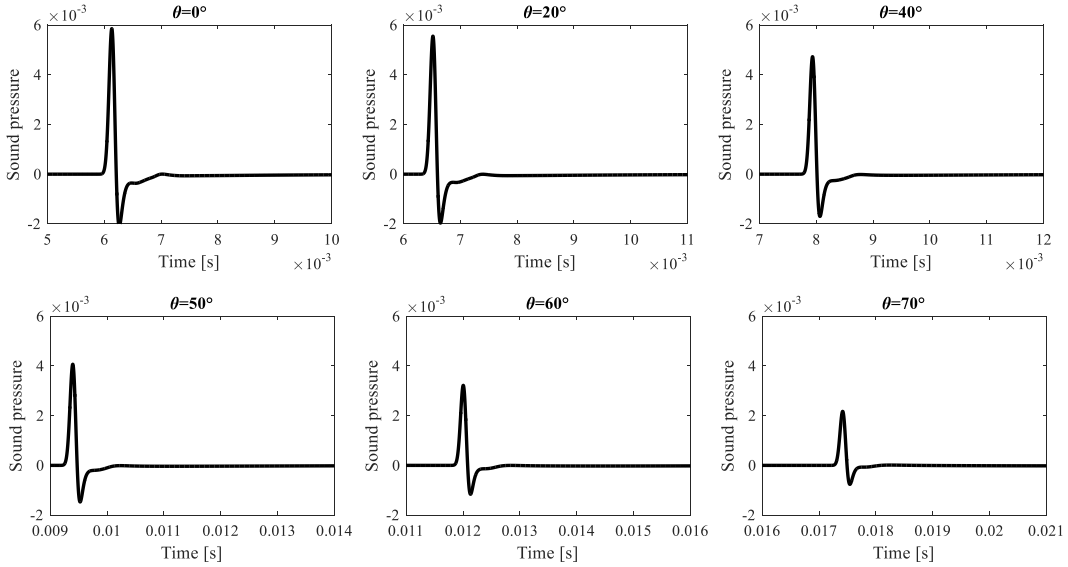

Fig.4.31 Case (4): the averaged sound pressure at different incident angle θ.

At the receiving point R, for different incident angles (0°, 20°, 40°, 50°,60°,70°), the calculated particle velocities are given in Fig.4.32.

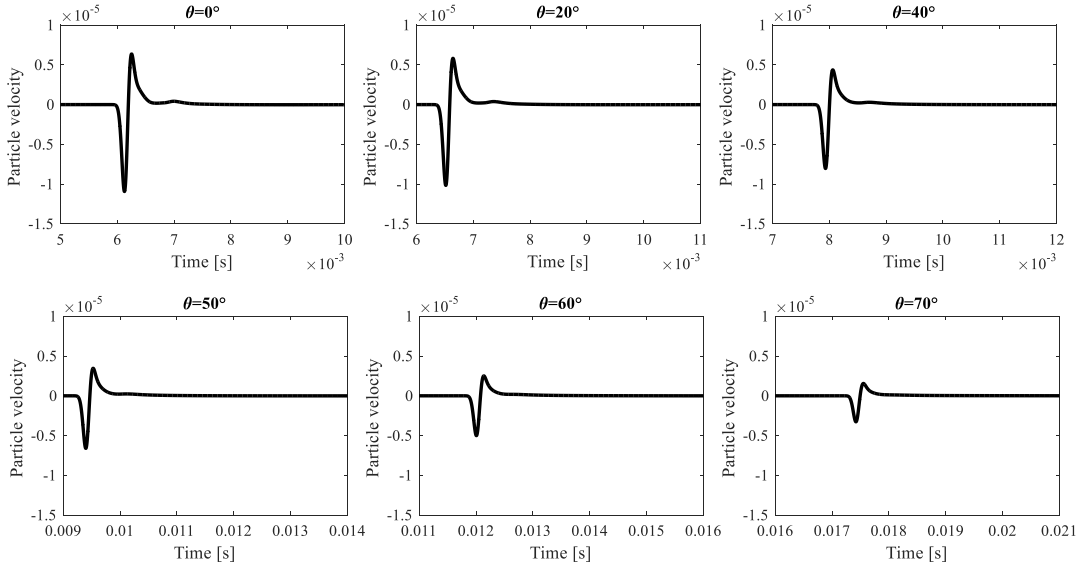

Fig. 4.32 Case (4): the particle velocity at different incident angle θ.

At the receiving point R, for different incident angles (0°, 20°, 40°, 50°,60°,70°), the calculated surface impedances (normalized by the characteristic

impedance of the air) are compared with the theoretical values, as shown in Fig.4.33. At all calculated incident angles, the calculated surface impedances agrees well with the theoretical values from 100Hz to 5000Hz.

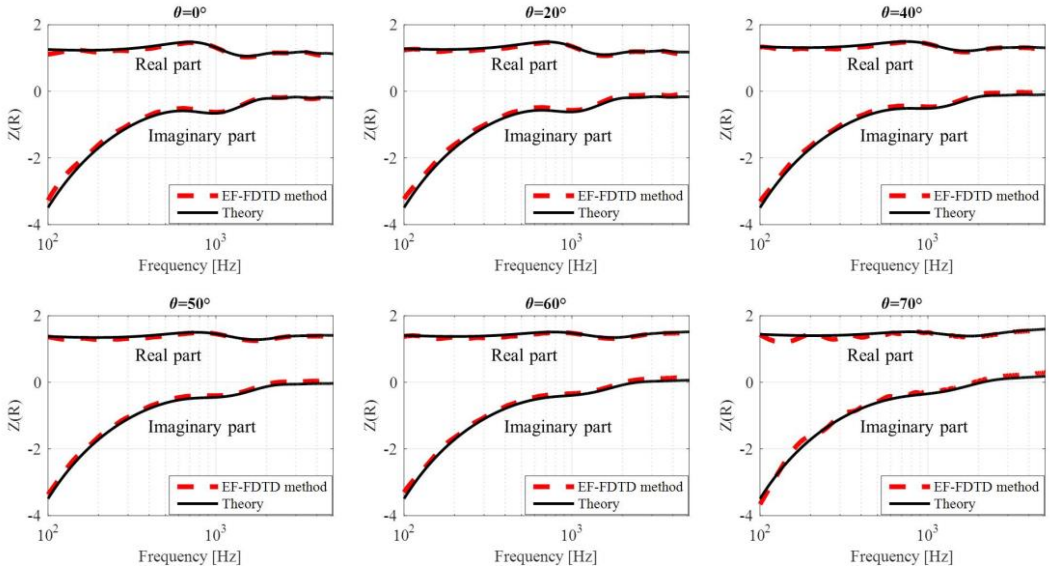

Fig.4.33 Case (4): the calculated surface impedances and theoretical values at different incident angle.

4.4 Simulation of the porous material with shape

In some places, porous materials are designed with shapes. When simulating the shaped porous material, how to treat the boundary condition is a question. As a solution, staircase approximation can be adopted. In this section, the accuracy of the staircase approximation is discussed.

As shown in Fig.4.34, the porous material (flow resistivity, 8000 $\mathrm{Nm^{-4}s}$) is backed with the rigid wall. The thickness of the porous material is 0.05m. The parameters of the designed IIR filters are given in Appendix B. R is the receiving point at the surface of the porous material. The angle θ is equal to $20°$.

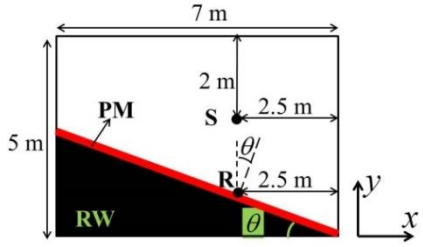

Fig.4.34 Computation domain for the FDTD analysis; PM represents the porous material; RW represents the rigid wall.

Fig.4.35 shows the treatment for the boundary condition between the air and the porous material. The particle velocities u and v are set on the boundary.

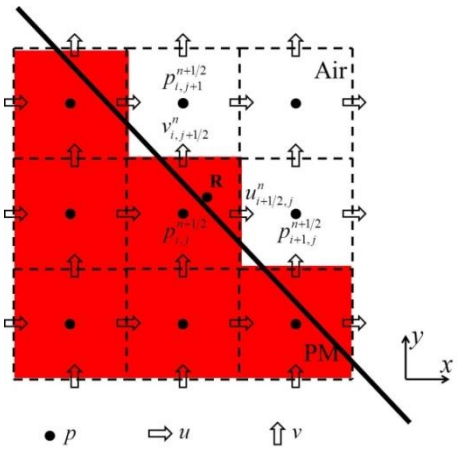

Fig.4.35 Computation domain near the boundary between the porous material and air; PM represents the porous material.

The particle velocity v is set at the boundary surface towards the y direction, calculated by:

$$v_{i,j+1/2}^{n+1} = v_{i,j+1/2}^{n} - \frac{\Delta t}{\tilde{\rho}\Delta x}\left[p_{i,j+1}^{n+1/2} - p_{i,j}^{n+1/2} \right]. \tag{4.24}$$

The particle velocity u is set at the boundary surface towards the x direction, calculated by:

$$u_{i+1/2,j}^{n+1} = u_{i+1/2,j}^{n} - \frac{\Delta t}{\tilde{\rho}\Delta x}\left[p_{i+1,j}^{n+1/2} - p_{i,j}^{n+1/2} \right], \tag{4.25}$$

where $\tilde{\rho}$ is the arithmetic averaged density of the porous material and the air.

In order to discuss the error caused by the staircase approximation, the following cases are set:

(case 1): $\Delta t = 1.02\times10^{-6}\text{s}$, $\Delta x=\Delta y = 0.001\text{m}$

(case 2): $\Delta t = 1.75\times10^{-6}\text{s}$, $\Delta x=\Delta y = 0.002\text{m}$

(case 3): $\Delta t = 3.07\times10^{-6}\text{s}$, $\Delta x=\Delta y = 0.003\text{m}$

The calculated surface impedance at the receiving point R is contrasted with the theoretical value. The theoretical value $Z(R)$ is given as:

$$Z(R) = -j\left(Z_c \frac{k}{k_3} \right)\cot(k_3 d), \tag{4.26}$$

$$k_3 = \sqrt{k^2 - (k_0 \sin\theta)^2}, \tag{4.27}$$

where d is the thickness of the porous material, equal to 0.05m here; Z_c is the characteristic impedance of the porous material; k_0 and k are the wave number in the air and in the porous material, respectively. Z_c and k are calculated by using Miki model.

For the FDTD analysis, the surface impedance $Z(R)$ is calculated by:

$$Z(R) = -\frac{P_{i,j}^{n+1/2}(\omega) + P_{i,j+1}^{n+1/2}(\omega)}{2V_{i,j+1/2}^{n}(\omega)}, \tag{4.28}$$

where $V_{i,j+1/2}^{n}(\omega)$ is the frequency response of the particle velocity $v_{i,j+1/2}^{n}$ (shown in Fig.4.35); $P_{i,j}^{n+1/2}(\omega)$ and $P_{i,j+1}^{n+1/2}(\omega)$ are the frequency responses of the sound pressure $p_{i,j}^{n+1/2}$ and $p_{i,j+1}^{n+1/2}$ (shown in Fig.4.35), respectively;

The calculated surface impedance (normalized by the characteristic impedance of the air) for case 1, case 2 and case 3 are denoted as Z_1, Z_2 and Z_3, respectively. In Fig.4.36, the theoretical value and the calculated surface impedances are plotted.

For the results of the real part and the imaginary part, Z_1 is close to Z compared to the others two results. This phenomenon is consistent with the expectation.

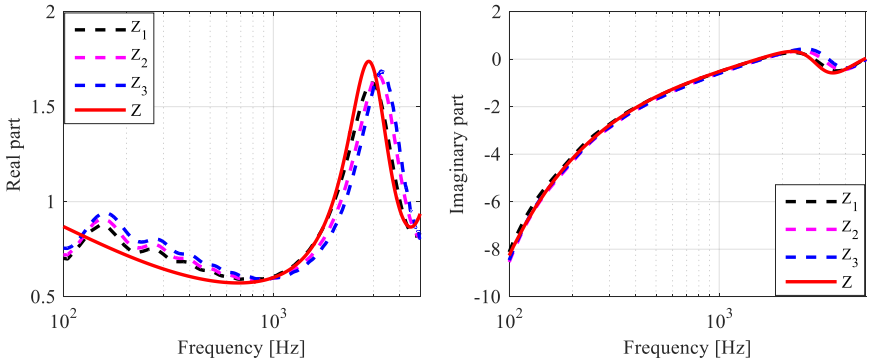

Fig.4.36 The calculated surface impedances for different simulation cases and the theoretical value.

For each case, the calculated sound absorption coefficient is given in Fig.4.37.

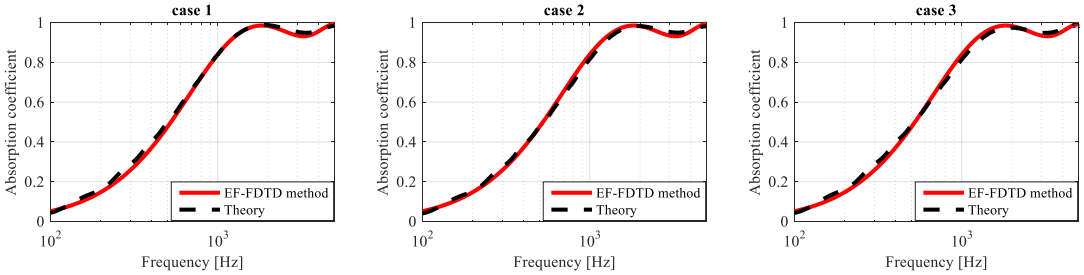

Fig.4.37 The calculated absorption coefficients for different cases and the theoretical value.

4.5 Comparison of the EF-FDTD algorithm and the Rayleigh method

In section 4.5, the 2-dimensional EF-FDTD algorithm and the exiting Rayleigh method are compared at the oblique incidence of sound. The formulas of the Rayleigh method are given in section 2.2.

In Fig.4.38, the 2-dimensional sound field is set. The four boundaries of the sound field are both the rigid wall. The porous material is set backed by the rigid wall. The thickness of the porous material is 0.05m, and the flow resistivity of the porous material is 8000 $\mathrm{Nm^{-4}s}$. S is the sound source, and the distance from the sound source to the surface of the porous material is 2m. R is set at the surface of the porous material.

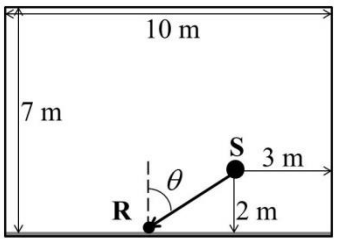

Fig.4.38 The 2 dimensional sound field for FDTD analysis.

In the numerical analysis, the discrete time interval $\Delta t = 1.75\times10^{-6}\mathrm{s}$, and the discrete space interval Δx and Δy are both 0.002m. The sound source is added by using Eq.(4.20).

The oblique incident absorption coefficient is used to examine the two methods, which is given by:

$$\alpha = 1 - \left| \frac{Z(R) - Z_0/\cos\theta}{Z(R) + Z_0/\cos\theta} \right|^2 . \tag{4.29}$$

For the calculation, $Z(R)$ is calculated by using Eq.(4.22). For the theoretical value, $Z(R)$ is calculated as follows:

$$Z(R) = -j\left(Z_c k/k_3\right)\cot\left(k_3 d_1\right), \tag{4.30}$$

$$k_3 = \sqrt{k^2 - \left(k_0 \sin\theta\right)^2}, \tag{4.31}$$

where d_1 is the thickness of the analyzed porous material. k_0 and k are wave number in air and in the porous material, respectively. Z_0 and Z_c are characteristic

impedance in the air and in the porous material. k and Z_c are calculated by using Miki model.

When using the Rayleigh model to simulate the porous material (flow resistivity: 8000 $\mathrm{Nm^{-4}s}$), the sound speed is given as $218.016 m/s$, the density is given as $2.126 \mathrm{kg/m^3}$, the flow resistivity is given as $7994.664 \mathrm{Nm^{-4}s}$, and the heat reduction coefficient is given as14.432kg/Pa.

In the figures, for different incident angles, the calculated sound pressures by using the EF-FDTD algorithm are plotted by the black lines, and the calculated averaged sound pressure by using the Rayleigh method are plotted by the red dotted lines.

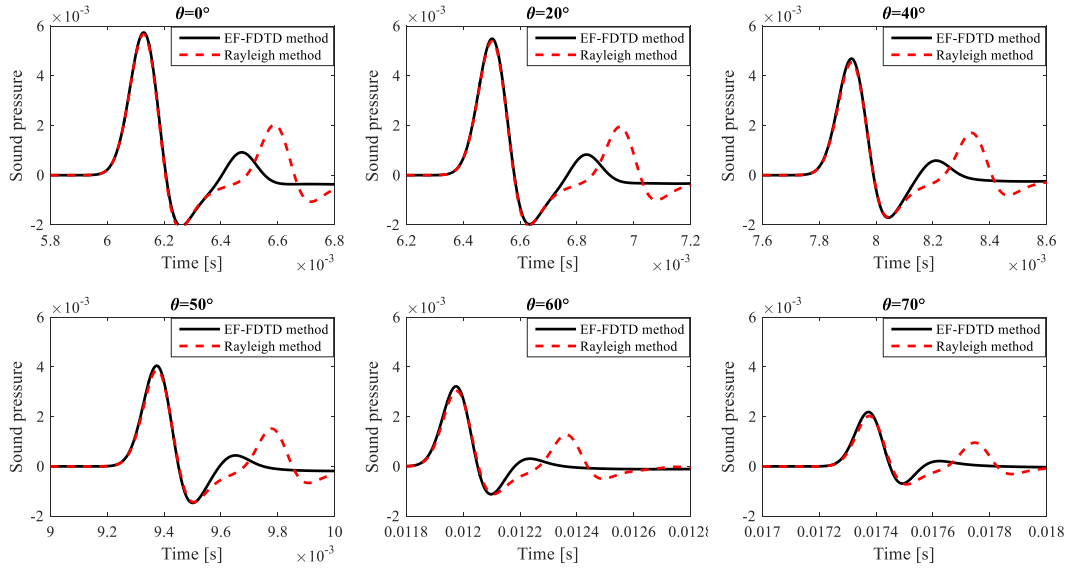

Fig.4.39 At the receiving point R, the averaged sound pressures from 0° to 70°.

For different incident angle, the calculated particle velocities by using the EF-FDTD algorithm are plotted by the black lines, as plotted in Fig.4.40. The particle velocities by using the Rayleigh method are plotted by the red dotted lines.

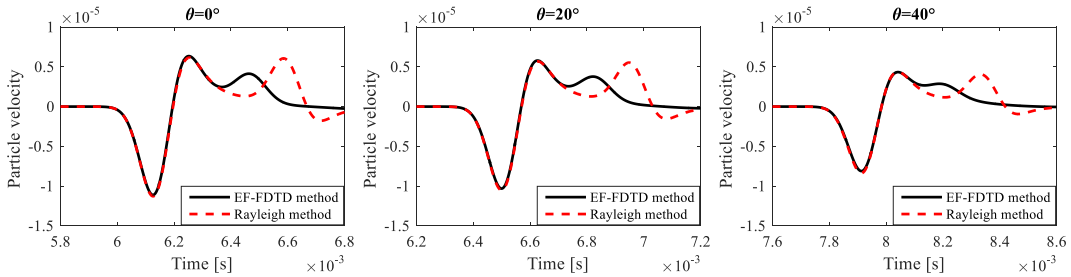

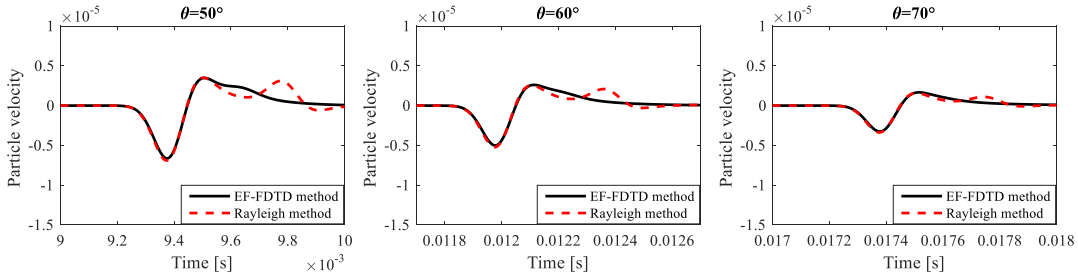

Fig.4.40 At the receiving point R, the calculated partical velocities from 0° to 70°.

When the oblique incident angle is 0°, the sound pressures calculated by the two methods almost overlap before 6.2ms, but deviate greatly from 6.2ms to 6.8ms.

When the oblique incident angle is 70°, the sound pressures calculated by the two methods deviate slightly from 17.4ms to 18ms. The particle velocity calculated by the EF-FDTD method is similar as that by the Rayleigh method.

From the results plotted in Fig.4.41, the EF-FDTD method is accurate in broad frequency range either at small incident angle or big incident angle. For the Rayleigh method, the errors between the calculated absorption coefficients and the theoretical values are very large.

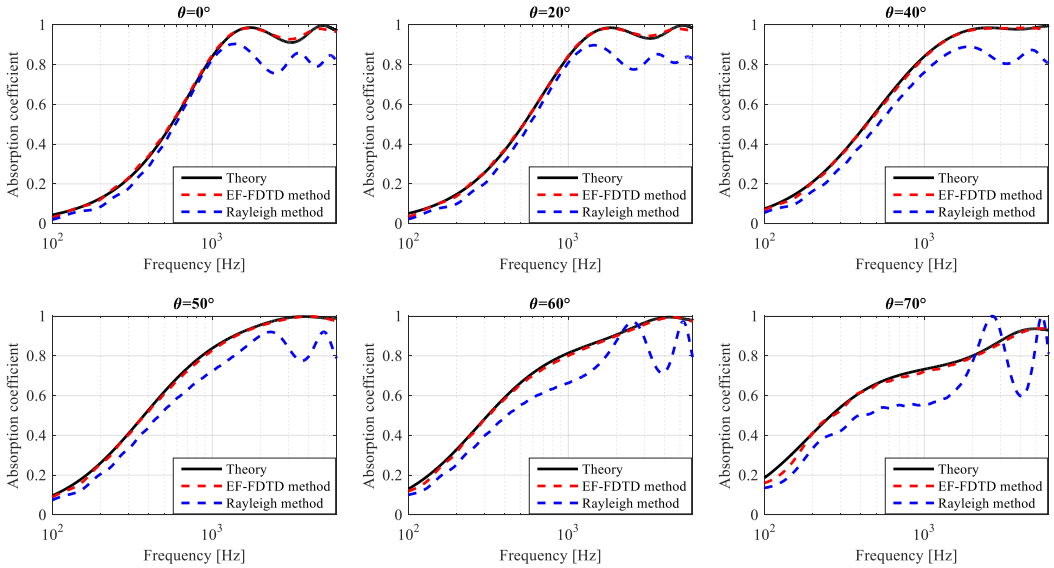

Fig.4.41 For different incident angle, the calculated absorption coeffecients and theoretical values.

4.6 Conclusion

In this chapter, the proposed EF-FDTD algorithm is validated. The 1-dimensional EF-FDTDT algorithm is validated under the normal incidence of the sound, by comparing the numerical analysis of the multi-layer porous material with the measured values. For the boundary condition analysis, the particle velocity is set on the boundary and the arithmetic averaged density is used. The 2-dimensional EF-FDTDT algorithm is validated under the oblique incident of the sound, by comparing the numerical analysis of the multi-layer porous material with the theoretic values. 4 cases of the simulation are conducted. For each case, how to treat the relative positions of the porous material and the air, how to treat the boundary condition, and how to calculate the surface impedance are discussed. The calculated surface impedances are very close to the theoretic values. The treatment for the shaped porous materials in FDTD analysis is discussed. When simulating the shaped porous material by using the staircase approximations, the discrete space interval Δx and Δy need be small.

Chapter 5 SIMULATION OF THE ACOUSTIC WEDGES

5.1 Introduction

In this chapter, 4 kinds of the porous material designed with shape (sample A, sample B, sample C and sample D) are measured and simulated. The 4 samples are introduced in section 5.2.1.The measurement system is introduced in section 5.2.2, and the properties of the used porous material are introduced in section 5.2.3. The measured and simulated results for sample A are given in section 5.3. In section 5.3.1, the equations for calculating the absorption coefficients from the measurement data are given. In section 5.3.2.2, the equations for calculating the absorption coefficients from the simulation data are given. In section 5.3.2.3, the factors which affect the result of the absorption coefficient are discussed in detail. The measured and simulated results for sample B, sample C and sample D are given in section 5.4, section 5.5 and section 5.6, respectively. The conclusions are given in section 5.7.

5.2 The preparation for the measurement

5.2.1 Background

Anechoic chamber is an important laboratory for acoustic measurements, in which the acoustical testing is conducted in nominally "free field" conditions. The "free-field" condition means that no signals are reflected from the wall. All the sound energy will be absorbed by the absorbing materials in the wall with almost none reflected energy. The "cut-off frequency" is one most important factor when design an anechoic chamber. The "cut-off frequency" is decided by the characteristic properties of the absorbing materials installed on the wall. The "cut-off frequency" is the lowest frequency at which the absorption coefficient of the absorbing materials is larger than 0.99.

In the past years, many studies[64-78] have been published to search the optimal design of the sound absorbing structures, such as geometry, dimensions, and used materials. In these studies, two important papers are published by Beranek[64-65] and Koidan[69]. In 1946, Beranek[64-65] published their significant data, in which the performances of five different kinds of structures used in an anechoic chamber are studied. The best one of these structures is made of glass fibers, shaped like a wedge. In this published paper, the "cut-off frequency" is defined. In 1972, Koidan[69] published their paper, in which a “hybrid” wedge consisting of glass wool of two densities was investigated by the experiment. The data in these papers are obtained through numerous experiments.

It takes a lot of effort to do the experiments to finally confirm the optimal parameters of the wedge. Nowadays, the properties of the acoustic wedges could be studied before it is manufactured, by using the numerical analysis methods. Easwaran[73] and Munjal used a finite element method model (FEM) to predict the reflection coefficients of a wedge. The analysis is studied in an impedance tube. The model is based on the bulk reaction assumption, which accounts for the wave

propagation in the wedge material. The theoretical predicted values agree well with those values from the experimental results. In the study by Wang[74], a boundary element method (BEM) is used in a two-dimensional analysis. The sound normally incident to a wedge settled in an impedance tube is studied. The influences on the sound pressure reflection coefficient caused by the properties of the wedge are studied, such as the total length of wedge, the thickness of base, and the thickness of air layer. In 2006, Kar[75] analyzed the performances of the acoustic wedges by using a boundary-condition-transfer function method. The method is based on the assumption of the bulk reaction for a wave propagating in the wedge material. Lee[76] used the gradient-based topology optimization setting, analyzing the two-dimensional optimal shape design method for the poroelastic acoustical foam. From the analysis, an unusual shape is obtained. Theoretically, the acoustic properties of the unusual shaped wedge are better than ordinary shaped wedge, but not verified by the experiment. In 2013, Bonfiglio[77] used simplified numerical methodologies in the FEM model, simulating the wedge in a virtual impedance tube. The low "cut-off frequency" of the anechoic chambers and the hemi-anechoic chambers is optimized. In 2016, jiang[78] used the commercial FEM software COMSOL Multiphysics, simulating the acoustical wedge structures in the normal incidence. The uniform-then-gradient, flat-wall (UGFW) structure is proposed as an alternative to the class wedge design for anechoic chambers.

It can be seen that there is not numerical method based on the FDTD analysis to design an acoustical wedge. For those people who are familiar with FDTD algorithm but not familiar with these existing methods, it will cause trouble when designing the acoustic wedges. In the previous chapters, the EF-FDTD algorithm was proposed and validated. In section 4.4, the shaped porous material can be simulated by using the staircase approximation, and the accuracy is verified. Therefore, in this chapter, based on the 2-dimensional EF-FDTD algorithm, the method for analyzing the absorption coefficients of acoustic wedges is developed[80].

5.2.2 4 samples for the measurement and simulation

Four samples simulation are illustrated in Fig.5.1, and four samples for the measurement are shown in Fig.5.2.

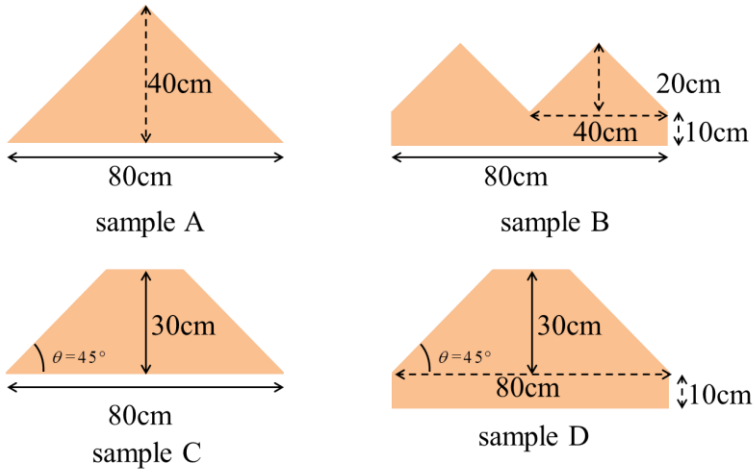

Fig.5.1 Four kinds of the designed porous material with shape.

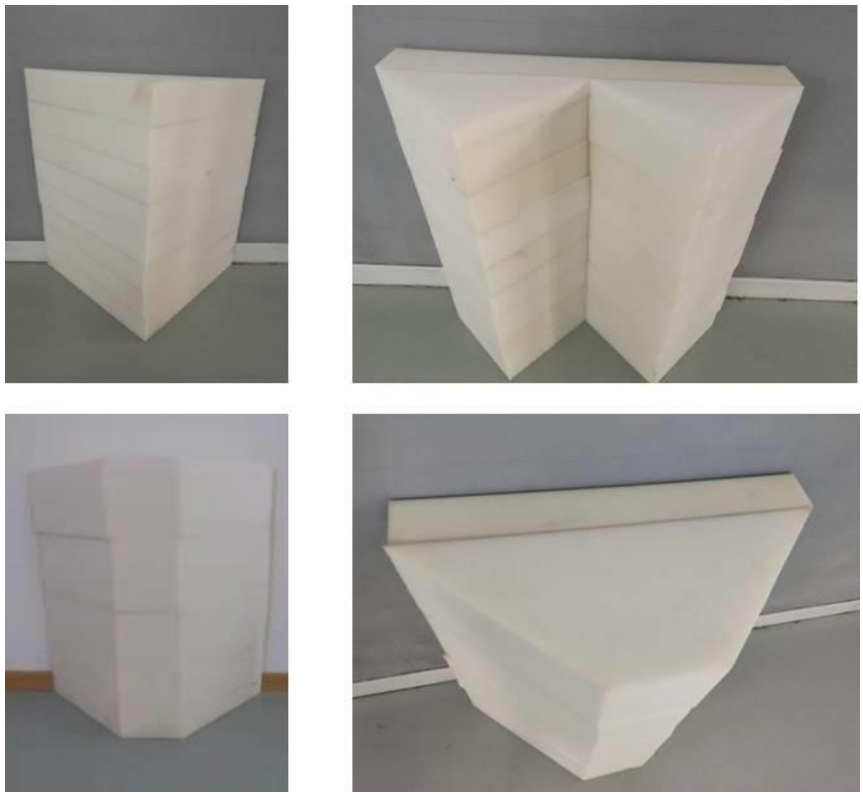

Fig.5.2 Four kinds of the customized porous materials with shape.

5.2.3 The low frequency impedance tube

The experiments are conducted in Qingdao Branch of Institute of Acoustics (Chinese Academy of Sciences), where a new low frequency impedance tube is built. As illustrated in Fig.5.3, the total length of the tube is 10.2m. The width and the height of the tube are both 0.8m. Therefore, the "cut-off frequency" f_{cut} of the impedance tube is 214Hz, calculated by:

$$f_{cut} = \frac{c_0}{2}\sqrt{\left(\frac{1}{0.8}\right)^2}. \tag{5.1}$$

The impedance tube is made of concrete, in which the standing wave ratio is larger than 40 dB. A microphone can be moved alone the middle of the tube. The measurements are based on ISO 10534-1-1996[79].

Fig.5.3 The Low frequency impedance tube.

5.2.4 Properties of the porous material

The high density sponge is used to manufacture the shaped porous materials for the measurement. The acoustical properties of the high density sponge are measured in the B&K impedance tube (Type: 4206). First, the testing samples are made circularly with the diameter of 100mm. The characteristic impedance $Z_c(\omega)$ and the wave number $k(\omega)$ are measured by using the 2-cavity method. As shown in Fig.5.4, the measured characteristic impedance of the high density sponge (normalized by the characteristic impedance of the air) is plotted by the left figure; the measured wave number of the high density sponge (normalized by the wave number of the air) is plotted by the right figure.

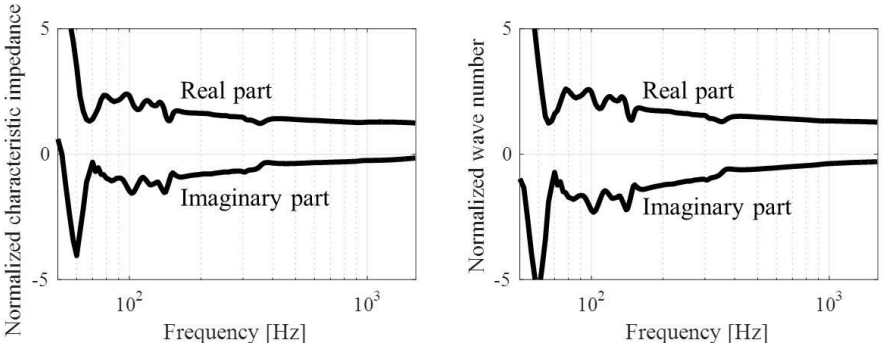

Fig.5.4 The measured properties of the high density sponge. Left: the normalized characteristic impedance; Right: the normalized wave number.

By using Eq.(4.6)-Eq.(4.7), the effective bulk modulus and the effective density are calculated by using the characteristic impedance $Z_c(\omega)$ and the wave number $k(\omega)$. Based on the calculated values, the IIR filters are designed from 50Hz to 500Hz. As shown in Fig.5.5, the effective bulk modulus of the high density sponge is plotted by the red lines in the left figure, and the designed IIR filter is plotted by the black dotted lines in the left figure. The effective density of the high density sponge is plotted by the red lines in the right figure, and the designed IIR filter is plotted by the black dotted lines in the right figure.

The IIR filters are designed only containing real poles, and the parameters are given in table 5-1 and table 5-2.

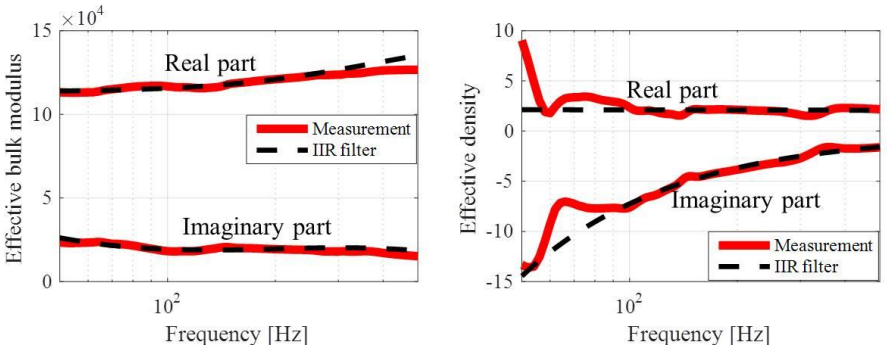

Fig.5.5 The properties of the high density sponge. Left: the effective bulk modulus and the designed IIR filter; Right: the effective density and the designed IIR filter.

Table 5-1 For the effective bulk modulus of the high density sponge, the parameters in the designed IIR filter.

k_0	q	r
147447.4566	-2362.9969	-80477144.5906
	-1.1143	-6822151.1199

Table 5-2 For the effective density of the high density sponge, the parameters in the designed IIR filter.

k_0'	q'	r'
1.4914	-11505.6722	6977.6840
	-0.6851	4533.6737

5.3 The measurement and the FDTD analysis for sample A

5.3.1 The measurement results for sample A

For sample A, the width is 0.8m and the height is 0.4m. The manufactured porous materials used for measurement are shown in Fig.5.6. The making of the samples are commissioned to a factory. Firstly 8 pieces of the samples are made. Due to the precision limitation of the fabrication process, in the measurement, there is air space (about 3cm) between the surface of the porous materials and the top rigid wall. Therefore, another sample with the thickness of 3cm is made, as shown in Fig.5.7.

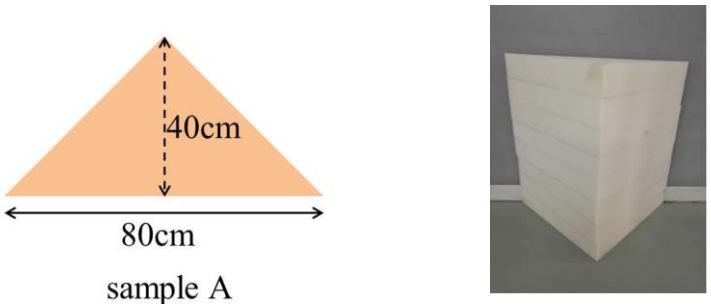

Fig.5.6 The customized porous materials for sample A.

Fig.5.7 shows the measurement photo on the site. At one end of the tube, the costumed porous materials are stacked without using glues. There is no air space setting between the porous materials and the backed rigid wall.

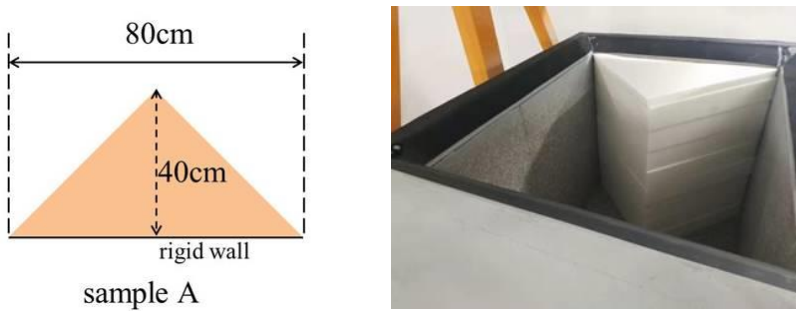

Fig.5.7 The measurement photo on the site for sample A.

In the measurement, the loudspeaker emits continues single frequency sinusoidal wave. As shown in Fig.5.8, a movable microphone is moving from position A to position B, recording the values of the sound pressure level in the impedance tube.

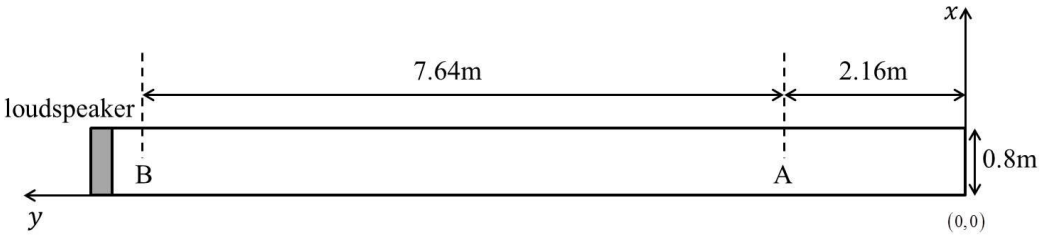

Fig.5.8 The microphone is moving from postion A to position B.

From 50Hz to 200Hz, the recorded values of the sound pressure level are plotted, as shown in Fig.5.9.

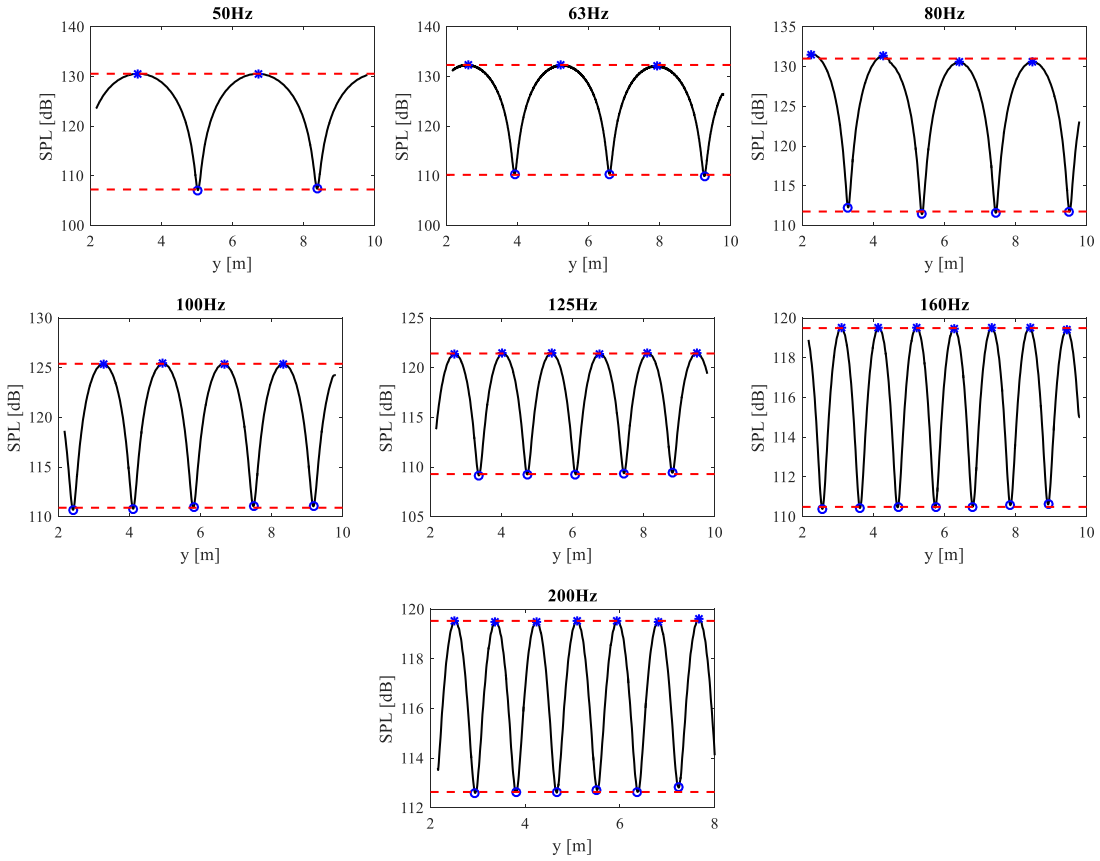

Fig.5.9 The measured sound pressure level for sample A.

In Fig.5.9, blue * represent the searched maximum values of the sound pressure levels. Then these maximum values are averaged, which is the value of $SPL_{\max}$, plotted by the upper dotted red line. Blue o represent the searched minimum sound pressure levels. Then these minimum values are averaged, which is the value of $SPL_{\min}$, plotted by the lower dotted red line.

For 200Hz, when search the maximum values and the minimum values, only the data between 20s and 100s is used.

The absorption coefficient can be calculated by:

$$\alpha = 1 - \left| \frac{G-1}{G+1} \right|^2 , \tag{5.2}$$

where G is the standing wave ratio, calculated by:

$$G = \frac{10^{SPL_{\max}/20}}{10^{SPL_{\min}/20}} . \tag{5.3}$$

For each frequency, the values of $SPL_{\max}$, the values of $SPL_{\min}$ and the absorption coefficients α_{meas} are given in table 5-3.

In chapter 5, 3 decimal places are used to analyze the value of the absorption coefficients, in order to get the precision errors between the measured absorption coefficients and the calculated values.

Table 5-3 The measured absorption coefficient for sample A

	50Hz	63 Hz	80 Hz	100 Hz	125 Hz	160 Hz	200 Hz
$SPL_{\max}$	130.55	132.33	130.83	125.40	121.43	119.49	119.53
$SPL_{\min}$	107.26	110.20	111.76	110.90	109.29	110.49	112.64
α_{meas}	0.240	0.269	0.361	0.534	0.636	0.773	0.858

In Fig.5.10, the measured absorption coefficients for sample A from 50Hz to 200Hz are plotted.

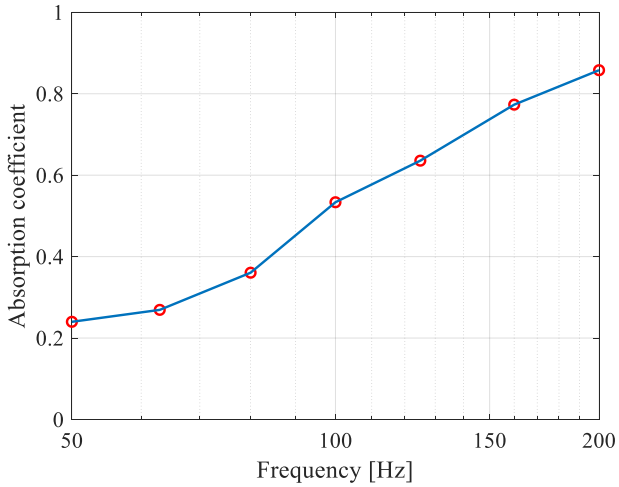

Fig.5.10 For sample A, the measured absorption coefficients from 50Hz to 200Hz.

5.3.2 The FDTD analysis for sample A

5.3.2.1 FDTD setting in 2-dimensioanl sound field

For the FDTD analysis, two-dimensional sound field setting is illustrated in Fig.5.11. Four boundaries in the computation domain are both rigid walls. Corresponding to the measurement, there is no air space between the porous material and the backed rigid wall. The length of the computation domain in y direction is 10m, and the width of the computation domain is 0.8m. The discrete time interval is 1.75×10^{-6} s. In order to obtain precision numerical results, the discrete space intervals Δx and Δy are both 0.002m. Therefore, in x direction, the number of the discrete grids Ax is 400. In the y direction, the number of the discrete grids Ay is 5000. For this number of the grid, the amount of calculation is acceptable. Two positions are marked in the figure. In the y direction, position a is at y=0.4m, and position b is at y=4.4m.

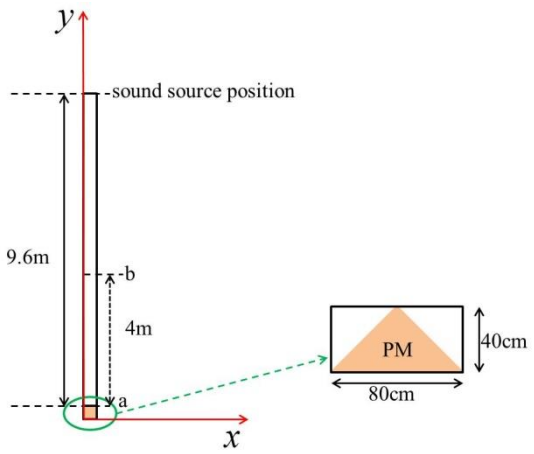

Fig.5.11 Two-dimensional sound field for the FDTD analysis.

In the calculation, the sound pressures at these receiving points $(Ax/2, y_a)$, $(Ax/2, y_a+1)\ldots$ $(Ax/2, y_b)$ are saved. y_a is corresponding to the position a (y=0.3m), and y_b is corresponding to the position b (y=4.3m).

5.3.2.2 Discuss the input method of the plane wave sound source

The sound source is input at the top position in the y direction, which is given as the plane wave incidence. As illustrated in Fig.5.12, the input method of the plane wave sound source can be given as follows:

$$p_{i,j}^{n+1/2} = \sin\left[2\times\pi\times f_c\times(n\Delta t)\right], \tag{5.4}$$

$$v_{i,j+1/2}^{n} = \sin\left[2\pi\times f_c\times(n\Delta t)\right] \tag{5.5}$$

Here, n is the time step, the value of i is from 1 to Ax, the value of j is equal to Ay. f_c is the frequency of the sound source, which is chosen from the following values: 50, 63, 80, 100, 125, 160, and 200.

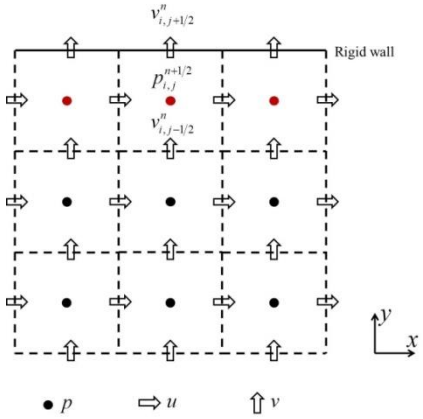

Fig.5.12 The sound field at the top position of the compution domain.

As an example, the calculated sound pressures by using Eq.(5.4) and Eq.(5.5) at the receiving point (0.4m, 4.4m) are shown in Fig.5.13.

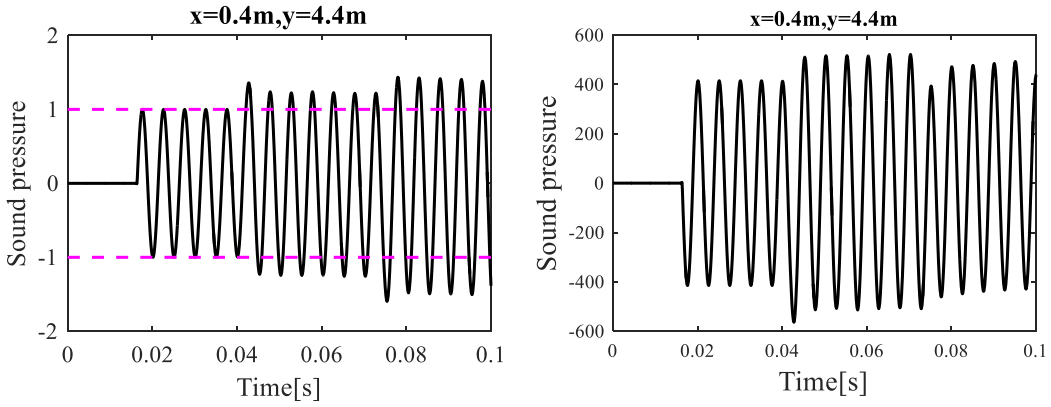

Fig.5.13 The calculated sound pressure at the receiving point (0.4m, 4.4m).Left: by using equation (5.5); right: by using equation (5.6).

In the calculation, the continuous sine wave is emitted from the plane wave sound source. The plane wave travels along the y direction. When the first plane wave arrives at the top position of the porous material, the first reflection occurs. Then the standing wave sound field begins to be established. When the reflected sound wave arrives at the top position in the y direction, the standing wave field is superposed by the incident sound wave from the sound source. The standing wave sound field is destroyed no matter using Eq.(5.4) or Eq.(5.5).

In Fig.5.13, the amplitudes of the calculated sound pressures are different. In this thesis, the input method of the plane wave sound source is adopted by using Eq.(5.4).

5.3.2.3 The method for calculating the absorption coefficient

In this section, how to calculate the sound absorption coefficient is discussed. As an example, when the frequency of the sound source f_c is 200Hz, the calculated sound pressures ($0 \le x \le 0.8m, 0 \le y \le 1.5\text{m}$) are shown in Fig.5.14.

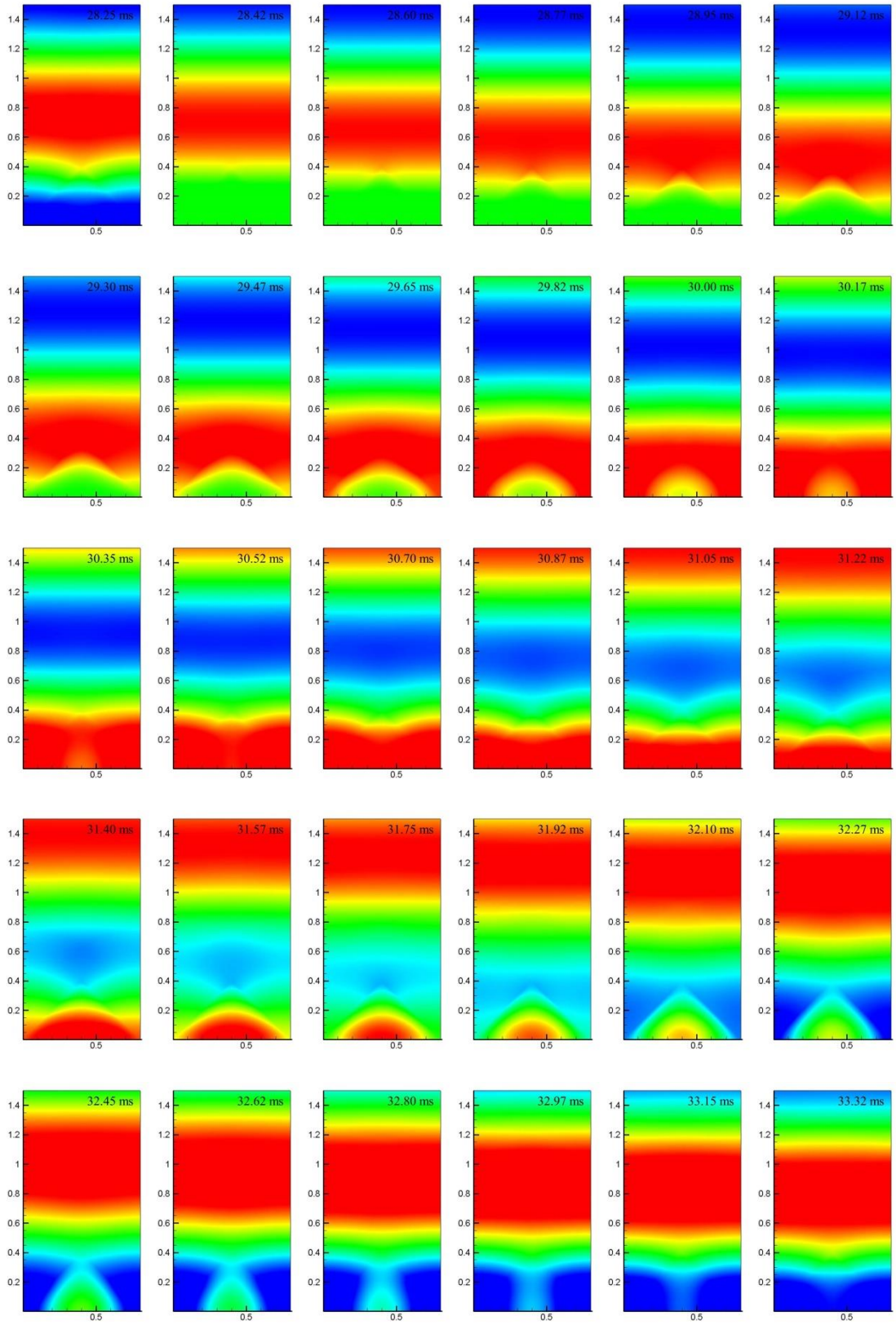
28.25 ms
28.42 ms
28.60 ms
28.77 ms
28.95 ms
29.12 ms
29.30 ms
29.47 ms
29.65 ms
29.82 ms
30.00 ms
30.17 ms
30.35 ms
30.52 ms
30.70 ms
30.87 ms
31.05 ms
31.22 ms
31.40 ms
31.57 ms
31.75 ms
31.92 ms
32.10 ms
32.27 ms
32.45 ms
32.62 ms
32.80 ms
32.97 ms
33.15 ms
33.32 ms

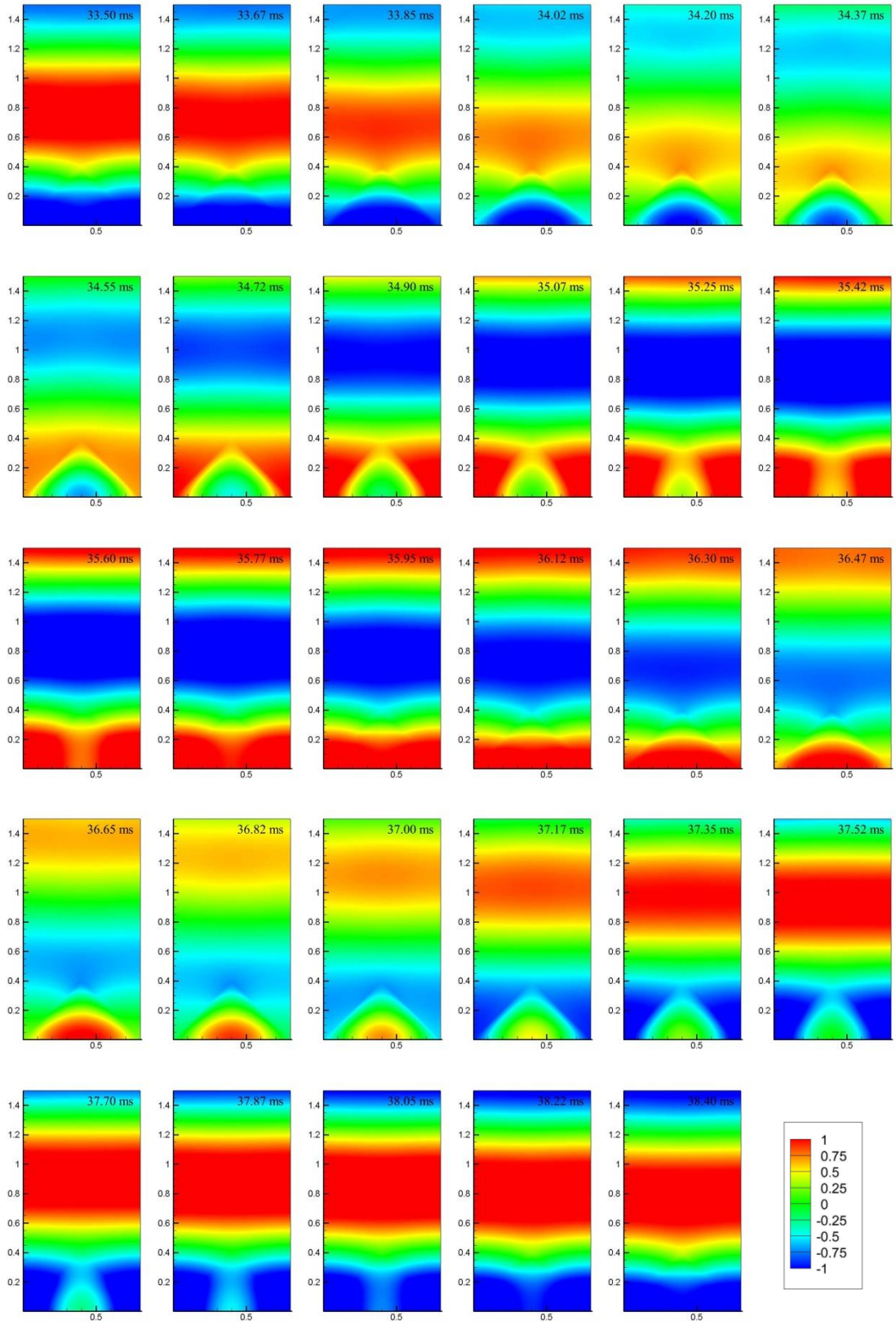

Fig.5.14 At different time step, the calculated sound pressures ($0 \le x \le 0.8m, 0 \le y \le 1.5\text{m}$).

The calculated sound pressures at these positions are plotted in Fig.5.15.

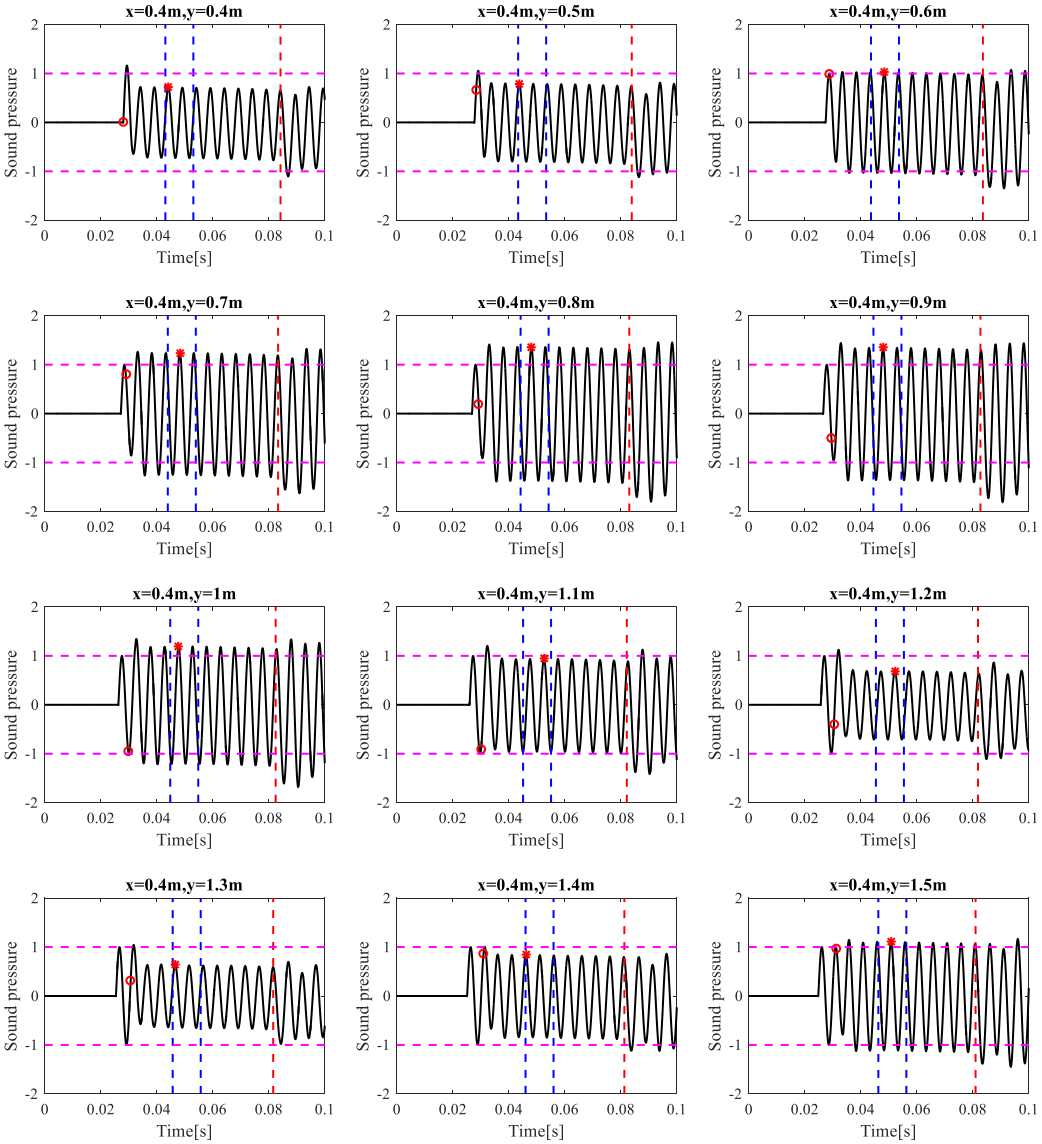

Fig.5.15 The received sound pressure at different receiving points.

When the plane wave firstly arrives at the top position of the porous material, the first reflected sound wave occurs. At different receiving points, the time point for arising the first reflected wave T_r is plotted by red o in Fig.5.15.

As shown in Fig.5.16, for a receiving point located at the position (x, y), T_r can be calculated by:

$$T_r = \frac{L+h}{c_0}, \tag{5.6}$$

where h is the distance in the y direction, between the top position of the porous material and the receiving point position, which satisfy $h = y - 0.4$ here. L is the

distance in the y direction, between the top position of the porous material and the sound source position, which satisfy $L = 9.4$ here. c_0 represents the sound speed in the air.

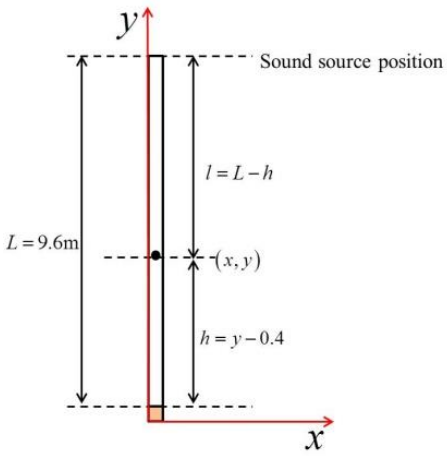

Fig.5.16 A receiving point located at the direction (x,y).

Once the time point T_r is searched, the time range for the standing wave exiting in the sound field can be searched. The standing wave field is not established immediately after the time point T_r. It needs time to establish the stable standing wave field. In Eq.(5.7)-Eq.(5.8), T_s and T_e are set to find the established standing wave field, which is calculated by:

$$T_s = T_r + \frac{M}{f_c}, \tag{5.7}$$

$$T_e = T_s + \frac{N}{f_c}. \tag{5.8}$$

In the Fig.5.15, T_s is plotted by the left dotted blue line, and T_e is plotted by the right dotted blue line. When calculate T_s and T_e, M and N are adopted as 3 and 2, respectively.

In the figure, the sound field is no longer the standing wave after time point $T_{\max}$. The reason is that the sine wave is continually emitted from the sound source. After time point $T_{\max}$, the standing wave field is superposed by the incident sound wave from the sound source. In Fig.5.15, $T_{\max}$ is plotted by the dotted red line, calculated by using Eq.(5.9):

$$T_{\max} = \frac{2L + l}{c_0}. \tag{5.9}$$

Then, the amplitudes of the standing wave at each receiving points can be searched. The amplitude of the standing wave is the maximum value of the sound pressure between time point T_s and time point T_e, which is plotted by the red * in the Fig.5.15.

By using the same method, the amplitude of the standing wave at each position can be obtained. In Fig.5.17, the searched amplitudes ($x = 0.4\text{m}, 0.4\text{m} \le y \le 4.4\text{m}$) are plotted when f_c is 200Hz.

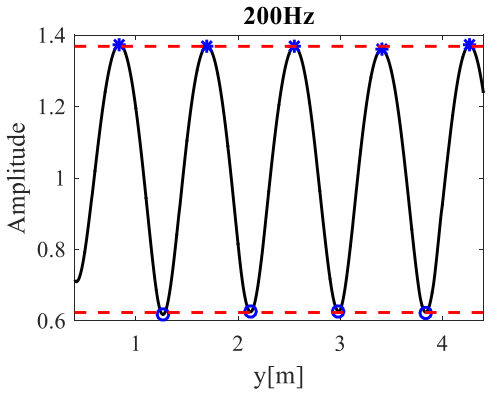

Fig.5.17 For 200Hz, the searched amplitudes of the standing wave.

When calculating the sound absorption coefficients, the maximum values of the amplitude of the standing wave and the minimum values of the amplitude of the standing wave need to be searched. The first minimum value occurs at y=0.42m, but is not used in the calculation. This position is near the top position of the porous material, that is y=0.4m. As shown in Fig.5.10, the sound field at that position is very complicated, which is caused by the shape of the porous materials. The air space exits between the porous material and the rigid side wall, and multiple reflections occur at those places near the top position of the porous materials. This minimum value is affected by the complicated sound field.

In Fig.5.17, blue * represents the searched maximum values. Then these maximum values are averaged, which is the value of $p_{\max}$, plotted by the upper

dotted red line. Blue o represents the searched minimum values. Then these minimum values are averaged, which is the value of $p_{\min}$, plotted by the lower dotted red line.

The absorption coefficient can be calculated by:

$$\alpha = 1 - \left| \frac{G-1}{G+1} \right|^2, \tag{5.10}$$

where G is the standing wave ratio, calculated by:

$$G = \frac{p_{\max}}{p_{\min}}. \tag{5.11}$$

For 200Hz, the value of $p_{\max}$ is 1.3690, and the value of $p_{\min}$ is 0.6237. Input $p_{\max}$ and $p_{\min}$ in Eq.(5.11), the standing wave ration G can be obtained, and the absorption coefficient can be calculated, which is 0.860. The measured absorption coefficient is 0.858, and the calculated value is 0.860. The absolute error is only 0.002.

5.3.2.4 Discussion of the factors affecting the result of the absorption coefficient

The factors affecting the calculation of the absorption coefficient are T_r, T_s and T_e.

T_r is the time point for receiving the first reflected sound wave coming from the surface of the porous material (y=0.4m), which is calculated by Eq.(5.12). For a fixed receiving point at position (x,y), L and h are not changed. Then T_r is not changed, which do not affect the calculation of the absorption coefficient.

$$T_r = \frac{L+h}{c_0}. \tag{5.12}$$

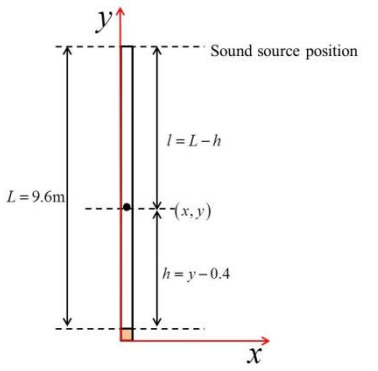

Fig.5.18 A receiving point located at the direction (x,y).

As discussed in section 5.3.2.2, T_s and T_e are time points to search the standing wave field, which satisfy the following equations:

$$T_s = T_r + \frac{M}{f_c}, \tag{5.13}$$

$$T_e = T_s + \frac{N}{f_c}, \tag{5.14}$$

$$T_e \le \frac{2L+l}{c_0}. \tag{5.15}$$

Rearranging these equations, the following equation is obtained:

$$\frac{M+N}{f_c} \le \frac{2l}{c_0}. \tag{5.16}$$

In the FDTD numerical simulation, the positions for these receiving points are from y=0.4m to y=4.4m. Then, the relationship between the value of *M* and the value of *N* is given:

$$M + N \le MN_{\max} = \frac{11.2 \cdot f_c}{c_0}. \tag{5.17}$$

From 50Hz to 200Hz, the values of $MN_{\max}$ are calculated, and given in table 5-4.

Table 5-4 From 50Hz to 200Hz, the values of $MN_{\max}$

	50Hz	63Hz	80Hz	100Hz	125Hz	160Hz	200Hz
$MN_{\max}$	1.63	2.06	2.61	3.27	4.09	5.23	6.54

In order that the maximum of the intercepted sound pressure can be found, the data at least one cycle should be ensured. Therefore, $N \ge 1$.

As shown in Fig.5.14 and Fig.5.15, there needs some time to establish a stable standing wave field. Too early or too late intercepting the received sound pressure, the searched maximum values may not be the true amplitudes of the standing wave. Therefore, how to choose the start time point T_s is very important.

Next, how the start time point T_s affects the result of the absorption coefficient is discussed. The following three cases are discussed.

(Case 1): *M*=0, *N*=1;

(Case 2): *M*=0.5, *N*=1;

(Case 3): *M*=1, *N*=1;

(1) $f_c = 200\,\text{Hz}$

As shown in Fig.5.19, the searched amplitudes of the standing wave at positions ($x = 0.4\text{m}, 0.4\text{m} \le y \le 4.4\text{m}$) for different cases are plotted, when the frequency of the sound source f_c is 200 Hz.

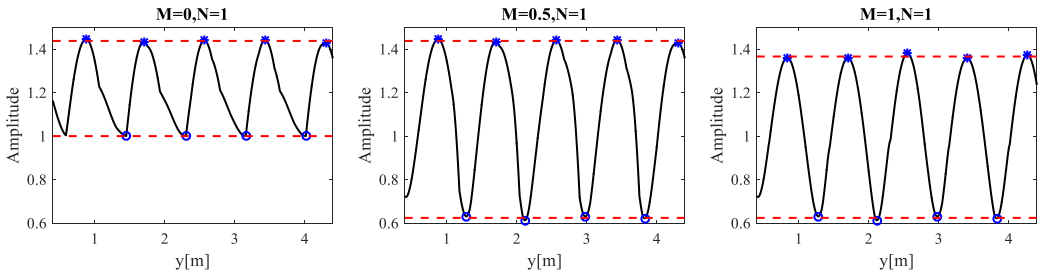

Fig.5.19 For 200Hz, the searched amplitudes of the standing wave.

For each case, the values of $p_{\max}$, the values of $p_{\min}$, the calculated absorption coefficients α_{FDTD}, and the absolute errors E_r ($|\alpha_{FDTD}-\alpha_{meas}|$) are given in table 5-5. For 200Hz, the absorption coefficient α_{meas} by the measurement is 0.858.

Table 5-5 The calculated values for 200Hz

	$M=0, N=1$	$M=0.5, N=1$	$M=1, N=1$
$p_{\max}$	1.4385	1.4385	1.3668
$p_{\min}$	1.0008	0.6249	0.6249
α_{FDTD}	0.968	0.845	0.861
E_r	0.110	0.013	0.003

(2) $f_c = 160$ Hz

As shown in Fig.5.20, the searched amplitudes of the standing wave at these positions ($x=0.4\text{m}, 0.4\text{m} \le y \le 4.4\text{m}$) for different cases are plotted, when the frequency of the sound source f_c is 160 Hz.

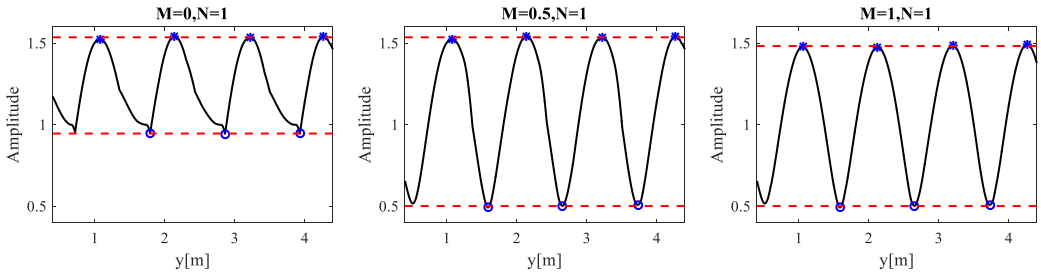

Fig.5.20 For 160Hz, the searched amplitudes of the standing wave.

For each case, the calculated values of $p_{\max}$, the calculated values of $p_{\min}$, the calculated absorption coefficients α_{FDTD}, and the absolute errors E_r ($|\alpha_{FDTD}-\alpha_{meas}|$) are given in table 5-6. For 160Hz, the measured absorption coefficient α_{meas} is 0.773.

Table 5-6 The calculated values for 160Hz

	$M=0, N=1$	$M=0.5, N=1$	$M=1, N=1$
$p_{\max}$	1.5365	1.5365	1.4832
$p_{\min}$	0.9465	0.5021	0.5021
α_{FDTD}	0.944	0.743	0.756
E_r	0.171	0.030	0.017

(3) $f_c = 125\,\text{Hz}$

As shown in Fig.5.21, the searched amplitudes of the standing wave at these positions ($x = 0.4\text{m}, 0.4\text{m} \le y \le 4.4\text{m}$) for different cases are plotted, when the frequency of the sound source f_c is 125 Hz.

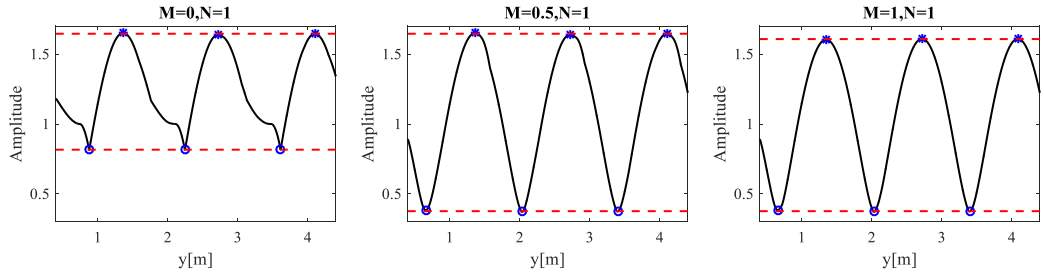

Fig.5.21 For 125Hz, the searched amplitudes of the standing wave.

For each case, the calculated values of $p_{\max}$, the calculated values of $p_{\min}$, the calculated absorption coefficients α_{FDTD}, and the absolute errors E_r ($|\alpha_{FDTD} - \alpha_{meas}|$) are given in table 5-7. For 125Hz, the measured absorption coefficients α_{meas} is 0.636.

Table 5-7 The calculated values for 125Hz

	$M=0, N=1$	$M=0.5, N=1$	$M=1, N=1$
$p_{\max}$	1.6456	1.6456	1.6076
$p_{\min}$	0.8164	0.3766	0.3766
α_{FDTD}	0.887	0.606	0.615
E_r	0.251	0.030	0.021

(4) $f_c = 100$ Hz

As shown in Fig.5.22, the searched amplitudes of the standing wave at these positions ($x = 0.4\text{m}, 0.4\text{m} \le y \le 4.4\text{m}$) for different cases are plotted, when the frequency of the sound source f_c is 100 Hz.

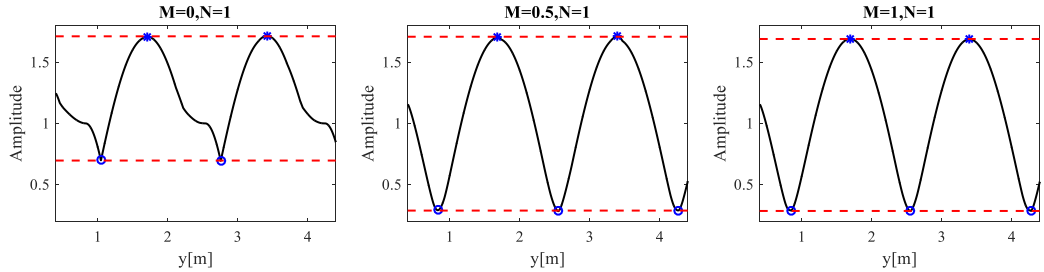

Fig.5.22 For 100Hz, the searched amplitudes of the standing wave.

For each case, the calculated values of $p_{\max}$, the calculated values of $p_{\min}$, the calculated absorption coefficients α_{FDTD}, and the absolute errors E_r ($\left|\alpha_{FDTD} - \alpha_{meas}\right|$) are given in table 5-8. For 100 Hz, the measured absorption coefficient α_{meas} is 0.534.

Table 5-8 The calculated values for 100Hz

	$M=0, N=1$	$M=0.5, N=1$	$M=1, N=1$
$p_{\max}$	1.7120	1.7085	1.6900
$p_{\min}$	0.6963	0.2873	0.2843
α_{FDTD}	0.822	0.493	0.493
E_r	0.288	0.041	0.041

(5) $f_c = 80$ Hz

As shown in Fig.5.23, the searched amplitudes of the standing wave at these positions ($x = 0.4\text{m}, 0.4\text{m} \le y \le 4.4\text{m}$) for different cases are plotted, when the frequency of the sound source f_c is 80 Hz.

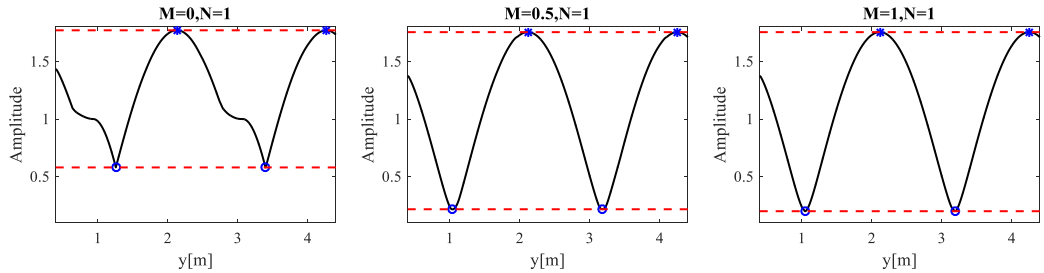

Fig.5.23 For 80Hz, the searched amplitude of the standing wave at different positions.

For each case, the calculated values of $p_{\max}$, the calculated values of $p_{\min}$, the calculated absorption coefficients α_{FDTD}, and the absolute errors E_r ($\left|\alpha_{FDTD}-\alpha_{meas}\right|$) are given in table 5-9. For 80Hz, the measured absorption coefficient α_{meas} is 0.361.

Table 5-9 The calculated values for 80Hz

	$M=0, N=1$	$M=0.5, N=1$	$M=1, N=1$
$p_{\max}$	1.7707	1.7548	1.7548
$p_{\min}$	0.5798	0.2165	0.1995
α_{FDTD}	0.743	0.391	0.367
E_r	0.382	0.030	0.006

(6) $f_c = 63\,\text{Hz}$

As shown in Fig.5.24, the searched amplitudes of the standing wave at these positions ($x=0.4\text{m}, 0.4\text{m} \le y \le 4.4\text{m}$) for different cases are plotted, when the frequency of the sound source f_c is 63 Hz.

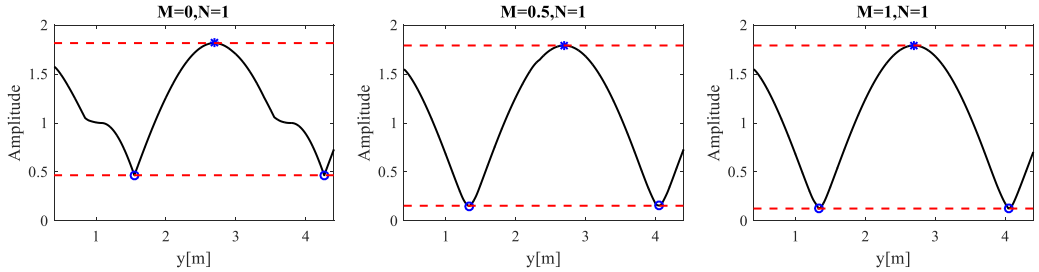

Fig.5.24 For 63Hz, the searched amplitude of the standing wave.

For each case, the calculated values of $p_{\max}$, the calculated values of $p_{\min}$, the calculated absorption coefficients α_{FDTD}, and the absolute errors E_r ($\left|\alpha_{FDTD}-\alpha_{meas}\right|$) are given in table 5-10. For 63Hz, the measured absorption coefficient α_{meas} is 0.269.

Table 5-10 The calculated values for 63Hz

	$M=0, N=1$	$M=0.5, N=1$	$M=1, N=1$
$p_{\max}$	1.8166	1.7921	1.7921
$p_{\min}$	0.4662	0.1544	0.1259
α_{FDTD}	0.650	0.292	0.245
E_r	0.381	0.023	0.024

(6) $f_c = 50\,\text{Hz}$

As shown in Fig.5.25, the searched amplitudes of the standing wave at these positions ($x = 0.4\text{m}, 0.4\text{m} \le y \le 4.4\text{m}$) for different cases are plotted, when the frequency of the sound source f_c is 50 Hz.

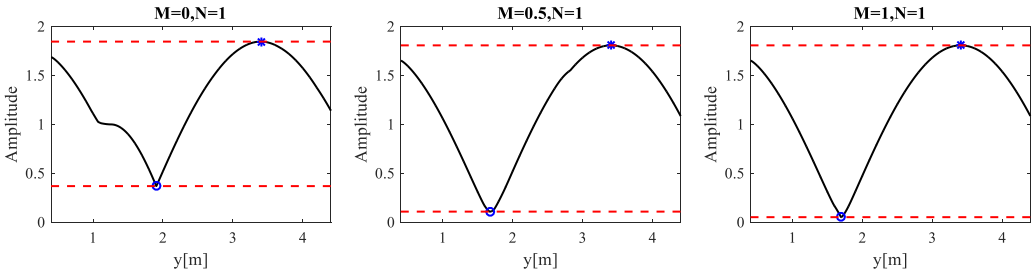

Fig.5.25 For 50Hz, the searched amplitude of the standing wave.

For each case, the calculated values of $p_{\max}$, the calculated values of $p_{\min}$, the calculated absorption coefficients α_{FDTD}, and the absolute errors E_r ($\left|\alpha_{FDTD} - \alpha_{meas}\right|$) are given in table 5-11. For 50Hz, the measured absorption coefficient α_{meas} is 0.240.

Table 5-11 The calculated values for 50Hz

	$M=0, N=1$	$M=0.5, N=1$	$M=1, N=1$
$p_{\max}$	1.8460	1.8076	1.8076
$p_{\min}$	0.3695	0.1088	0.0521
α_{FDTD}	0.556	0.214	0.109
E_r	0.316	0.026	0.131

(7) Conclusion

For different cases, the absolute errors between the measured absorption coefficients and the values by the numerical analysis from 50Hz to 200Hz are given in table 5-12.

Table 5-12 For different cases, the absoute errors between the measured absorption coefficients and the values by the numerical analysis.

	$M=0, N=1$	$M=0.5, N=1$	$M=1, N=1$
50Hz	0.316	0.026	0.131
63Hz	0.381	0.023	0.024
80Hz	0.382	0.030	0.006
100Hz	0.288	0.041	0.041
125Hz	0.251	0.030	0.021
160Hz	0.171	0.030	0.017
200Hz	0.110	0.013	0.003

For 50Hz and 63Hz, when $M=0.5$ and $N=1$, the error is the smallest than the other two cases. When $M=0$, it is earlier to choose the start time point T_s. When $M=1$, it is later to choose the start time point T_s. The reason for this phenomenon is that the wavelengths for 50Hz and 63Hz are 6.8m and 5.4m, respectively. Compared with their wavelengths, the total computation domain in the y direction is not long enough.

For 80Hz-200Hz, when $M=1$ and $N=1$, the error is the smallest than the other two cases. For all frequencies, when $M=0.5$, the errors are acceptable. It means that for a receiving point, once T_r is known, the best value for T_s is:

$$T_s \geq T_r + \frac{0.5}{f_c}. \tag{5.18}$$

From the above analysis, the following 3 equations are concluded to decide the best values of M and N:

$$M + N \leq MN_{\max}, \tag{5.19}$$

$$M \geq 0.5, \tag{5.20}$$

$$N \geq 1. \tag{5.21}$$

In the simulation for sample A, the value of $MN_{\max}$ can be found in table 5-13.

Table 5-13 From 50Hz to 200Hz, the values of $MN_{\max}$

	50Hz	63Hz	80Hz	100Hz	125Hz	160Hz	200Hz
MN_{max}	1.63	2.06	2.61	3.27	4.09	5.23	6.54

5.3.3 Contrast the measurement results and the FDTD analysis results

In Fig.5.26, the amplitudes of the standing wave ($x = 0.4\text{m}, 0.4\text{m} \le y \le 4.4\text{m}$) from 50Hz to 200Hz are plotted. The values of M and N in Eqs.(5.7)-(5.8) are given in table 5-14.

Table 5-14 From 50Hz to 200Hz, the values of M and N

	50Hz	63 Hz	80 Hz	100 Hz	125 Hz	160 Hz	200 Hz
M	0.6	0.8	1.5	1.5	2	2	3
N	1	1	1	1	1	2	2

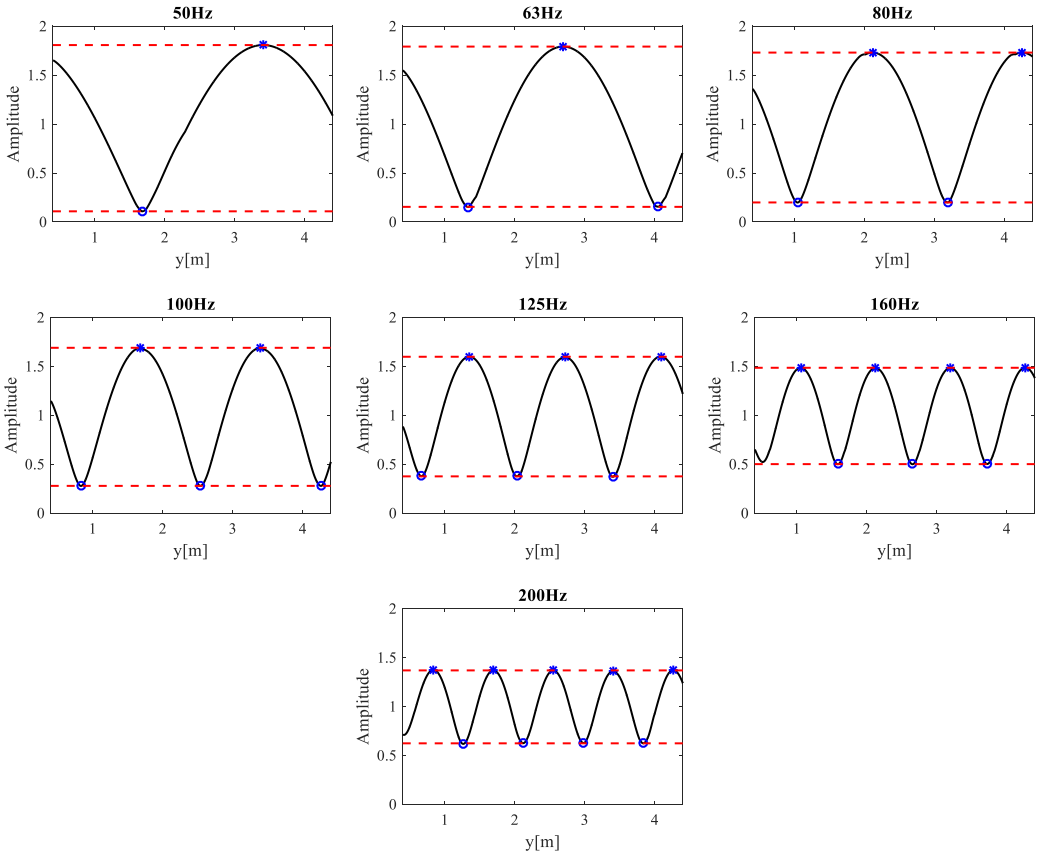

Fig.5.26 For each frequency, the searched amplitude of the standing wave.

When calculate the absorption coefficient, the maximum value and the minimum value of the amplitudes of the standing wave are used. In Fig.5.25, blue * represents the searched maximum values. Then these maximum values are averaged, which is the value of $p_{\max}$, plotted by the upper dotted red line. Blue o represents the searched minimum values. Then these minimum values are averaged, which is the value of

$p_{\min}$, plotted by the lower dotted red line. The values of $p_{\max}$ and the values of $p_{\min}$ are presented in table 5-15.

Table 5-15 From 50Hz to 200Hz, the calculated values of $p_{\max}$ and $p_{\min}$

	50Hz	63 Hz	80 Hz	100 Hz	125 Hz	160 Hz	200 Hz
$p_{\max}$	1.8076	1.7921	1.7309	1.6898	1.5983	1.4857	1.3690
$p_{\min}$	0.1088	0.1544	0.1995	0.2789	0.3761	0.5012	0.6237

The measured absorption coefficients α_{meas}, the calculated absorption coefficients α_{FDTD}, and the errors are presented in table 5-16.

Table 5-16 From 50Hz to 200Hz , the measured absorption coefficients, the calculated absorption coefficients, and the errors.

	50Hz	63 Hz	80 Hz	100Hz	125Hz	160Hz	200Hz
α_{meas}	0.240	0.269	0.361	0.534	0.636	0.773	0.858
α_{FDTD}	0.214	0.292	0.371	0.487	0.617	0.755	0.860
$\lvert\alpha_{FDTD}-\alpha_{meas}\rvert$	0.026	0.023	0.010	0.047	0.019	0.018	0.002
$\lvert\alpha_{FDTD}-\alpha_{meas}\rvert/\alpha_{meas}$	10.8%	8.5%	2.7%	8.8%	2.9%	2.3%	0.2%

In Fig.5.27, the calculated absorption coefficients are plotted by the red dotted line, from 50Hz to 200Hz. The measured sound absorption coefficients are plotted by the black line.

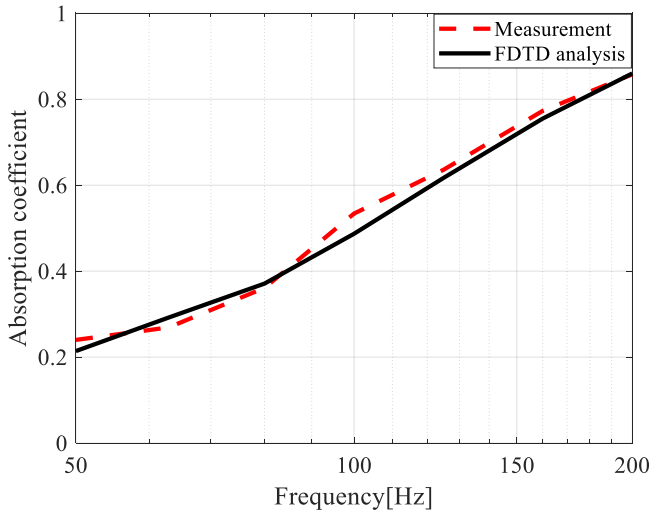

Fig.5.27 The measured absorption coefficients and the calculated absorption coefficients.

5.4 The measurement and the FDTD analysis for sample B

5.4.1 The measurement results

For sample B, the width of the porous materials is 0.8m and the total height is 0.3m. The manufactured porous materials used in the measurement are shown in Fig.5.28.

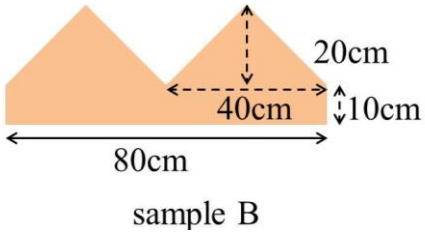

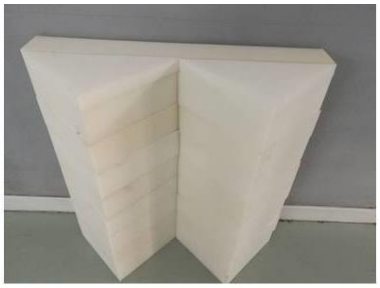

Fig.5.28 The customized porous materials for sample B.

Fig.5.29 shows the measurement photo on the site. In the measurement, the costumed porous materials are settled at the end of the low frequency impedance tube. In the measurement, the porous materials are backed by the rigid wall without air space.

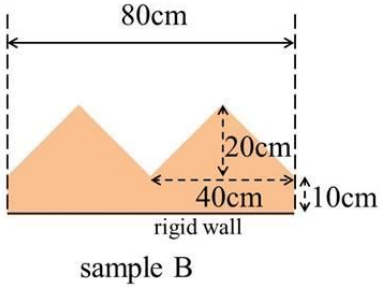

Fig.5.29 The measurement photo on the site for sample B.

As shown in Fig.5.30, a movable microphone is moving from position A to position B, recording the values of the sound pressure level in the impedance tube. From 50Hz to 200Hz, the recorded values of the sound pressure level are plotted, as shown in Fig.5.31.

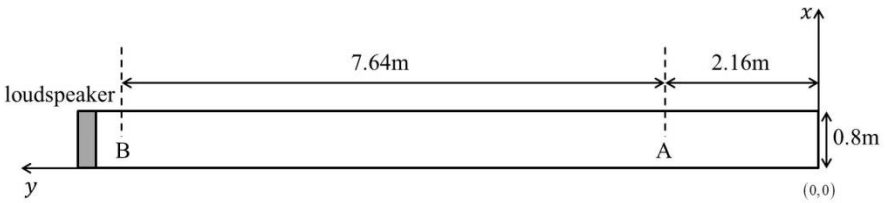

Fig.5.30 The microphone is moving from postion A to position B.

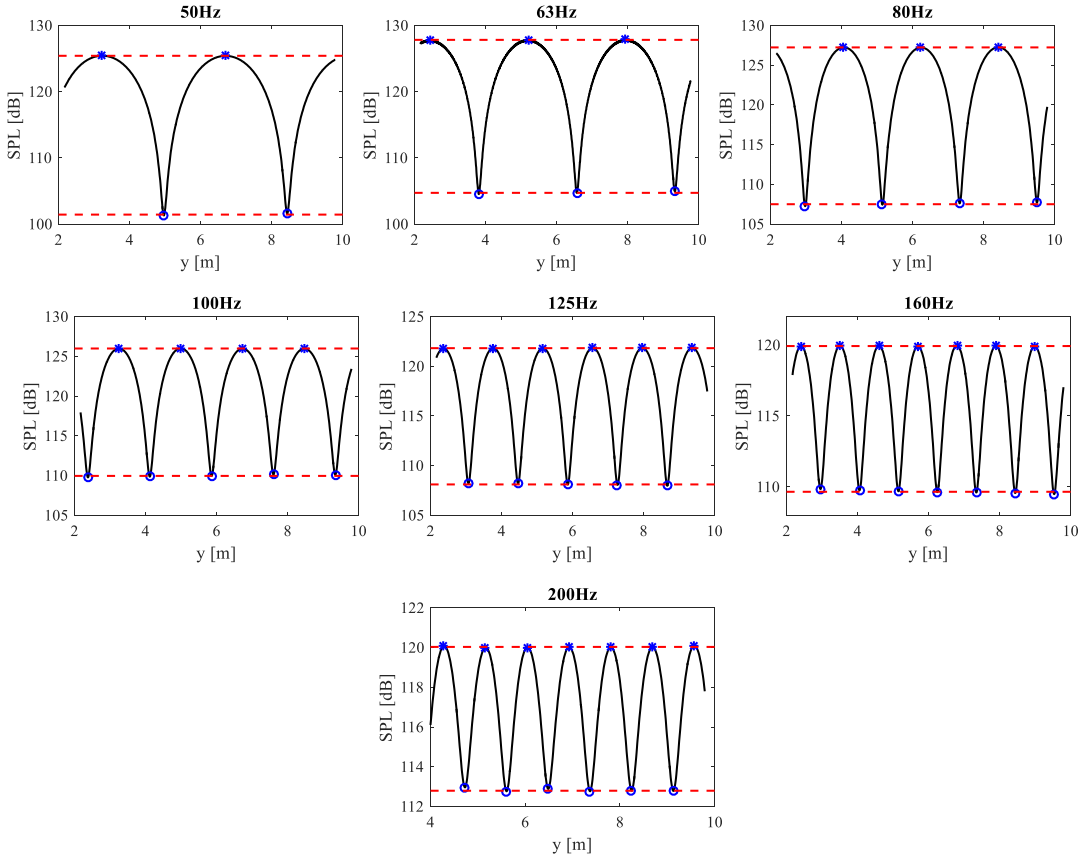

Fig.5.31 From 50Hz to 200Hz, the measured sound pressure level for sample B.

In the measurement, the measured sound pressure levers are shown in Fig.5.31. Blue * represent the searched maximum values of the sound pressure levels. Then these maximum values are averaged, which is the value of $SPL_{\max}$, plotted by the upper dotted red line. Blue o represent the searched minimum sound pressure levels. Then these minimum values are averaged, which is the value of $SPL_{\min}$, plotted by the lower dotted red line.

From 50Hz to 200Hz, the calculated values of $SPL_{\max}$, the calculated values of $SPL_{\min}$ and the absorption coefficient α_{meas} are presented in table 5-17.

Table 5-17 The measured absorption coefficients from 50Hz to 200Hz.

	50Hz	63 Hz	80 Hz	100 Hz	125 Hz	160 Hz	200 Hz
SPL_{max}	125.42	127.83	127.24	125.99	121.83	119.93	120.03
SPL_{min}	101.44	104.72	107.51	109.96	108.11	109.66	112.79
α_{meas}	0.224	0.244	0.339	0.471	0.567	0.718	0.845

5.4.2 The FDTD analysis for sample B

5.4.2.1 FDTD setting

In the FDTD analysis, two-dimensional sound field setting is illustrated in Fig.5.32. The four boundaries in the computation domain are both rigid walls. Corresponding to the measurement, there is no air gap between the porous material and the backed rigid wall. The length of the computation domain is 10m, and the width of the computation domain is 0.8m. The discrete time interval is 1.75×10^{-6} s. In order to obtain precision numerical results, the discrete space intervals Δx and Δy are both 0.002m. Therefore, in x direction, the number of the discrete grids Ax is 400. In y direction, the number of the discrete grids Ay is 5000. Two positions are marked in the figure. In the y direction, position a is at y=0.3m, and position b is at y=4.3m.

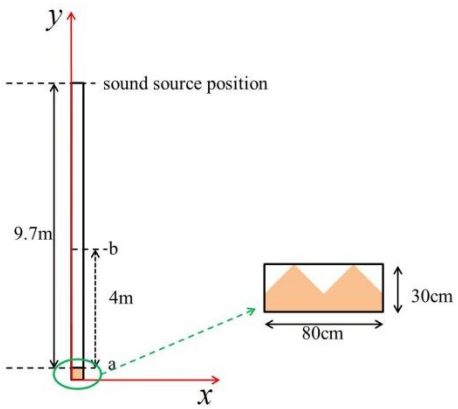

Fig.5.32 Two-dimensional sound field in the FDTD analysis for sample B.

The sound source is input at the top position in the y direction ($y=10\text{m}$), given as the plane wave incidence. At the position of the sound source, the sound pressure is

updated by using Eq.(5.4). The frequency of the sound source is chosen from these values: 50, 63, 80, 100, 125, 160, 200.

In the calculation, the sound pressures at these positions $(Ax/2, y_a)$, $(Ax/2, y_a+1)\ldots$ $(Ax/2, y_b)$ are saved. y_a is corresponding to the position a (y=0.3m), and y_b is corresponding to the position b (y=4.3m).

5.4.2.2 The result of the calculation

As an example, when the frequency of the sound source f_c is 200Hz, the distribution of the sound pressure ($0 \le x \le 0.8m, 0 \le y \le 1.5$m) are shown in Fig.5.33.

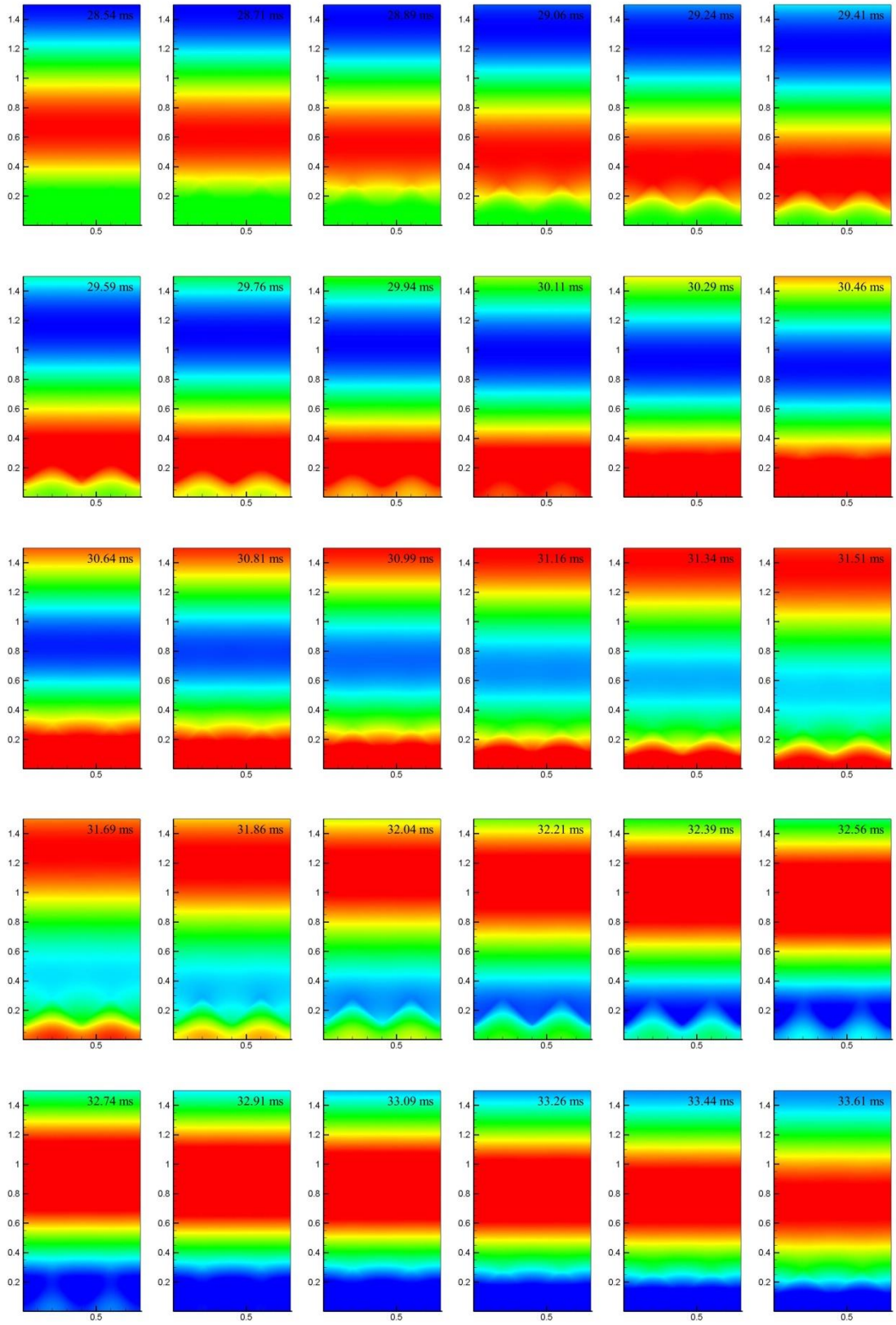
28.54 ms
28.71 ms
28.89 ms
29.06 ms
29.24 ms
29.41 ms
29.59 ms
29.76 ms
29.94 ms
30.11 ms
30.29 ms
30.46 ms
30.64 ms
30.81 ms
30.99 ms
31.16 ms
31.34 ms
31.51 ms
31.69 ms
31.86 ms
32.04 ms
32.21 ms
32.39 ms
32.56 ms
32.74 ms
32.91 ms
33.09 ms
33.26 ms
33.44 ms
33.61 ms

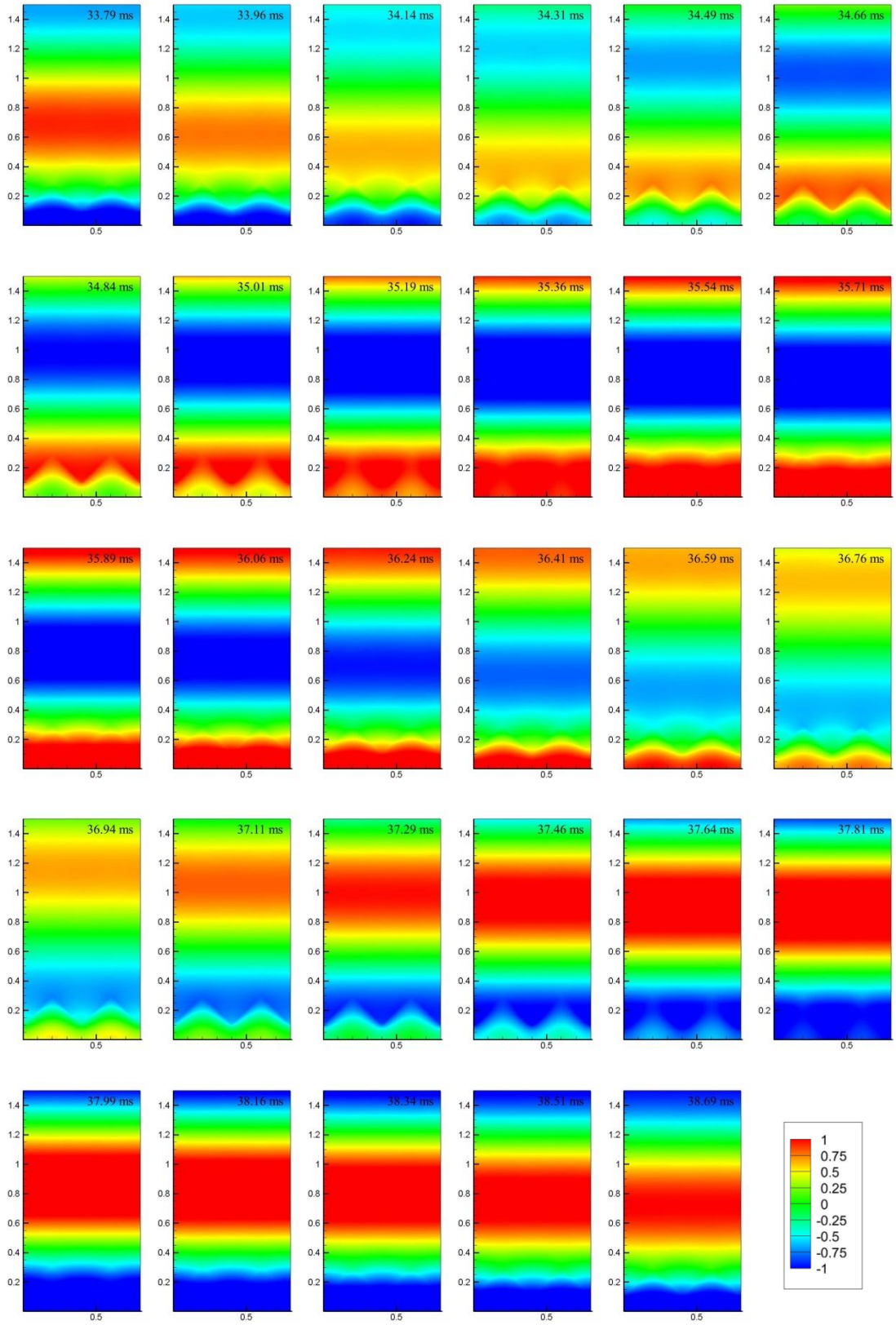

Fig.5.33 At different time step, the calculated sound pressures ($0 \le x \le 0.8m, 0 \le y \le 1.5\text{m}$).

The calculated sound pressures at these positions are shown in Fig.5.34.

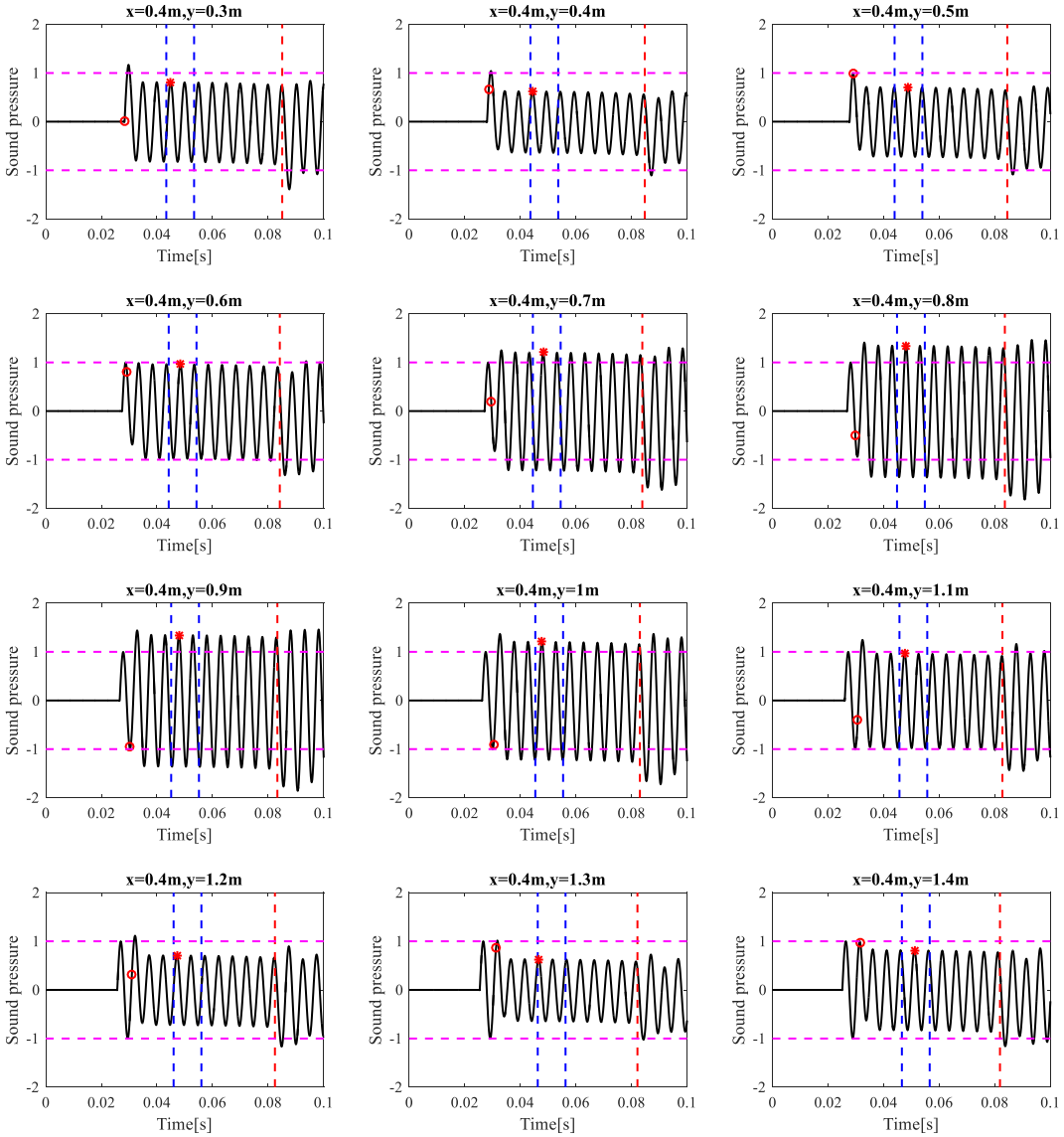

Fig.5.34 For 200Hz, the calculated sound pressures at different positions.

In fig.5.34, the time point for receiving the first reflection wave from the surface of the porous materials is T_r, which is plotted by red o.

The time range $[T_s \quad T_e]$ for searching the stable standing wave field are represented by the blue dotted lines, where $T_s = T_r + M/f_c$ and $T_e = T_s + N/f_c$. In the FDTD numerical simulation, the positions for these receiving points are from y=0.4m to y=4.4m. Then the following equation is obtained:

$$M + N \le MN_{\max} = \frac{11.4 \cdot f_c}{c_0}. \tag{5.22}$$

Table 5-18 The values of $MN_{\max}$

	50Hz	63Hz	80Hz	100Hz	125Hz	160Hz	200Hz
$MN_{\max}$	1.67	2.10	2.67	3.33	4.17	5.33	6.67

In Fig.5.34, M is equal to 3, and N is equal to 2 for 200Hz. The amplitude of the standing wave is the maximum value of the sound pressures at the time range $[T_s \quad T_e]$, which is plotted by red *.

By using the same method, at different positions, the amplitudes of the standing wave can be obtained. When the frequency of the sound source f_c is 200Hz, the amplitudes of the standing wave at different positions ($x = 0.4m, 0.5\text{m} \le y \le 4.5\text{m}$) are plotted, as shown in Fig.5.35.

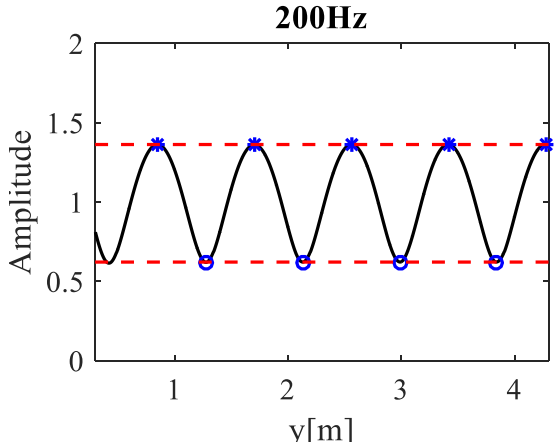

Fig.5.35 For 200Hz, the amplitudes of the standing wave

In Fig.5.35, the 5 minimum values are 0.6148 (y=0.424m), 0.6199 (y=1.28m), 0.6218(y=2.132m), 0.6220(y=2.992m) and 0.6222(y=3.842m). Although the difference between the first minimum value and the other values is small, the first minimum value is not used here. Near the surface of the porous materials, the sound field is very complicate, and affecting the amplitudes of the standing wave. For 200Hz, the first minimum value occurs at the position near the surface of the porous materials. This minimum value may be affected, and it is not used for the calculation.

Fig.5.36 shows the searched amplitudes of the standing wave from 50Hz to 160Hz. The values of M and N in the calculation are listed in table 5-19.

Table 5-19 The values of M and N in the calculation

	50 Hz	63 Hz	80 Hz	100 Hz	125 Hz	160 Hz	200 Hz
M	0.6	1	1.5	2	2.5	2	3
N	1	1	1	1	1	2	2

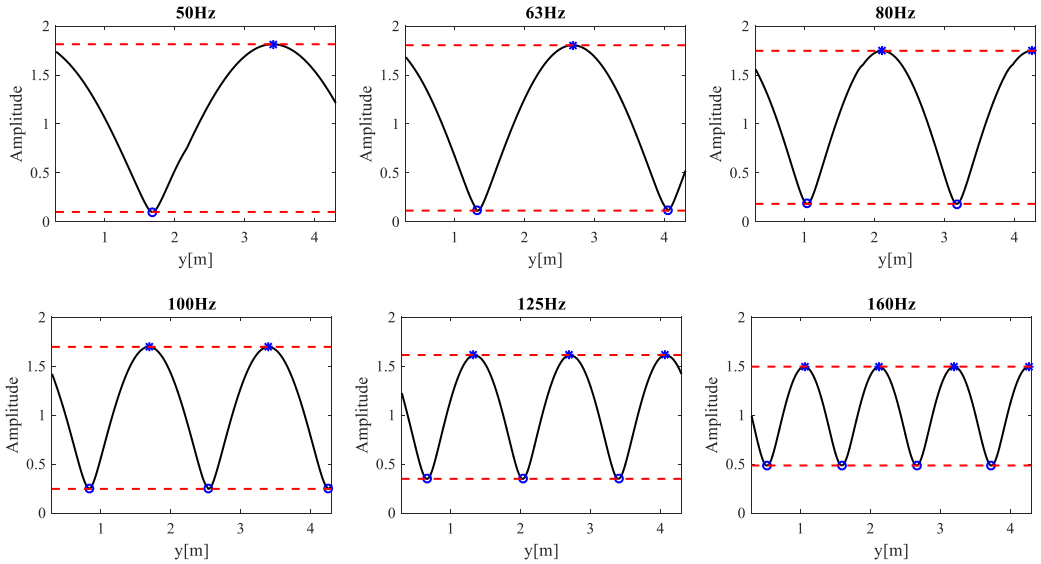

Fig.5.36 For 50Hz-160Hz, the searched amplitudes of the standing wave.

In Fig.5.36, blue * represents the searched maximum values. Then these maximum values are averaged, which is the value of $p_{\max}$, plotted by the upper dotted red line. Blue o represents the searched minimum values. Then these minimum values are averaged, which is the value of $p_{\min}$, plotted by the lower dotted red line. The values of $p_{\max}$ and the values of $p_{\min}$ are listed in table 5-15.

Table 5-20 The calculated values and the absorption coefficient

	50Hz	63 Hz	80 Hz	100 Hz	125 Hz	160 Hz	200 Hz
$p_{\max}$	1.8145	1.8042	1.7472	1.6977	1.6143	1.4955	1.3626
$p_{\min}$	0.1006	0.1141	0.1834	0.2464	0.3490	0.4856	0.6215
α_{FDTD}	0.199	0.224	0.344	0.443	0.585	0.740	0.861

5.4.3 Contrast the measurement results and the FDTD analysis results

The two results and the errors are given in table 5-21. It can be found that the maximum value of the absolute errors is at 100Hz, which is 0.028. The maximum value of the relative errors is at 50Hz, which is 11.1%.

Table 5-21 The measured absorption coefficients, the calculated absorption coefficients, and the errors.

	50Hz	63 Hz	80 Hz	100Hz	125Hz	160Hz	200Hz
α_{meas}	0.224	0.244	0.339	0.471	0.567	0.718	0.845
α_{FDTD}	0.199	0.224	0.344	0.443	0.585	0.740	0.861
$\lvert\alpha_{FDTD}-\alpha_{meas}\rvert$	0.025	0.020	0.005	0.028	0.018	0.022	0.016
$\lvert\alpha_{FDTD}-\alpha_{meas}\rvert/\alpha_{meas}$	11.1%	8.1%	1.4%	5.9%	3.1%	3.0%	1.8%

In Fig.5.37, the calculated absorption coefficients are plotted by the red dotted line, from 50Hz to 200Hz. The measured sound absorption coefficients are plotted by the black line.

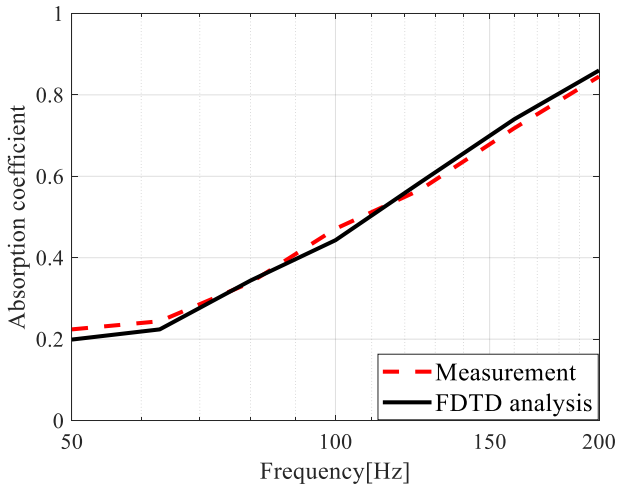

Fig.5.37 The measured absorption coefficients and the calculated absorption coefficients.

5.5 The measurement and the FDTD analysis for sample C

5.5.1 The measurement results

The sample C and the manufactured porous materials in the measurement are illustrated in Fig.5.38. 4 pieces of the samples are made by a factory. The height of the customized porous materials is 0.8m, and the width of the porous materials is 0.8m.

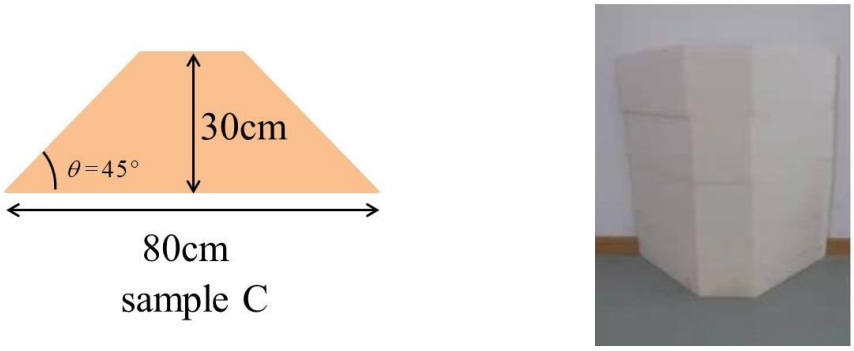

Fig.5.38 The sample C and the customized porous material.

Fig.5.39 shows the measurement photo on the site. In the measurement, the costumed porous materials are settled at the end of the low frequency impedance tube. In the measurement, there is no air gap settled between the porous material and the backed rigid wall.

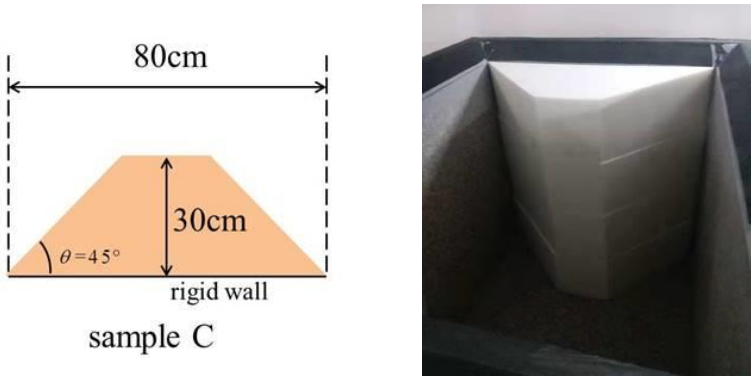

Fig.5.39 The measurement photo on the site for sample C.

In the measurement, the loudspeaker emits continues single frequency sinusoidal wave. As shown in Fig.5.40, a movable microphone is moving from position A to position B, recording the values of the sound pressure level in the impedance tube. From 50Hz to 200Hz, the recorded values of the sound pressure level are plotted, as given in Fig.5.41.

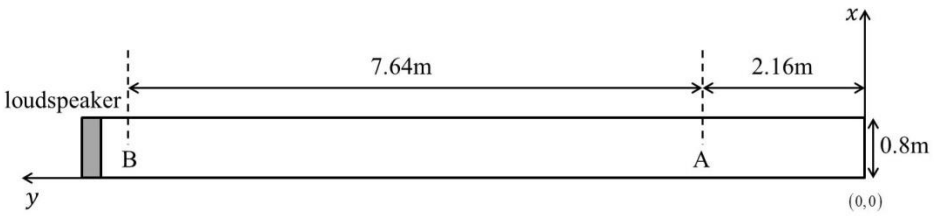

Fig.5.40 The microphone is moving from postion A to position B.

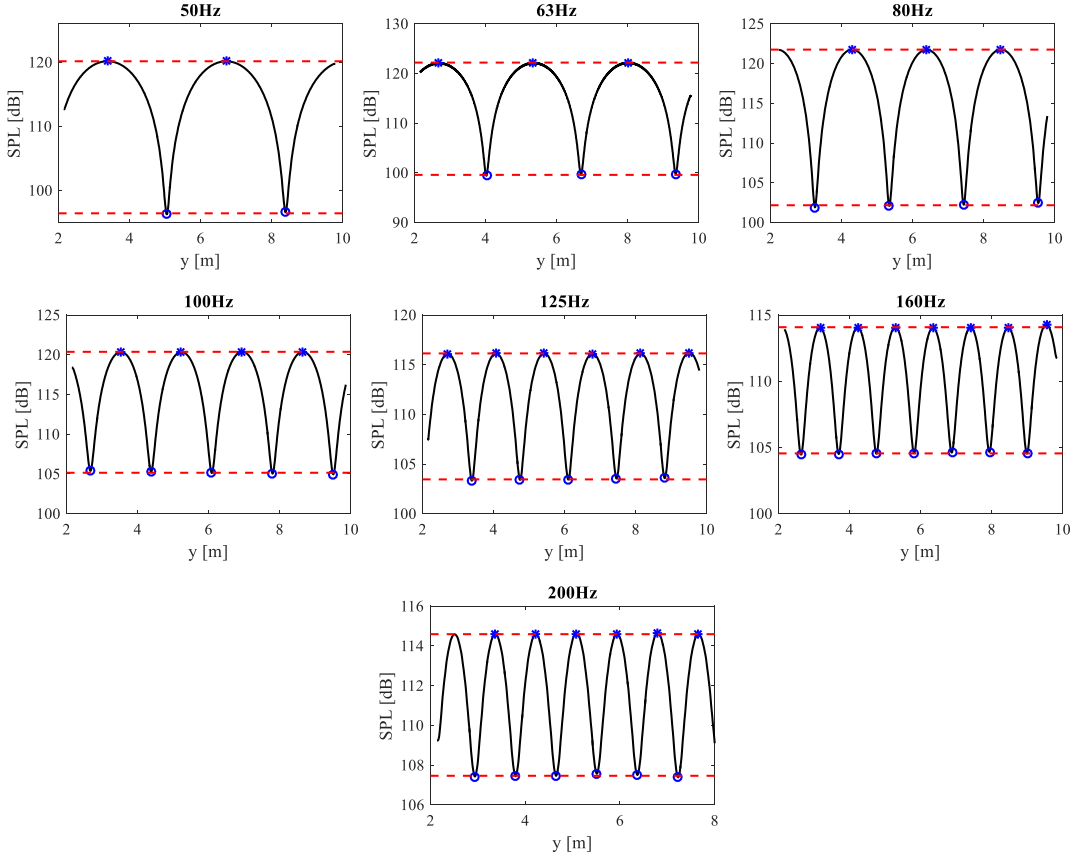

Fig.5.41 The measured sound pressure level for sample C.

In Fig.5.41, the measured values of the sound pressure lever are shown. Blue * represent the searched maximum values of the sound pressure levels. Then these maximum values are averaged, which is the value of SPL_{max}, plotted by the upper dotted red line. Blue o represent the searched minimum sound pressure levels. Then these minimum values are averaged, which is the value of SPL_{min}, plotted by the lower dotted red line.

For each frequency, the values of SPL_{max}, the values of SPL_{min} and the absorption coefficients α_{meas} are given in table 5-22.

Table 5-22 From 50Hz to200Hz, the measured absorption coefficients.

	50Hz	63 Hz	80 Hz	100 Hz	125 Hz	160 Hz	200 Hz
SPL_{max}	120.16	122.20	121.76	120.37	116.14	114.08	114.60
SPL_{min}	96.44	99.59	102.17	105.16	103.46	104.56	107.47
α_{meas}	0.230	0.257	0.344	0.504	0.612	0.751	0.849

5.5.2 The FDTD analysis for sample C

5.5.2.1 FDTD setting

In the FDTD analysis, two-dimensional sound field setting is illustrated in Fig.5.42. The four boundaries in the computation domain are both rigid walls. Corresponding to the measurement, there is no air gap between the porous material and the backed rigid wall. The length of the computation domain is 10m, and the width of the computation domain is 0.8m. The discrete time interval is 1.75×10^{-6} s. In order to obtain precision numerical results, the discrete space intervals Δx and Δy are both 0.002m. Therefore, in x direction, the number of the discrete grids Ax is 400. In y direction, the number of the discrete grids Ay is 5000. Two positions are marked in the figure. In the y direction, position a is at y=0.3m, and position b is at y=4.3m.

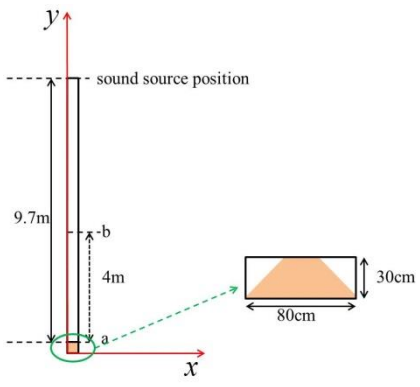

Fig.5.42 Two-dimensional sound field for the FDTD analysis.

The sound source is input at the top position in the y direction ($y=10\text{m}$), given as the plane wave incidence. At the position of the sound source ($y=10\text{m}$), the sound

pressure is updated by using Eq.(5.4). The frequency of the sound source is chosen from these values: 50, 63, 80, 100, 125, 160, and 200.

In the FDTD analysis, the sound pressures at these positions $(Ax/2, y_a)$, $(Ax/2, y_a+1)\ldots$ $(Ax/2, y_b)$ are saved. y_a is corresponding to the position a (y=0.3m), and y_b was corresponding to the position b (y=4.3m).

5.5.2.2 The result of the calculation

As an example, the calculated sound pressures ($0 \le x \le 0.8m, 0 \le y \le 1.5$m) from 28.54ms to 38.69ms are shown in Fig.5.43. The frequency of the sound source f_c is 200Hz.

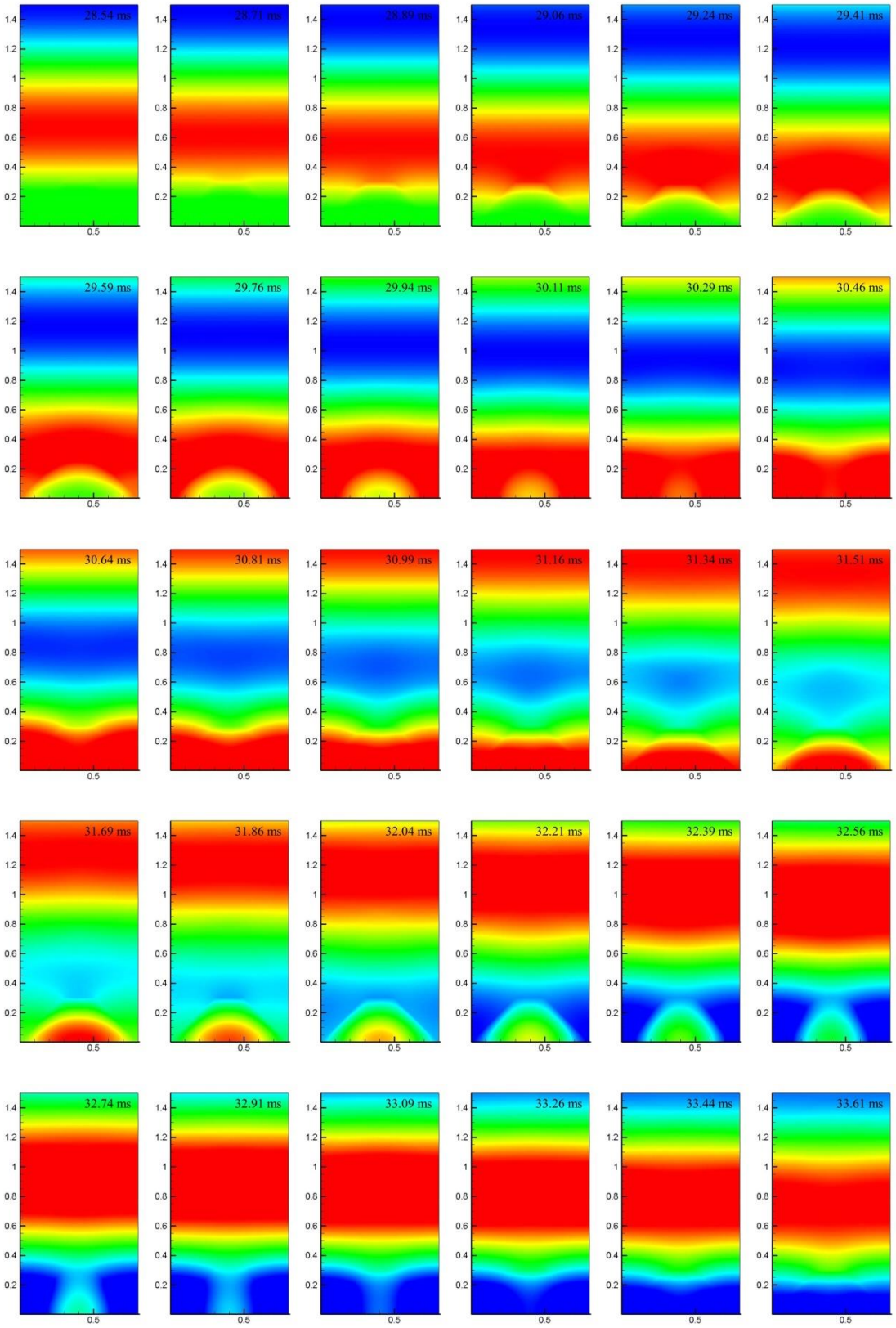
28.54 ms
28.71 ms
28.89 ms
29.06 ms
29.24 ms
29.41 ms
29.59 ms
29.76 ms
29.94 ms
30.11 ms
30.29 ms
30.46 ms
30.64 ms
30.81 ms
30.99 ms
31.16 ms
31.34 ms
31.51 ms
31.69 ms
31.86 ms
32.04 ms
32.21 ms
32.39 ms
32.56 ms
32.74 ms
32.91 ms
33.09 ms
33.26 ms
33.44 ms
33.61 ms

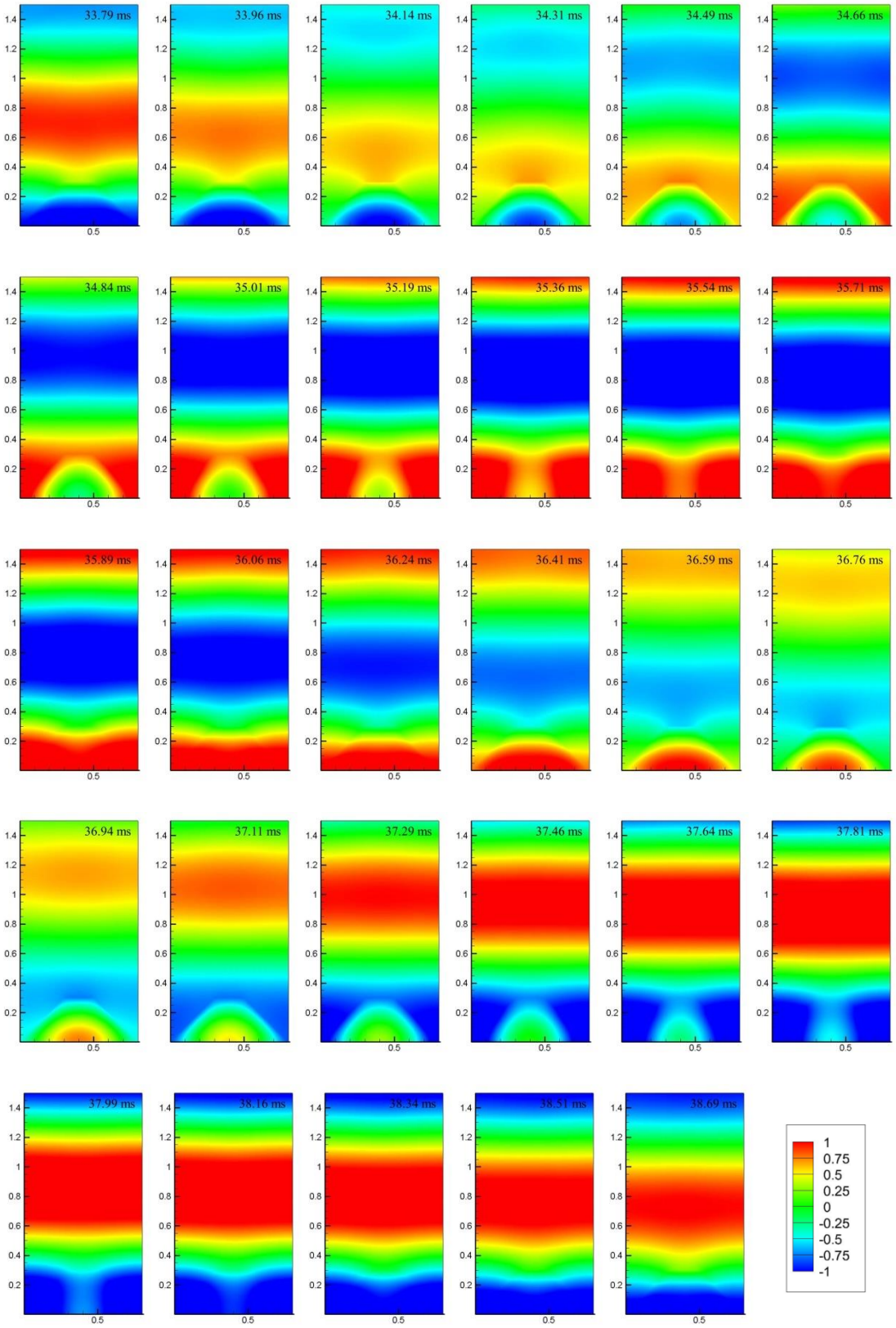

Fig.5.43 At different time step, the calculated sound pressures ($0 \le x \le 0.8m, 0 \le y \le 1.5\text{m}$).

The calculated sound pressures at these positions are given in Fig.5.44.

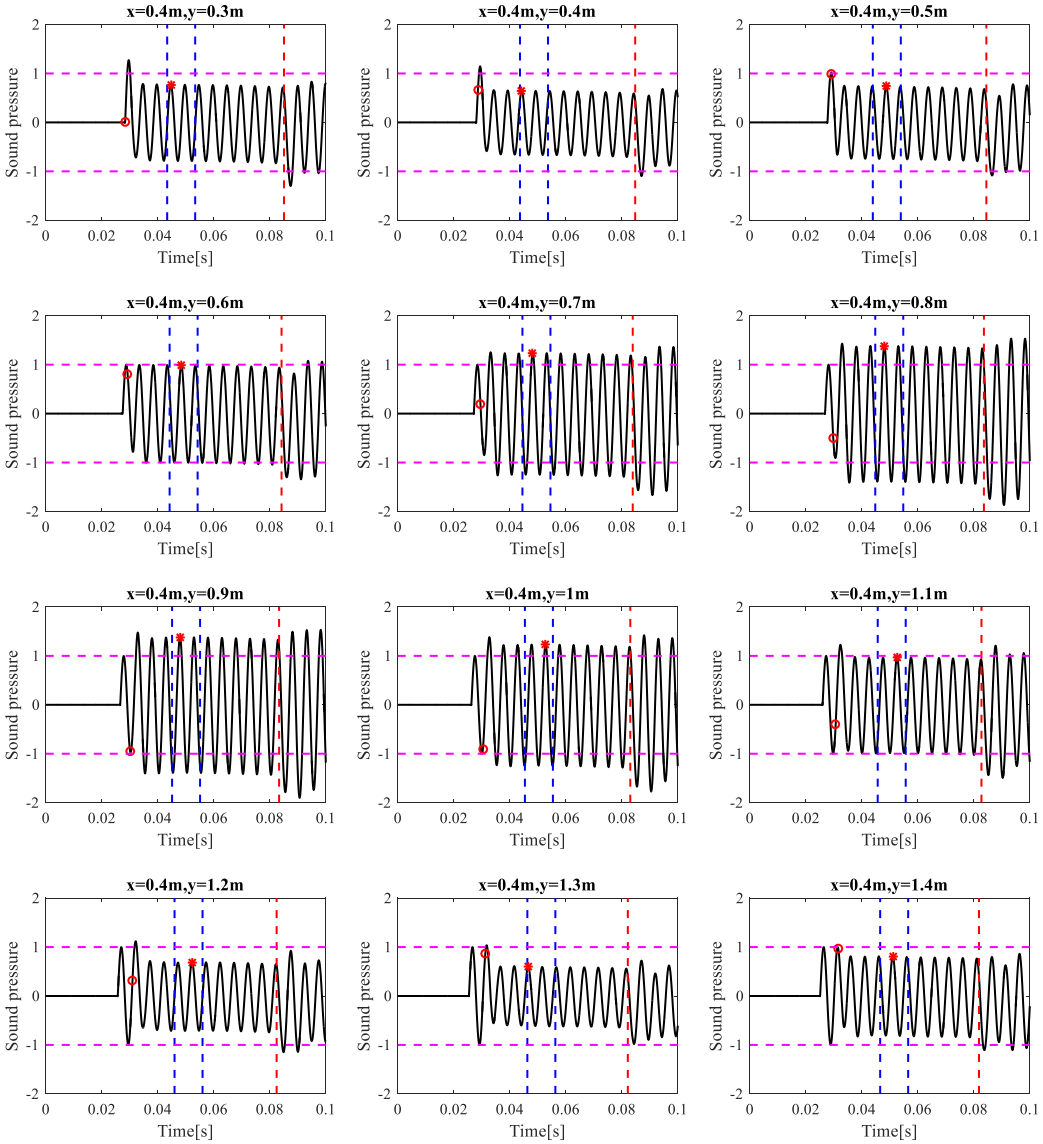

Fig.5.44 For 200Hz, the calculated sound pressures.

In Fig.5.44, the time point for receiving the first reflection wave from the surface of the porous materials is T_r, which is plotted by red o.

The time range $[T_s \quad T_e]$ for searching the stable standing wave field are represented by the blue dotted lines, where $T_s = T_r + M/f_c$, $T_e = T_s + N/f_c$ and $T_e \le T_{\max}$. $T_{\max}$ is represent by the red dotted line, given by using Eq.(5.9). In the FDTD calculation, the positions for the receiving points are from y=0.3m to y=4.3m. Then the relationship between the value of M and the value of N is obtained:

$$M + N \le MN_{\max} = \frac{11.4 \cdot f_c}{c_0}. \tag{5.23}$$

Table 5-23 The values of $MN_{\max}$

	50Hz	63Hz	80Hz	100Hz	125Hz	160Hz	200Hz
$MN_{\max}$	1.67	2.10	2.67	3.33	4.17	5.33	6.67

In Fig.5.44, M is equal to 3, and N is equal to 2 for 200Hz. The searched amplitude of the standing wave is the maximum value of the sound pressures between the time range $[T_s \quad T_e]$, which is plotted by red *.

By using the same method, the amplitude of the standing wave for each frequency can be obtained. The amplitudes of the standing wave ($x = 0.4m, 0.3\text{m} \le y \le 4.3\text{m}$) are shown in Fig.5.45.

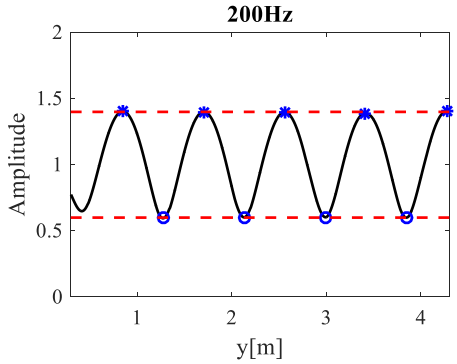

Fig.5.45 For 200 Hz, the amplitude of the standing wave

In Fig.5.46, the searched amplitudes of the standing wave are plotted for 50Hz-160Hz. The values of M and N in the calculation are presented in table 5-24.

Table 5-24 The values of M and N in the calculation

	50 Hz	63 Hz	80 Hz	100 Hz	125 Hz	160 Hz	200 Hz
M	0.6	1	1.5	2	2.5	2	3
N	1	1	1	1	1	2	2

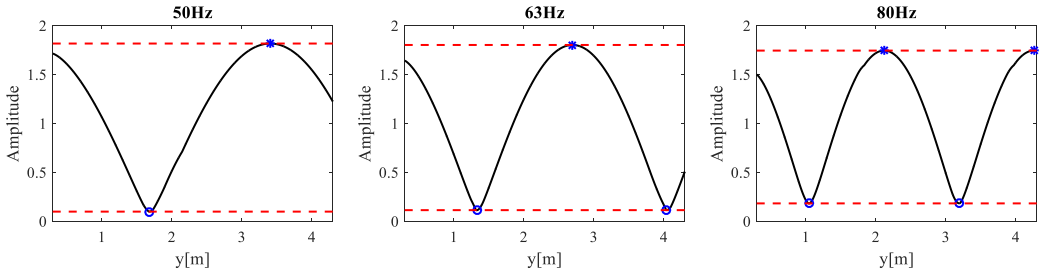

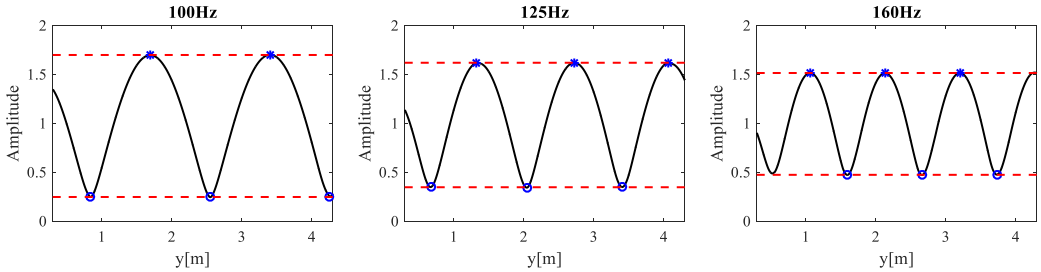

Fig.5.46 For 50Hz-160Hz, the searched amplitude of the standing wave.

In Fig.5.45 and Fig.5.46, blue * represents the searched maximum values. Then these maximum values are averaged, which is the value of $p_{\max}$, plotted by the upper dotted red line. Blue o represents the searched minimum values. Then these minimum values are averaged, which is the value of $p_{\min}$, plotted by the lower dotted red line. The value of $p_{\max}$ and the value of $p_{\min}$ are given in table 5-15. For 160Hz and 200Hz, the first maximum value is not used for the calculation.

In table 5-25, the values of $p_{\max}$, the values of $p_{\min}$ and the calculated absorption coefficients α_{FDTD} are listed.

Table 5-25 The calculated absorption coefficient

	50Hz	63 Hz	80 Hz	100 Hz	125 Hz	160 Hz	200 Hz
$p_{\max}$	1.8195	1.8049	1.7473	1.6992	1.6197	1.5152	1.3970
$p_{\min}$	0.1020	0.1171	0.1861	0.2481	0.3477	0.4745	0.5978
α_{FDTD}	0.201	0.229	0.348	0.445	0.5820	0.727	0.840

5.5.3 Contrast the measurement results and the FDTD analysis results

The two results and the errors are given in table 5-26. It can be found that the maximum value of the absolute errors is at 100Hz, which is 0.059. The maximum value of the relative errors is at 50Hz, which is 12.6%.

Table 5-26 The measured absorption coefficients, the calculated absorption coefficients, and the errors.

	50Hz	63 Hz	80 Hz	100Hz	125Hz	160Hz	200Hz
α_{meas}	0.230	0.257	0.344	0.504	0.612	0.751	0.849
α_{FDTD}	0.201	0.229	0.348	0.445	0.582	0.727	0.840
$\lvert\alpha_{FDTD}-\alpha_{meas}\rvert$	0.029	0.028	0.004	0.059	0.030	0.024	0.009
$\lvert\alpha_{FDTD}-\alpha_{meas}\rvert/\alpha_{meas}$	12.6%	10.9%	1.1%	11.7%	4.9%	3.2%	1.0%

In Fig.5.47, the calculated absorption coefficients are plotted by the red dotted line, from 50Hz to 200Hz. The measured sound absorption coefficients are plotted by the black line.

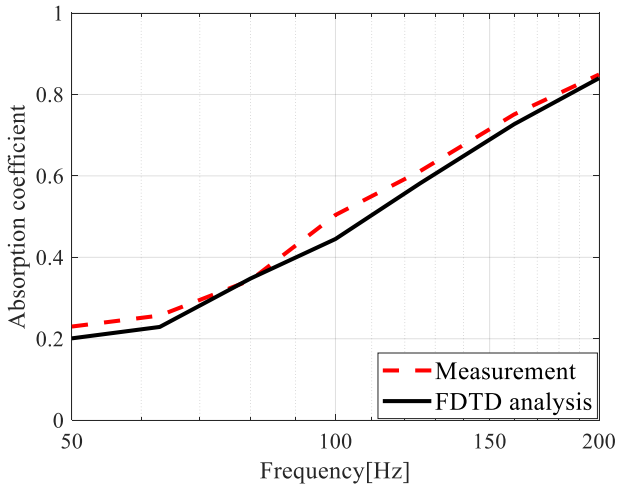

Fig.5.47 The measured absorption coefficients and the calculated absorption coefficients.

5.6 The measurement and the FDTD analysis for sample D

5.6.1 The measurement results for sample D

For sample D, the width of the porous materials is 0.8m, and the height of the porous materials is 0.4m. The customized porous materials used for the measurement are illustrated in Fig.5.48.

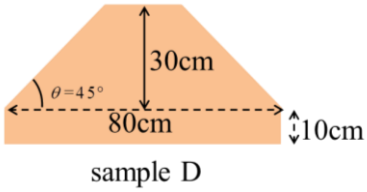

Fig.5.48 The sample D and the customized porous materials.

Fig.5.49 shows the measurement photo on the site. In the measurement, the costumed porous materials are simply stacked at the end of the low frequency impedance tube. An air gap of 0.1m is set between the porous materials and the backed rigid wall. The glue is not used in the measurement. Therefore, there may be some air gap between the pieces of the samples. The height of the customized porous materials is 0.8m, and the total width of the porous materials is 0.8m.

Fig.5.49 The measurement photo on the site for sample D.

As shown in Fig.5.50, a movable microphone is moving from position A to position B, recording the values of the sound pressure level in the impedance tube. In

the measurement, the recorded values of the sound pressure level from 50Hz to 200Hz as shown in Fig.5.51.

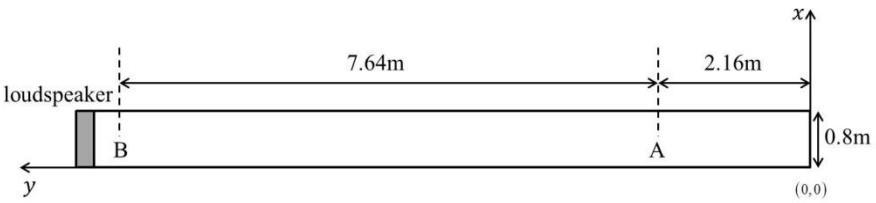

Fig.5.50 The microphone is moving from postion A to position B.

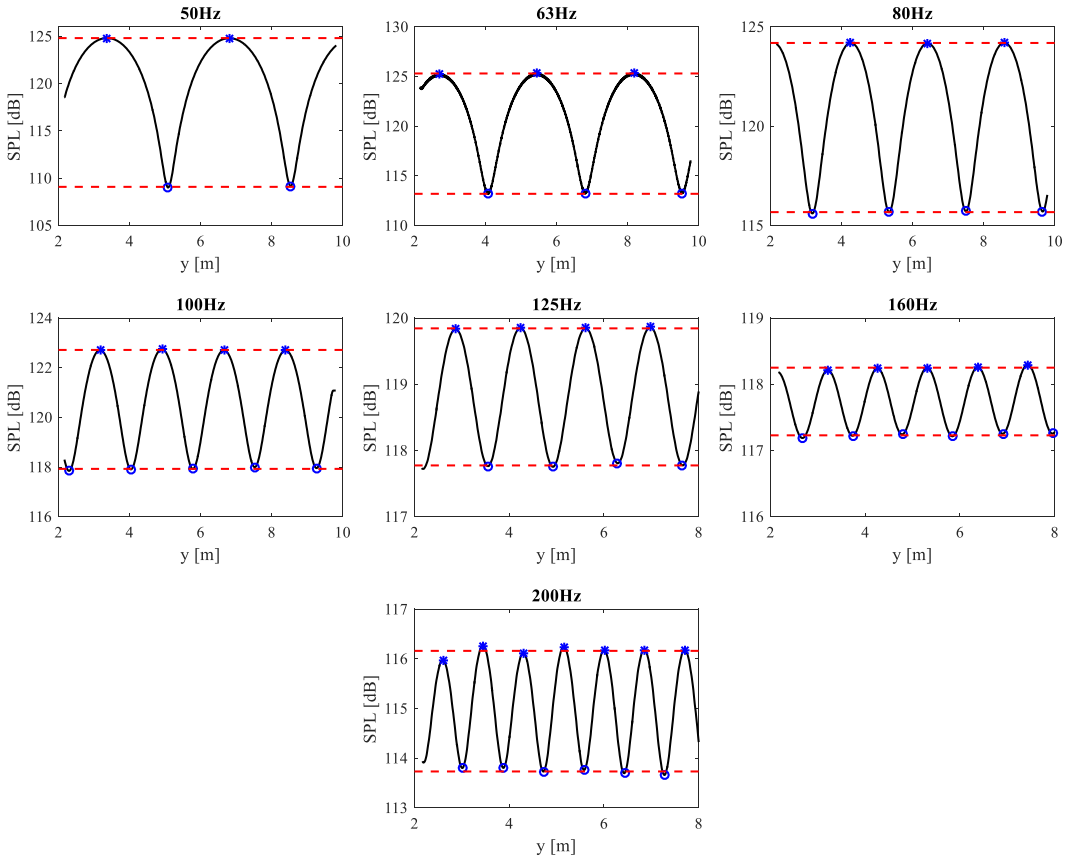

Fig.5.51 The measured sound pressure level by the moving microphone for sample D.

Blue * represent the maximum values of the sound pressure level. Then these maximum values are averaged, which is the value of $SPL_{\max}$, plotted by the upper dotted red line. Blue o represent the minimum values of the sound pressure level. Then these minimum values are averaged, which is the value of $SPL_{\min}$, plotted by the lower dotted red line.

From 50Hz to 200Hz, the calculated values of $SPL_{\max}$, the calculated values of $SPL_{\min}$, and the calculated absorption coefficients α_{meas} are presented in table 5-27.

Table 5-27 The measured absorption coefficients from 50Hz to 200Hz

	50Hz	63 Hz	80 Hz	100 Hz	125 Hz	160 Hz	200 Hz
$SPL_{\max}$	124.81	125.31	124.19	122.72	119.84	118.25	116.16
$SPL_{\min}$	109.09	113.19	115.67	117.93	117.77	117.23	113.73
α_{meas}	0.484	0.637	0.793	0.928	0.986	0.997	0.981

5.6.2 The FDTD analysis for sample D

5.6.2.1 FDTD setting

In the FDTD analysis, two-dimensional sound field setting is illustrated in Fig.5.52. The four boundaries in the computation domain are both rigid walls. Corresponding to the measurement, the air gap of 0.1m is set between the porous material and the backed rigid wall. The length of the computation domain is 10m, and the width of the computation domain is 0.8m. The discrete time interval is 1.75×10^{-6} s. In order to obtain precision numerical results, the discrete space intervals Δx and Δy are both 0.002m. Therefore, in x direction, the number of the discrete grids Ax is 400. In y direction, the number of the discrete grids Ay is 5000. Two positions are marked in the figure. In the y direction, position a is at y=0.5m, and position b is at y=4.5m.

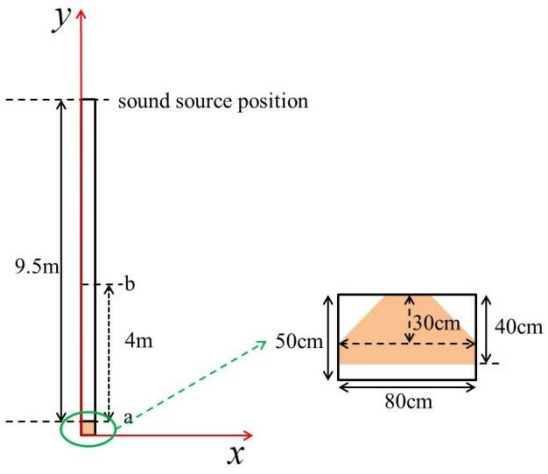

Fig.5.52 Two-dimensional sound field for the FDTD analysis.

The sound source is input at the top position in y direction ($y = 10\text{m}$), given as the plane wave incidence. At the position of the sound source ($y = 10\text{m}$), the sound pressure is updated by using Eq.(5.4). The frequency of the sound source is chosen from these values: 50, 63, 80, 100, 125, 160, and 200.

In the calculation, the sound pressures at these positions $(Ax/2, \text{y}_\text{a})$, $(Ax/2, \text{y}_\text{a}+1)\ldots$ $(Ax/2, \text{y}_b)$ are saved. y_a is corresponding to the position a (y=0.5m), and y_b is corresponding to the position b (y=4.5m).

5.6.2.2 The result of the calculation

As an example, when the frequency of the sound source f_c is 200Hz, the calculated sound pressures ($0 \le x \le 0.8m, 0 \le y \le 1.5\text{m}$) from 27.78ms to 37.93ms are shown in Fig.5.53.

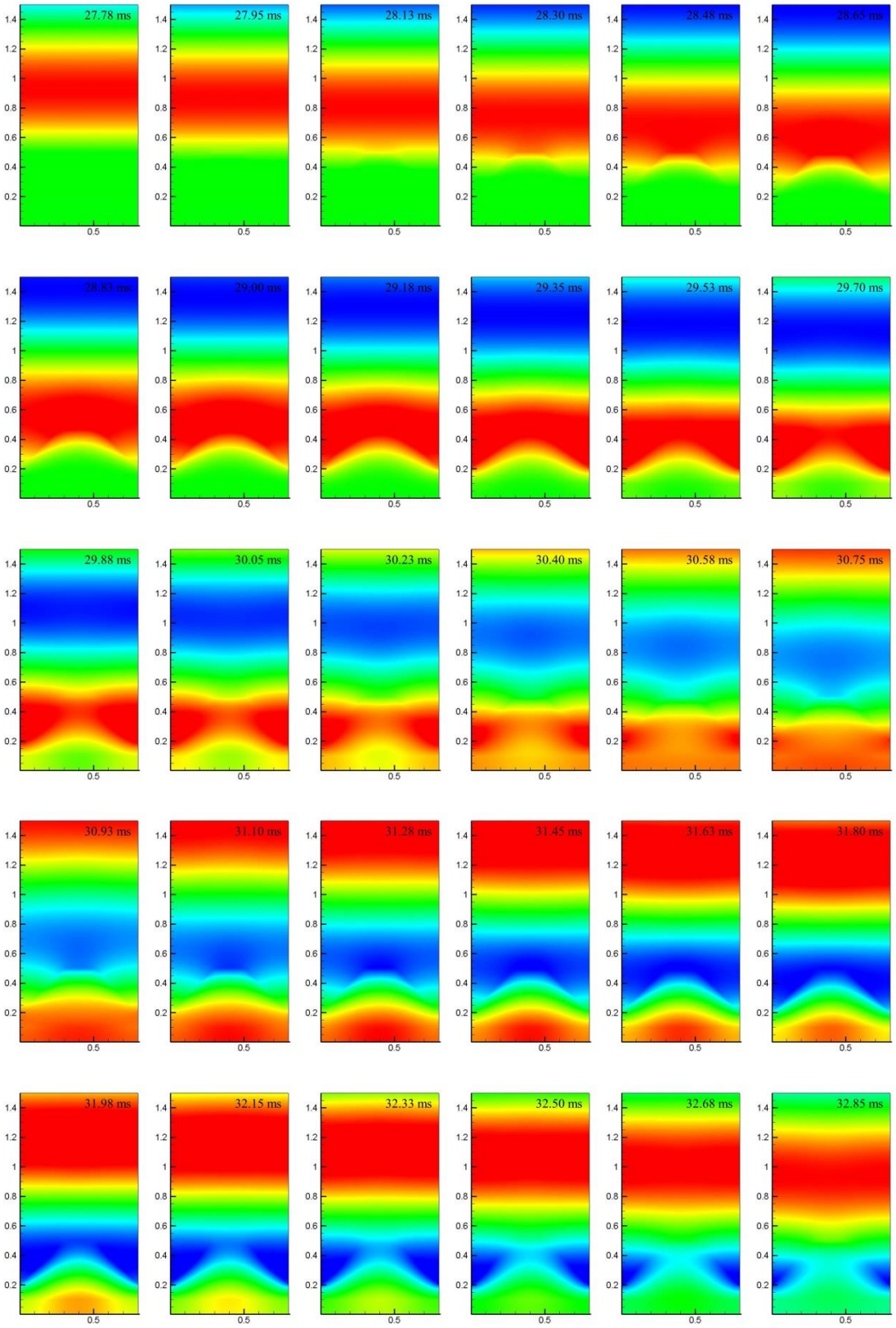
27.78 ms
27.95 ms
28.13 ms
28.30 ms
28.48 ms
28.65 ms
28.83 ms
29.00 ms
29.18 ms
29.35 ms
29.53 ms
29.70 ms
29.88 ms
30.05 ms
30.23 ms
30.40 ms
30.58 ms
30.75 ms
30.93 ms
31.10 ms
31.28 ms
31.45 ms
31.63 ms
31.80 ms
31.98 ms
32.15 ms
32.33 ms
32.50 ms
32.68 ms
32.85 ms

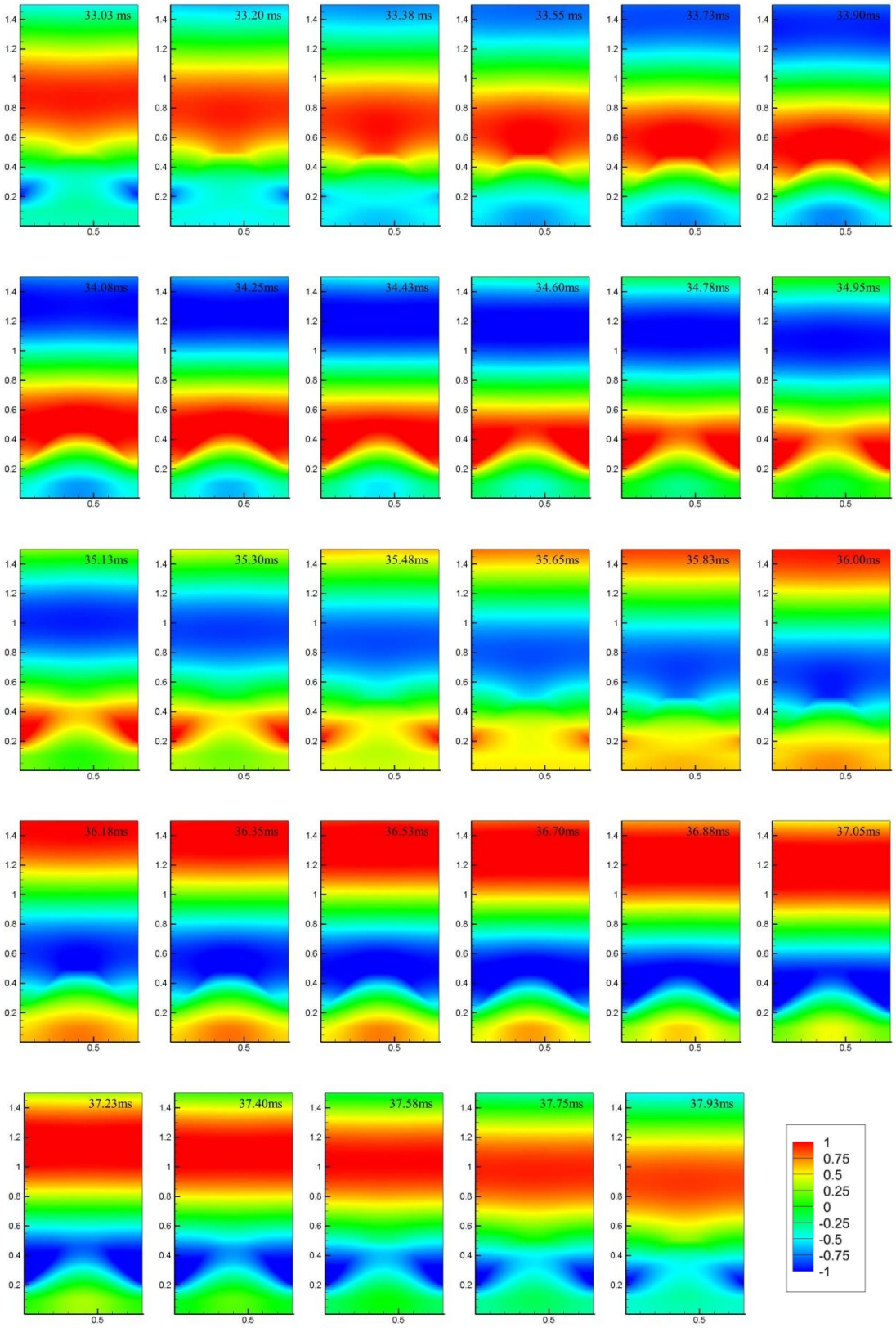

Fig.5.53 From 27.78ms to 37.93ms, the distribution of the calculated sound pressures ($0 \le x \le 0.8m, 0 \le y \le 1.5\text{m}$).

The calculated sound pressures at these positions are shown in Fig.5.54.

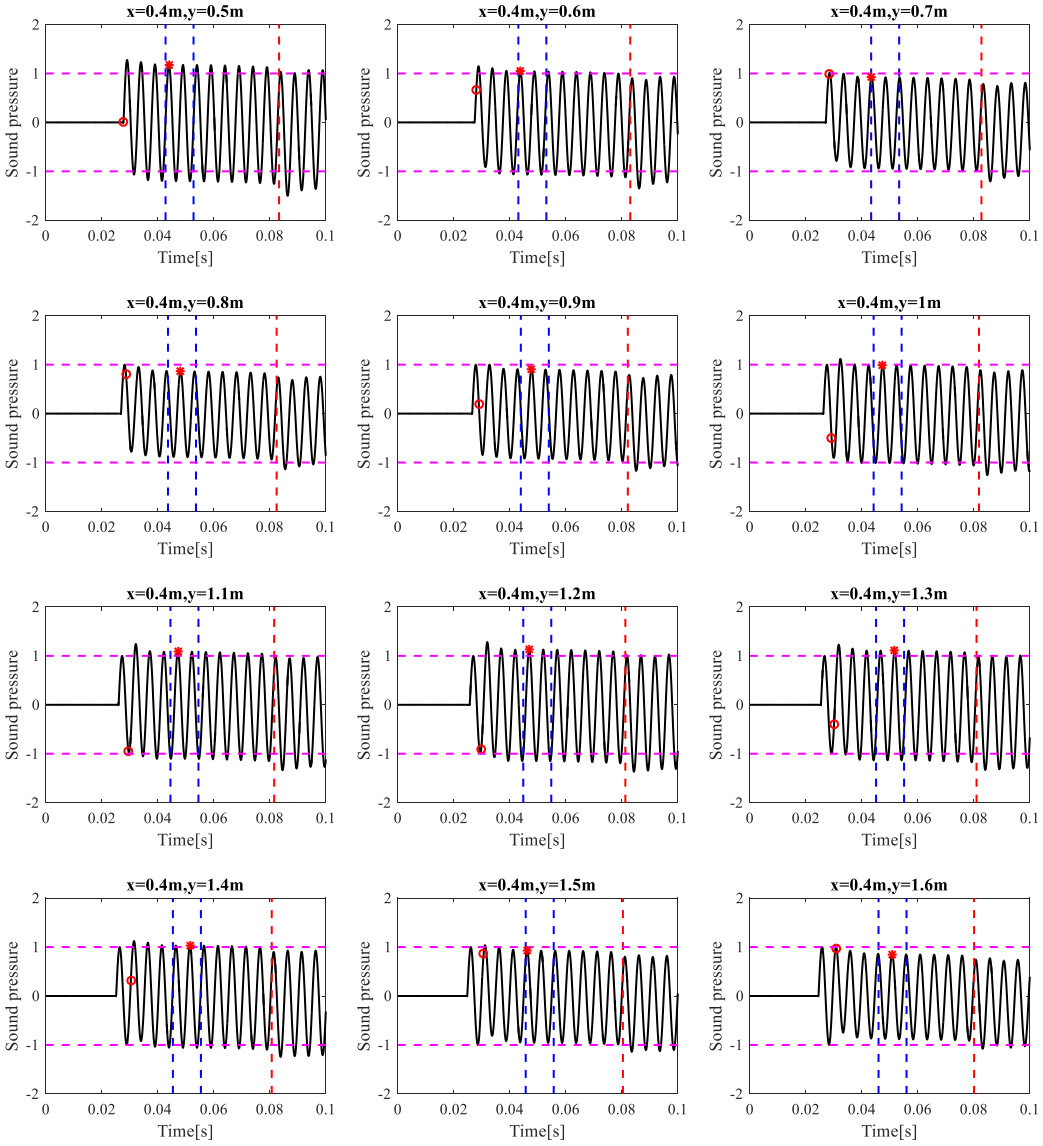

Fig.5.54 For 200Hz, the calculated sound pressure.

In Fig.5.54, the time point for receiving the first reflection wave from the surface of the porous materials is T_r, which is plotted by red o.

The time range $[T_s \quad T_e]$ for searching the stable standing wave field are represented by the blue dotted lines, where $T_s = T_r + M/f_c$, $T_e = T_s + N/f_c$ and $T_e \le T_{\max}$. $T_{\max}$ is calculated by using Eq.(5.9), represent by the red dotted line. In the FDTD calculation, the positions for the receiving points are from y=0.5m to y=4.5m. Then the relationship between the value of M and the value of N is obtained:

$$M+N \le MN_{\max} = \frac{11 \cdot f_c}{c_0}. \tag{5.24}$$

Table 5-28 The values for $MN_{\max}$

	50Hz	63Hz	80Hz	100Hz	125Hz	160Hz	200Hz
$MN_{\max}$	1.60	2.02	2.57	3.21	4.02	5.14	6.43

In Fig.5.54, M is equal to 3, and N is equal to 2 for 200Hz. The searched amplitude of the standing wave is the maximum value of the sound pressures between the time range $[T_s \quad T_e]$, which is plotted by red *.

By using the same method, the amplitudes of the standing wave at different positions can be obtained. When the frequency of the sound source f_c is 200Hz, the amplitudes of the standing wave ($x = 0.4\text{m}, 0.5\text{m} \le y \le 4.5\text{m}$) are plotted, as shown in Fig.5.54.

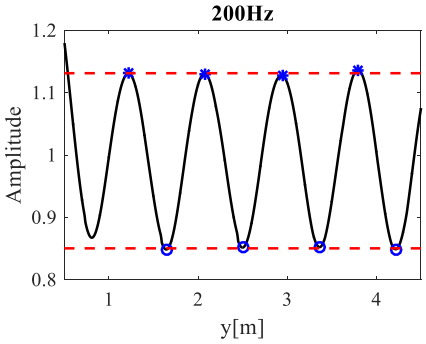

Fig.5.55 For 200Hz, the searched amplitude of the standing wave.

From 50Hz to 160Hz, the searched amplitudes of the standing wave are plotted, as shown in Fig.5.55. The values of M and N in the calculation are given in table 5-29.

Table 5-29 The values of M and N in the calculation.

	50 Hz	63 Hz	80 Hz	100 Hz	125 Hz	160 Hz	200 Hz
M	0.6	1	1.5	2.2	2.8	2	3
N	1	1	1	1	1	2	2

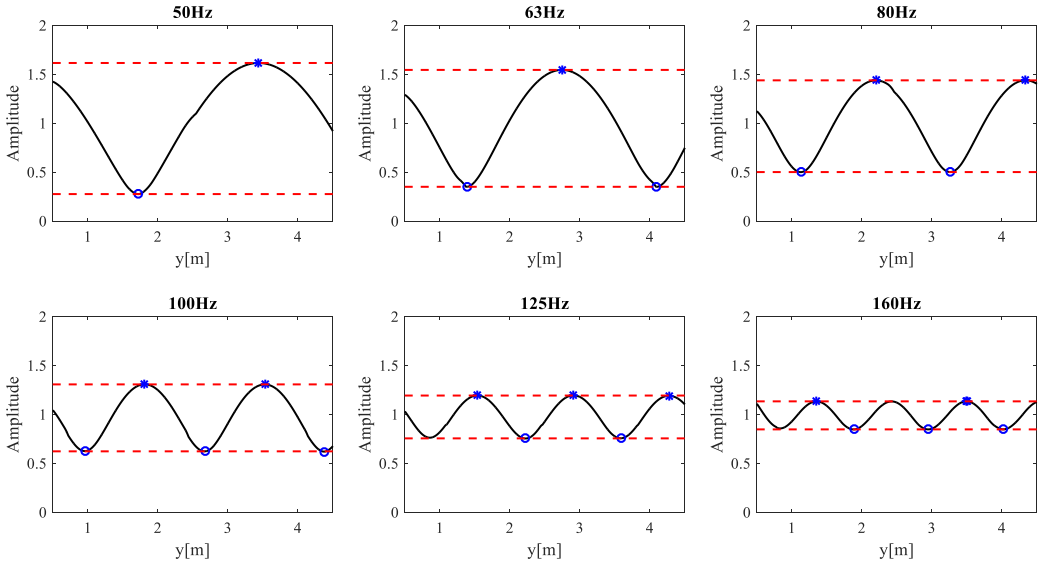

Fig.5.56 For different frequency, the amplitudes of the standing wave.

In Fig.5.56, blue * represents the searched maximum values. Then these maximum values are averaged, which is the value of $p_{\max}$, plotted by the upper dotted red line. Blue o represents the searched minimum values. Then these minimum values are averaged, which is the value of $p_{\min}$, plotted by the lower dotted red line. The value of $p_{\max}$ and the value of $p_{\min}$ are given in table 5-15. For 125Hz, 160Hz and 200Hz, the first minimum value of the amplitudes is not used.

The calculated values of $p_{\max}$, the calculated values of $p_{\min}$ and the calculated absorption coefficients α_{FDTD} are presented in table 5-30.

Table 5-30 The calculated absorption coefficients

	50Hz	63 Hz	80 Hz	100 Hz	125 Hz	160 Hz	200 Hz
$p_{\max}$	1.6174	1.5465	1.4400	1.3088	1.1947	1.1354	1.1312
$p_{\min}$	0.2778	0.3522	0.5027	0.6246	0.7571	0.8490	0.8502
α_{FDTD}	0.500	0.604	0.767	0.875	0.9497	0.979	0.980

5.6.3 Contrast the measurement results and the FDTD analysis results

The measured absorption coefficients α_{meas}, the calculated absorption coefficients α_{FDTD}, and the errors are presented in table 5-31. It can be found that the maximum value of the absolute errors is at 100Hz, which is 0.053. The maximum value of the relative errors is at 100Hz, which is 5.7%.

Table 5-31 The measured absorption coefficients, the calculated absorption coefficients, and the errors.

	50Hz	63 Hz	80 Hz	100Hz	125Hz	160Hz	200Hz
α_{meas}	0.484	0.637	0.793	0.928	0.986	0.997	0.981
α_{FDTD}	0.500	0.604	0.767	0.875	0.950	0.979	0.980
$\lvert\alpha_{FDTD}-\alpha_{meas}\rvert$	0.016	0.033	0.026	0.053	0.036	0.018	0.001
$\lvert\alpha_{FDTD}-\alpha_{meas}\rvert/\alpha_{meas}$	3.3%	5.1%	3.2%	5.7%	3.6%	1.8%	0.1%

In Fig.5.57, the calculated absorption coefficients are plotted by the red dotted line, from 50Hz to 200Hz. The measured sound absorption coefficients are plotted by the black line.

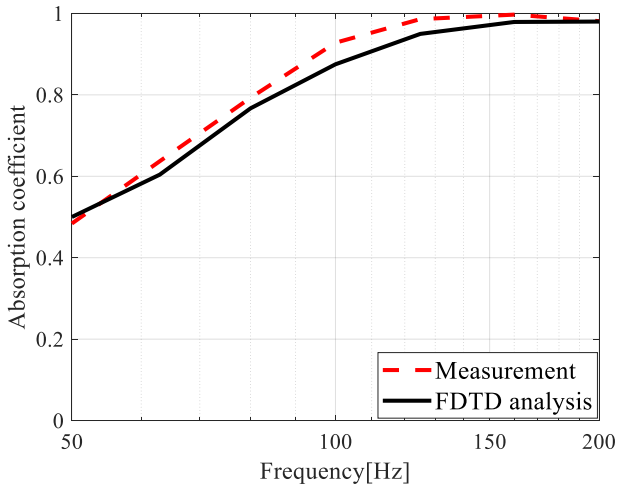

Fig.5.57 From 50Hz to 200Hz, the measured absorption coefficients and the calculated values.

5.7 Conclusion

In this chapter, the measurements and simulations for the 4 kinds of the shaped porous material are conducted. The main conclusions are given as follows:

(1) In the measurement, the samples are simply stacked together without using glue, which may cause some errors in the measured absorption coefficient.

(2) For the 4 kinds of samples, the calculated absorption coefficients are compared to the measured values. The maximum value of the absolute errors is for sample D, which is 0.053.

(3) The factor which significantly affects the result of the absorption coefficient is the start time point time point T_s. The best value for T_s is $T_s \geq T_r + 0.5/f_c$.

(4) For the 4 kinds of samples, the amplitudes of the standing wave near the top position of the samples are affected by the shape of the samples. When search the minimum value of the amplitudes of the standing wave, it needs to be careful to decide whether the first minimum value is used for the calculation.

Chapter 6 CONCLUSION

6.1 Summary of the dissertation

The EF-FDTD algorithm in the porous material with rigid flame is developed. The algorithm treat the frequency-domain wave equations based on the equivalent fluid model, by combining the IIR filter design methods and the Z transform theories, and the formulations in time domain for FDTD analysis are obtained. For the frequency-domain equations, the effective bulk modulus and the effective density are frequency dependent, which are designed in the form of the IIR filters. By applying the Z-transform theories, the whole wave equations are transformed to Z domain, avoiding the complex convolution operation in time domain. In Z domain, new parameters are defined, which greatly simplified the equations in the Z domain. The simplified equations and the defined parameters are easily transformed to the time domain, and formulations for the EF-FDTD algorithm are obtained. The formulations for 1-dimensional EF-FDTD algorithm, 2-dimensional EF-FDTD algorithm and 3-dimensional EF-FDTD algorithm are given.

The thermal effects are reflected in the EF-FDTD formulations, by the parameters of the designed IIR filters of the effective bulk modulus. The viscous effects in the porous materials are reflected in the EF-FDTD formulations, by the parameters of the designed IIR filters the effective density. Once the IIR filter of the effective bulk modulus and the effective density is determined, there is no need to design them again if the discrete time interval in the FDTD analysis is changed.

The EF-FDTD algorithm can also be simplified if the IIR filters designed for the effective bulk modulus and the effective density only have real poles.

The stability of the 1-dimensional EF-FDTD algorithm is discussed in detail. It is found that the stability of the algorithm is related with the parameters of the designed IIR filters, especially related with the number of the poles.

In chapter 4, the 1-dimensional EF-FDTD algorithm is validated under the normal incidence of the sound by comparing the numerical analysis and the experiment. 2 layers of the porous materials are constructed by one layer of glasswool 24k and one layer of glasswool 32k. The simulation and the measurement are conducted and compared by two cases (with air space and without air space). In the simulation, the boundary conditions are discussed. The calculated absorption coefficient generally agrees well with the measured result from 100 Hz to 6.4 kHz.

The 2-dimensional EF-FDTDT algorithm is validated under the oblique incidence of the sound. 4 layers of the porous materials are simulated in the numerical analysis. The oblique incident absorption coefficients by the numerical analysis are compared with the theoretical values. The calculated surface impedance is very close to the theoretical value in broad frequency range.

The simulations for the shaped porous material are discussed. When the shaped porous material is simulated, the staircase approximation can be adopted. The errors caused by the staircase approximation are discussed. It is found that when the discrete space interval becomes smaller, the error becomes smaller.

In chapter 5, the methods for calculating the absorption coefficient of the acoustic wedges are analyzed. The measurements and simulations for the 4 kinds of the wedges are conducted. For the 4 kinds of wedges, the calculated absorption coefficient is very close to the measured values. In the calculation, the factors which may affect the result of the absorption coefficient are discussed. The time point T_s for intercepting the calculated sound pressure is very important. The best value for T_s is $T_s \geq T_r + 0.5/f_c$. For the shaped samples, the sound field near the top position of the samples is very complicate, and the amplitude of the standing wave near the top position of the samples could be affected. When search the minimum value of the

amplitude of the standing wave, it needs to be careful to decide whether the first minimum value is used for the calculation.

6.2 Future Directions

Porous materials are frequently used in many places to reduce noise. Therefore, there exist some future directions for the prosed EF-FDTD algorithm.

One is the designing of the sound absorbing wedges in the anechoic chambers. In some places, the wedges need to be coved by the cloth or the panel. How to predict the absorption coefficient of these wedges needs to be solved. Another direction is to obtain the optimal geometry, dimensions, and materials for sound absorbing structures from the proposed EF-FDTD algorithm.

The other one is to study the behavior of the porous material under high sound pressure level. For this condition, the air flow velocity inside porous materials tends to be large that the flow resistance no longer follows Darcy low, which will affect the sound absorbing performance of porous material. The wave equations under high sound pressure level are given by Wilson and McIntosh. The methods used to deduce the EF-FDTD algorithm can be adopted in discrete these wave equations. The numerical analysis for the porous material under high sound pressure can be studied.

Appendix A. An example of designing IIR filter by MATLAB

In this thesis, $K_{eq}(\omega)$ and $\rho_{eq}(\omega)$ need to be designed in the form of IIR filters, which is expressed as:

$$H(j\omega)=\frac{b_1(j\omega)^n+b_2(j\omega)^{n-1}+\cdots b_{n+1}}{a_1(j\omega)^m+a_2(j\omega)^{m-1}+\cdots a_{m+1}}, \tag{A.1}$$

where ω is the angular frequency. The used form in the EF-FDTD algorithm is expressed as:

$$H(\omega)=k_0+\sum_{l=1}^{N}\frac{r_l}{j\omega-q_l}. \tag{A.2}$$

The function "invfreqs" in MATLAB can be used to design the IIR filter. The statement in the MATLAB is:

[b,a]=invfreqs(H,w,n,m,[],iter)

Here, b and a are the real numerator and denominator coefficient vectors of the transfer function; the vector H is the complex frequency response. Here H is the value of $K_{eq}(\omega)$ or $\rho_{eq}(\omega)$; the vector w is the angular frequency. The value of w is between 0 and π, corresponding to ω' in Eq.(A.3); scalars n and m is the desired orders of the numerator and denominator polynomials; the parameter iter is the number of the iterations in "invfreqs" function. The obtained IIR filter by using "invfreqs" function is expressed as:

$$H(j\omega)=\frac{b_1(j\omega')^n+b_2(j\omega')^{n-1}+\cdots b_{n+1}}{a_1(j\omega')^m+a_2(j\omega')^{m-1}+\cdots a_{m+1}}, \tag{A.3}$$

where ω' is between o and π, which is different from ω ($\omega=2\pi f$) in Eq.(A.1).

The obtained form of the IIR filter by using "invfreqs" function is different from that used for the EF-FDTD algorithm. Therefore, one key point here is to obtain the IIR filter in Eq.(A.2) by using "invfreqs" function from the measurement data.

The solutions are given as follows:

(1) The frequency is firstly scaled, and ω' is obtained. In the measurement, the highest frequency is denoted as fh. The following statement in MATLAB is used:

f_scale=fh*2;

w1=2*pi*f/ f_scale;

w1 is corresponding to ω' in Eq.(A.3), and the relationship between ω' and ω is:

$$\omega' = \frac{\omega}{f\_scale}. \tag{A.4}$$

(2) The "invfreqs" function is adopted:

[b,a]=invfreqs(h,w1,n,m,[],iter);

From this statement, Eq.(A.3) is obtained.

(3) The following statement is used:

[r,q,k]=residue(b,a);

From this statement, the following expression is obtained:

$$H(\omega) = k + \sum_{l=1}^{N} \frac{r_l}{j\omega' - q_l}. \tag{A.5}$$

By using Eq.(A.4), Eq.(A.5) becomes:

$$H(\omega) = k + \sum_{l=1}^{N} \frac{r_l}{j\dfrac{\omega}{f\_scale} - q_l} = k + \sum_{l=1}^{N} \frac{r_l \times f\_scale}{j\omega - q_l \times f\_scale}. \tag{A.6}$$

(3) The following statement is used:

q1=q* f_scale;

r1= r* f_scale;

From this statement, the following expressions can be obtained:

$$H(\omega) = k + \sum_{l=1}^{N} \frac{r_l}{j\omega - q_l}, \tag{A.7}$$

where q1 is corresponding to q_l in Eq.(A.7), and r1 is corresponding to r_l in Eq.(A.7).

One example for designing the IIR filter by using MATLAB is given as follows:

```
clear ;
close all;
clc;
c_air=342;     % sound speed
rho=1.213;     % density
z_air=c_air*rho;
j=sqrt(-1);
fl=100;     % the lowest frequency
fh=6400;    % the highest frequency
f=fl:fh;    % the frequency
w0=2*pi*f; % the original angular frequency
 %%%%%%%%%%%%%%%%%%%%%%%%%%%%%%%%%%%%%%%%%%%
Rf=8000;       % flow resistivity
a=1+0.07 *(f/Rf).^(-0.632);
b= -0.107*(f/Rf).^(-0.632);
zc_miki=z_air*(a+j*b); %   miki model
c=1+0.109*(f/Rf).^(-0.618);
d= -0.160*(f/Rf).^(-0.618);
k_miki=(c+j*d).*w0/c_air; % wave number in   miki model
%%%%%%%%%%%%%%%%%%%%%%%%%%%%%%%%%%%%%%%%%%%%
bulk_material=w0.*zc_miki./k_miki;
bulk_air=rho*c_air*c_air;
bulk_normalized=bulk_material/bulk_air;     % the normalized bulk modulus
%%%%%%%%%%%%%%%%%%%%%%%%%%%%%%%%%%%%%%%%%%%
f_scale=fh*2;
w1=2*pi*f/f_scale;    % the sclaed   angular frequency
%%%%%%%%%%%%%%%%%%%%%%%%%%%%%%%%%%%%%%%%%%%%
n=2;
```

```
m=2;

iter=30;

[b,a]=invfreqs(bulk_normalized,w1,n,m,[],iter);      % design IIR filter for the normalized bulk modulus

%%%%%%%%%%%%%%%%%%%%%%%%%%%%%%%%%%%%%%%%%%%%

[r,q,k]=residue(b,a);

r1=r*f_scale;

q1=q*f_scale;

k1=k;

%%%%%%%%%%%%%%%%%%%%%%%%%%%%%%%%%%%%%%%%%%%%

k2=k1*bulk_air;

r2=r1*bulk_air;

q2=q1;

[b2,a2]=residue(r2,q2,k2);

%%%%%%%%%%%%%%%%%%%%%%%%%%%%%%%%%%%%%%%%%%%%

Num=polyval(b2,j*w0);    % numerator of the IIR filter

Den=polyval(a2,j*w0);    % denominator of the IIR filter

IIR_filter=Num./Den;

 %%%%%%%%%%%%%%%%%%%%%%%%%%%%%%%%%%%%%%%%%%%

figure;

semilogx(f,real(bulk_material),'r',f,real(IIR_filter),'k--');

hold on;

semilogx(f,imag(bulk_material),'r',f,imag(IIR_filter),'k--');

legend('Miki model', 'IIR filter')

xlabel('Frequency [Hz]');    ylabel('Effective bulk modulus');
```

Appendix B. Parameters for the design IIR filters

In section 4.3, 4.4 and 4.5, Miki model is used to calculate the acoustical properties of the porous material[81]. In Miki model, the characteristic impedance $Z_c(\omega)$ and the wave number $k(\omega)$ of the porous material are given by

$$Z_c(\omega) = \rho_0 c_0 \left[1 + 0.07(f/\sigma)^{-0.632} - j0.107(f/\sigma)^{-0.632}\right], \quad \text{(B.1)}$$

$$k(\omega) = \frac{\omega}{c_0}\left[1 + 0.109(f/\sigma)^{-0.618} - j0.160(f/\sigma)^{-0.618}\right]. \quad \text{(B.2)}$$

In Eq.(B.1) and Eq.(B.2), σ is the flow resistivity of the porous materials. Then effective bulk modulus $K_{eq}(\omega)$ and the effective density $\rho_{eq}(\omega)$ are:

$$K_{eq}(\omega) = \omega Z_c(\omega)/k(\omega), \quad \text{(B.3)}$$

$$\rho_{eq}(\omega) = Z_c(\omega)k(\omega)/\omega. \quad \text{(B.4)}$$

The parameters in the designed IIR filters for different porous materials are presented below. Here, the IIR filters are designed only having real poles between 100 Hz and 5000 Hz.

(1) $\sigma = 3000$ Nm^{-4}s

Table B-1 For the effective bulk modulus, parameters in the designed IIR filter.

k_0	q	r
140084.525293	-25415.892783	-135431078.779791
	-4461.127146	-52067306.554010
	-872.471579	-14197643.360053

Table B-2 For the effective density, parameters in the designed IIR filter.

k_0'	q'	r'
1.299242	-16283.561591	4259.657139
	-2055.019833	1479.207258
	-0.001588	2769.553538

(2) $\sigma = 5000\ \mathrm{Nm^{-4}s}$

Table B-3 For the effective bulk modulus, parameters in the designed IIR filter.

k_0	q	r
139596.513066	-28441.674057	-191419131.506220
	-5299.054988	-68751311.567228
	-1084.358710	-15276994.639450

Table B-4 For the effective density, parameters in the designed IIR filter.

k_0'	q'	r'
1.319538	-20277.013884	5896.527672
	-3067.221647	2111.060316
	-0.001881	4609.648368

(3) $\sigma = 8000\ \mathrm{Nm^{-4}s}$

Table B-5 For the effective bulk modulus, parameters in the designed IIR filter.

k_0	q	r
139069.973321	-32164.869905	-264883001.994329
	-6323.195398	-86741279.561776
	-1336.767720	-15987099.092468

Table B-6 For the effective density, parameters in the designed IIR filter.

k_0'	q'	r'
1.337897	-26248.122851	8099.659365
	-4541.795935	3080.183675
	-0.020987	7310.634474

(4) $\sigma = 10000\ \mathrm{Nm^{-4}s}$

Table B-7 For the effective bulk modulus, parameters in the designed IIR filter.

k_0	q	r
138797.849563	-34365.130589	-309890370.339827
	-6916.535420	-96038805.285083
	-1482.707892	-16255672.734029

Table B-8 For the effective density, parameters in the designed IIR filter.

k_0'	q'	r'
1.351565	-27749.383390	9316.372904
	-4997.915007	3430.863025
	-0.013373	9059.545631

(5) $\sigma = 15000\ \mathrm{Nm^{-4}s}$

Table B-9 For the effective bulk modulus, parameters in the designed IIR filter.

k_0	q	r
138286.098409	-39389.577011	-414906983.795335
	-8222.812162	-114040896.095543
	-1808.632084	-16728408.780645

Table B-10 For the effective density, parameters in the designed IIR filter.

k_0'	q'	r'
1.330098	-52752.999544	16388.064277
	-8223.757498	5969.940785
	-0.014820	13583.994837

(6) $\sigma = 20000\ \mathrm{Nm^{-4}s}$

Table B-11 For the effective bulk modulus, parameters in the designed IIR filter.

k_0	q	r
137934.210098	-44077.652532	-514398081.234544
	-9374.153903	-127712342.986942
	-2104.643816	-17132851.415772

Table B-12 For the effective density, parameters in the designed IIR filter.

k_0'	q'	r'
1.322781	-78464.610409	24856.494540
	-10761.779442	7958.490749
	-0.047831	18141.520380

Appendix C. EF-FDTD algorithm with High accuracy

In order to raise the accuracy of the EF-FDTD algorithm, $\partial f/\partial x$ can be expressed as[45]:

$$\frac{\partial f}{\partial x}=\frac{-f\left(x+\frac{3}{2}\Delta x\right)+27f\left(x+\frac{1}{2}\Delta x\right)-27f\left(x-\frac{1}{2}\Delta x\right)+f\left(x-\frac{3}{2}\Delta x\right)}{24\Delta x}. \tag{C.1}$$

Then, for the wave equation:

$$j\omega p+K_{eq}(\omega)\cdot\left(\frac{\partial u}{\partial x}+\frac{\partial v}{\partial y}+\frac{\partial w}{\partial z}\right)=0. \tag{C.2}$$

The EF-FDTD algorithm can be written as:

$$\begin{aligned}D(i,j,k)=&\frac{-u^n\left(i+\frac{3}{2},j,k\right)+27u^n\left(i+\frac{1}{2},j,k\right)-27u^n\left(i-\frac{1}{2},j,k\right)+u^n\left(i-\frac{3}{2},j,k\right)}{24\Delta x}\\&+\frac{-v^n\left(i,j+\frac{3}{2},k\right)+27v^n\left(i,j+\frac{1}{2},k\right)-27v^n\left(i,j-\frac{1}{2},k\right)+v^n\left(i,j-\frac{3}{2},k\right)}{24\Delta y}\\&+\frac{-w^n\left(i,j,k+\frac{3}{2}\right)+27w^n\left(i,j,k+\frac{1}{2}\right)-27w^n\left(i,j,k-\frac{1}{2}\right)+w^n\left(i,j,k-\frac{3}{2}\right)}{24\Delta z},\end{aligned} \tag{C.3}$$

$$\begin{aligned}p^{n+1/2}(i,j,k)=&\,p^{n-1/2}(i,j,k)-K_e\Delta t\cdot D(i,j,k)-\Delta t^2\sum_{l=1}^{N_1}a_l\cdot {I_l}^{n-1/2}(i,j,k)\\&-\Delta t^2\sum_{k=1}^{N_2}X1_k\cdot {Q_k}^{n-1/2}(i,j,k)-X2_k\cdot {Q_k}^{n-3/2}(i,j,k),\end{aligned} \tag{C.4}$$

$$\begin{aligned}{I_l}^{n+1/2}(i,j,k)=&\,b_l\cdot {I_l}^{n-1/2}(i,j,k)+D(i,j,k)\\&l=1,2\cdots N_1,\end{aligned} \tag{C.5}$$

$$\begin{aligned}{Q_k}^{n+1/2}(i,j,k)=&\,X3_k\cdot {Q_k}^{n-1/2}(i,j,k)-X4_k\cdot {Q_k}^{n-3/2}(i,j,k)+D(i,j,k)\\&k=1,2\cdots N_2.\end{aligned} \tag{C.6}$$

For the equation:

$$\frac{\partial p}{\partial x}+\rho_{eq}(\omega)\cdot j\omega u=0. \tag{C.7}$$

The EF-FDTD algorithm can be written as:

$$\begin{aligned} X(i,j,k)=\frac{1}{24}\Bigg[&-p^{n+\frac{1}{2}}\left(i+\frac{3}{2},j,k\right)+27p^{n+\frac{1}{2}}\left(i+\frac{1}{2},j,k\right)\\ &-27p^{n+\frac{1}{2}}\left(i-\frac{1}{2},j,k\right)+p^{n+\frac{1}{2}}\left(i-\frac{3}{2},j,k\right)\Bigg], \end{aligned} \tag{C.8}$$

$$\begin{aligned} u^{n+1}\left(i+\frac{1}{2},j,k\right)=&u^{n}\left(i+\frac{1}{2},j,k\right)-\frac{\Delta t}{\rho_e\Delta x}X(i,j,k)\\ &-\frac{\Delta t}{\rho_e}\sum_{l=1}^{N_1'}a_l'\cdot\left[{M_l}^{n}\left(i+\frac{1}{2},j,k\right)-{M_l}^{n-1}\left(i+\frac{1}{2},j,k\right)\right]\\ &-\frac{\Delta t}{\rho_e}\sum_{k=1}^{N_2'}X1_k'\cdot\left[{R_k}^{n}\left(i+\frac{1}{2},j,k\right)-{R_k}^{n-1}\left(i+\frac{1}{2},j,k\right)\right]\\ &+\frac{\Delta t}{\rho_e}\sum_{k=1}^{N_2'}X2_k'\cdot\left[{R_k}^{n-1}\left(i+\frac{1}{2},j,k\right)-{R_k}^{n-2}\left(i+\frac{1}{2},j,k\right)\right], \end{aligned} \tag{C.9}$$

$$\begin{aligned} {M_l}^{n+1}\left(i+\frac{1}{2}\right)&=u^{n+1}\left(i+\frac{1}{2}\right)+b_l'\cdot{M_l}^{n}\left(i+\frac{1}{2}\right)\\ l&=1,2\cdots N_1', \end{aligned} \tag{C.10}$$

$$\begin{aligned} {R_k}^{n+1}\left(i+\frac{1}{2}\right)&=u^{n+1}\left(i+\frac{1}{2}\right)+X3_k'\cdot{R_k}^{n}\left(i+\frac{1}{2}\right)-X4_k'\cdot{R_k}^{n-1}\left(i+\frac{1}{2}\right)\\ k&=1,2\cdots N_2'. \end{aligned} \tag{C.11}$$

References

[1] K.S.Yee, “Numerical solution of initial boundary value problems involving Maxwell’s equations in isotropic media”. IEEE Trans. Antennas Propag. 14, 302-307.(1966).

[2] G.Mur, “ Absorbing Boundary Conditions for the Finite-Difference Approximation of the Time-Domain Electromagnetic-Field Equations”. IEEE TRANSACTIONS ON ELECTROMAGNETIC COMPATIBILITY, VOL. EMC-23, NO.4,377-382(1981).

[3] T. Deveze, L. Beaulieu, W. Tabbara, “A forth order scheme for the FDTD algorithm applied to Maxwell’s equations”. IEEE Trans. Antennas Propag. 42, 346–349 (1992)

[4] K.S.Kunz and R.J.Luebbers, “The finite difference time domain method for electromagnetics”. CRC, Boca Raton, FL (1993).

[5] J.P. Berenger, “A perfectly matched layer for the absorption of electromagnetic waves”. J. Comput.Phys. 114, 185–200 (1994).

[6] M.F.Hadi and M.Piket, “A Modified FDTD (2,4) Scheme for Modeling Electrically Large Structures with High-Phase Accuracy”, IEEE TRANSACTIONS ON ANTENNAS AND PROPAGATION, Vol. 45, 254-264(1997).

[7] A. Taflove and S. C. Hagness, Computational Electrodynamics the Finite-Difference Time-Domain Method, 3rd ed. (Artech House Publishers, Boston, 2005).

[8] M. Sato, ‘‘Fundamental investigation of shear and surface elastic waves in soft biological tissues by numerical simulation,’’Jpn. J. Appl. Phys., 34 Part 1 (5B), 2808–2811 (1995).

[9] F. Iijima, T. Tsuchiya and N. Endoh, “Analysis of characteristics of underwater sound propagation in the ocean by a finite difference time domain method,” Jpn. J. Appl. Phys., 39 Part 1(5B), 3200–3204 (2000).

[10] O. Chiba and T. Kashiwa, “Analysis of sound fields in three dimensional space by the time-dependent finite difference method based on the leap frog algorithm”, J.Acoust.Soc.Jpn, 49, 551–562 (1993) (in Japanese).

[11] D.Botteldooren, “Acoustical finite-difference time-domain simulation in a quasi-Cartesian grid”, J,Acoust.Soc.Am. 95(5), 2313-2319 (1994).

[12] D.Botteldooren, “Finite-difference time-domain simulation of low-frequency room acoustic problems”, J,Acoust.Soc.Am. 98(6), 3302-3308 (1995).

[13] J. LoVetri, D. Mardare and G. Soulodre, ‘‘Modeling of the seat dip effect using the finite-difference time-domain method,’’ J.Acoust. Soc. Am., 100, 2204–2212 (1996).

[14] D.Botteldooren, “Vorticity and entropy boundary conditions for acoustical finite-difference time-domain Simulations”. J,Acoust.Soc.Am. 102(1), 170-178 (1997).

[15] J.D.Poorter and D.Botteldooren, “Acoustical finite-difference time-domain simulations of subwavelength geometries”, J,Acoust.Soc.Am., 104, pp:1171-1177 (1998).

[16] T. Yokota, S. Sakamoto and H. Tachibana, ‘‘Visualization of sound propagation and scattering in rooms,’’ Acoust. Sci. &Tech., 23, 40–46 (2002).

[17] Y. Yasuda, A. Ushiyama, S. Sakamoto and H. Tachibana, ‘‘Experimental and numerical studies on reverberation characteristics in a rectangular room with unevenly distributed absorbers,’’ Acoust. Sci. & Tech., 27, 366–374 (2006).

[18] S.Sakamoto, H.Nagatomo, A.Ushiyama, and H.Tachibana, “Calculation of impulse responses and acoustic parameters in a hall by the finite-difference time-domain method”, Acoust.Sci.Tech. 29, 256-265 (2008).

[19] M. Toyoda, D. Takahashi, “Prediction for architectural structure-borne sound by the finitedifference time-domain method”. Acoust. Sci. Tech. 30, 265–276 (2009)

[20] M. Toyoda, H. Miyazaki, Y. Shiba, A. Tanaka, D. Takahashi, “Finite-difference time-domain method for heterogeneous orthotropicmedia with damping”. Acoust. Sci.Tech. 33, 77–85 (2012)

[21] 木下隆志，石塚真一，“周波数特性に注目した音源配置とディジタルフィルタの最適設計手法”，日本音響学会春季研究発表会, pp.665-668, 2008.

[22] 鹿野洋，“FDTD 法における指向こ性合成を用いた室内音場解析”，修士論文, 2010.

[23] Yuuki Tachioka, “Boundary condition for finite-difference time-domain method using digital filters and efficient design of filter coefficients using equivalent mechanical system”, Acoust. Sci. & Tech. 33, 329-331 (2012).

[24] J.Escolano, F.Jacobsen, and J,Lopez, “An efficient realization of frequency dependent boundary conditions in an acoustic finite-difference time-domain model”, J.Sound Vib. 316, 234-237 (2008).

[25] H.Kuttruff, Room Acoustics, 4th ed. (Spon Press, London, 2000), pp.163-172.

[26] H.Suzuki, A.Omoto, and K.Fujiwara, “Treatment of boundary conditions by finite difference time domain method”, Acousti. Sci. Tech. 28, 16-26 (2007).

[27] H.Suzuki, A.Omoto, and K.Fujiwara, “ 有限差法における多孔質材料のモデル化手法に関する研究”, 日本音響学会講演論文集, 983-986 (2007).

[28] Yoh KANO, Sakae YOKOYAMA, Shinichi SAKAMOTO, Takeharu SASAOKA and Nobuya HATOU. “Sound field analysis on car cabin by the FDTD method -Application of extended reactive boundary”. SEISAN KENKYU. Vol.63, No.2, 119-124(2011).

[29] Yuuki Tachioka, Yosuke Yasuda and Tetsuya Sakuma. “Application of the constrained interpolation profile method to room acoustic problems: Examination of boundary modeling and spatial/time discretization”. Acoust. Sci. Tech. Vol.33, No.1, 21-32(2012).

[30] Nuno Ferreira, and Carl Hopkins, “ Using finite-difference time domain methods with a Rayleigh approach to model low-frequency sound fields in small spaces subdivided by porous materials”, Acoust. Sci. Tech. 34,332-341(2013)

[31] M.Biot, “The theory of propagation of elastic waves in a fluid-filled-saturated porous solid. I.Low-frequency range”, J. Acoust. Soc. Am. 28, 168-178 (1956).

[32] M.Biot, “The theory of propagation of elastic waves in a fluid-filled-saturated porous solid. II.Higher-frequency range”, J. Acoust. Soc. Am. 28, 179-191 (1956).

[33] A.Hosokawa. Simulation of ultrasound propagation through bovine cancellous bone using elastic and Biot's finite-difference time-domain methods. J. Acoust. Soc. Am. 2005. 118: 1782-1789.

[34] J.F.Allard and N.Atalla, “Propagation of sound in porous Media. Modeling sound Absorbing Materials”, Wiley, Chichester, UK (2009).

[35] Z. E. A. Fellah and C. Depollier, “Transient acoustic wave propagation in rigid porous media: A time domain approach,” J. Acoust. Soc. Am. 107,683–688 (2000).

[36] Z. E. A. Fellah and C. Depollier, “AN APPROACH TO DIRECT AND INVERSE TIME-DOMAIN SCATTERING OF ACOUSTIC WAVES FROM RIGID POROUS MATERIALS BY A FRACTIONAL CALCULUS BASED METHOD”. Journal of sound and vibration, 244(2),359-366(2001).

[37]Z. E. A. Fellah, C. Depollier, M. Fellah, “Application of Fractional Calculus to the Sound Waves Propagation in Rigid Porous Materials: Validation Via Ultrasonic Measurements”. ACTA ACUSTICA UNITED WITH ACUSTICA, Vol.88, 34-39(2002).

[38] Z. E. A. Fellah, M. Fellah, W. Lauriks, and C. Depollier, “Direct and inverse scattering of transient acoustic waves by a slab of rigid porous material,” J. Acoust. Soc. Am. 113, 61–72 (2003).

[39] Z. E. A. Fellah, A. Wirgin, M. Fellah, N. Sebaa, C. Depollier, and W.Lauriks, “A time-domain model of transient acoustic wave propagation in double-layered porous media,” J. Acoust. Soc. Am. 118, 661–670 (2005).

[40] R.F.Lambert, "The acoustical structure of highly porous open-cell foams". J. Acoust. Soc. Am. 72, 879-887 (1982).

[41] D.L.Johnsonn, J.Koplik and R.Dashen, "Theory of dynamic permeability and tortuosity in fluid-saturated porous media," J. Fluid Mech.176, 379-402.

[42] D.K.Wilson, "Relaxationa-matched modeling of propagation through porous media, including fractal pore structure", J.Acoust.Soc.Am. 94,1136-1145 (1993).

[43] D.K.Wilson, "Simple, relaxational models for the acoustical properties of porous material", Appl.Acoust. 50,171-188 (1997).

[44] D.K.Wilson, V.E.Ostashev, and S.L.Collier, "Time-domain equations for sound propagation in rigid-frame porous media", J. Acoust. Soc. Am. 116, 1889–1892 (2004).

[45] Olga Umnova and Diego Turo, "Time domain formulation of the equivalent fluid model for rigid porous media", J. Acoust. Soc. Am. 125, 1860–1863 (2009).

[46] D.Dragna, P.Pineau and P.Blanc-Benon, "A generalized recursive convolution method for time-domain propagation in porous media". J. Acoust. Soc. Am. 138, 1030–1042 (2015).

[47] Tetsuya Sakuma, Shinichi Sakamoto and Toru Otsuru, "Computational Simulation in Architectural and Environmental Acoustics, Methods and Applications of Wave-Based Computation", Springer Tokyo Heidelberg New York Dordrecht London, Springer Japan (2014).

[48] D.M.Sullivan, "ELETROMAGNETIC SIMULATION USING THE FDTD METHOD", IEEE Microwave Theory and Techniques Society, Sponsor (2000).

[49] D.M.Sullivan, "Frequency-Dependent FDTD Methods Using Z transform", IEEE Trans. Antennas Propag. 40, 1223-1230 (1992).

[50] D.M.Sullivan, "Z-Transform Theory and the FDTD Method", IEEE Trans. Antennas Propag. 44, 28-34 (1996).

[51] C.Zwikker and C.W.Kosten, sound absorbing materials (Elsevier, New York, 1949);as cited by Paulo Henrique Mareze, Rodrigo Pereira Becker, Arcanjo Lenzi, and Claudio Pellegrini, International Compressor Engineering Conference, 2012.

[52] D.L.Johnson, J.Koplik and L.M.Schwartz, "New pore size parameter characterizing transport in porous media". Phys. Rev. Lett., 57, 2564–2567(1986).

[53] D.L.Johnson, J.Koplik, and R.Dashen, "Theory of dynamic permeability and tortuosity in fluid-saturated media", J.Fluid Mech. 176, 379-402 (1987).

[54] Y. Champoux and J.F. Allard, “Dynamic tortuosity and bulk modulus in air-saturated porous media,” J. Appl. Phys. 70, 1975–1979 (1991).

[55] D. Lafarge, P. Lemariner, J.-F. Allard, and V. Tarnow, “Dynamic compressibility of air in porous structures at audible frequencies,” J. Acoust.Soc. Am. 102, 1995–2006 (1997).

[56] MATLAB documentation, contents, invfreqs.

[57] Levi, E.C, “Complex-Curve Fitting”. IRE Trans.on Automatic Control. Vol.AC-4,37-44(1959).

[58] Dennis, J.E., Jr., and R.B.Schnabel. “Numerical Methods for Unconstrained Optimization and Nonlinear Equations”. Englewood Cliffs, NJ:Prentice-Hall(1983).

[59] Jing Zhao, Ming Bao, Xiaolin Wang, Hyojin Lee and Shinichi Sakamoto. “An equivalent fluid model based finite-difference time-domain algorithm for sound propagation in porous material with rigid frame”, J. Acoust. Soc. Am., 143:130-138, (2018).

[60] Jing Zhao, Zhifei Chen, Ming Bao, Hyojin Lee and Shinichi Sakamoto. “Two-dimensional finite-difference time-domain analysis of sound propagation in rigid-frame porous material based on equivalent fluid model”, Applied Acoustics, 146:204-212(2019).

[61] H. W. Chang, C. J. Randall. Finite-difference time-domain modeling of elastic wave propagation in the cylindrical coordinate system. Proc. IEEE Ultrason. Symp., 397-402(1988).

[62] Hideo Utsunoa, Toshimitsu Tanaka, and Takeshi Fujikaw, “Transfer function method for measuring characteristic impedance and propagation constant of porous materials”, J. Acoust. Soc. Am. 86, 637-643 (1989).

[63]日本音響学会編，はじめての音響数値シミュレーションプログラミングガイド，コロナ社出版，日本(2009)

[64] L.L.Beranek, and H.P.Sleeper, “The design and construction of anechoic sound chambers”, J. Acoust. Soc. Am., 18, 140–150(1946).

[65] L.L.Beranek and H.P.Sleeper, “The Design of Anechoic Sound Chambers”. J. Acoust. Soc. Am., 18, 246 (1946).

[66] R.Berger and E.Ackerman, “The Construction of an Inexpensive Anechoic Chamber”, J. Acoust. Soc. Am., 26,145(1954).

[67] B.G.Watters, “Design of Wedges for Anechoic Chambers”, Noise Control, 4, 32(1958).

[68] J.Duda and A.Oppenheim, “Economic Design and Construction of Anechoic Chambers”, J. Acoust. Soc. Am., 34,737(1962).

[69] W.Koidan, G.R.Hruska and M.A.Pickett, “Wedge design for National Bureau of Standards anechoic chambers”. J. Acoust. Soc. Am., 52, 1071-1076(1972).

[70] A.Eckel, “Anechoic wedge design and development/anechoic chamber qualification testing”, J. Acoust. Soc. Am., 108,2472(2000).

[71] I.V.Belyaev, A.Yu.Golubev, A.Ya.Averev, S.Yu.Makashov, V.V.Palchikovskiy, A.F.Sobolev and V.V.Chernykh, “ Experimental Investigation of sound Absorption of acoustic wedges for anechoic chambers”. Applied Physics, Vol.61,606-614(2015).

[72] V.F.Kopiev, V.V.Palchikovskiy, Yu.V.Bersenev, S.Yu.Makashov, I.V.Belyaev, I.A.Korin, E.V.Sorokin, I.V.Khramtsov and O.Yu.Kustov, “Design and qualification of an anechoic facility in PNRPU”. Procedia Engineering, 176, 264-272(2017).

[73] V.Easwaran and M.L.Munjal, “Finite element analysis of wedges used in anechoic chambers”, Journal of Sound and Vibration, 160, 333–350(1993).

[74] C.N. Wang, and M.K.Tang, “Boundary element evaluation on the performance of sound absorbing wedges for anechoic chambers”. Engineering Analysis with Boundary Elements, 18: 103–110(1996).

[75] T.Kar and M.L.Munjal, “Plane wave analysis of acoustic wedges using the boundary-condition-transfer algorithm”. Applied Acoustics, 67,901-917(2006).

[76] J.S.Lee, Y.Y.Kim, J.S.Kim and Y.J.Kang, “Two-dimensional poroelastic acoustical foam shape design for absorption coefficient maximization by topology optimization method”. J. Acoust. Soc. Am., 123, 2094-2106(2008).

[77] Paolo Bonfiglio and Francesco Pompoli, “Numerical methodologies for optimizing and predicting the low frequency behavior of anechoic chambers”. J. Acoust. Soc. Am., 134, 285-291(2013).

[78] Changyong Jiang, Shangyu Zhang and Lixi Huang, “On the acoustic wedge design and simulation of anechoic chamber”. Journal of sound and Vibration, 381, 139-155(2016).

[79] ISO 10534-1-1996: Determination of sound absorption coefficient and impedance in impedance tubes -- Part 1: Method using standing wave ratio

[80] Jing Zhao, Zhifei Chen, Ming Bao, and Shinichi Sakamoto, “Prediction of sound absorption coefficients of acoustic wedges using finite-difference time-domain analysis”. Applied Acoustics, 155, pp:428–441 (2019).

[81] Y.Miki. Acoustical properties of porous materials-Modifications of Delany-Bazley models-. J.Acoust.Soc.Jpn. 1990. 11:19-24.

List of Publications

[1] Jing Zhao, Zhifei Chen, Ming Bao, and Shinichi Sakamoto, “Prediction of sound absorption coefficients of acoustic wedges using finite-difference time-domain analysis”. Applied Acoustics, 155, pp:428–441 (2019).

[2] Jing Zhao, Zhifei Chen, Ming Bao, Hyojin Lee and Shinichi Sakamoto. “Two-dimensional finite-difference time-domain analysis of sound propagation in rigid-frame porous material based on equivalent fluid model”, Applied Acoustics, 146:204-212, 2018.

[3] Jing Zhao, Ming Bao, Xiaolin Wang, Hyojin Lee and Shinichi Sakamoto. “An equivalent fluid model based finite-difference time-domain algorithm for sound propagation in porous material with rigid frame”, J. Acoust. Soc. Am., 143:130-138, 2018.

[4] 趙静, 李孝珍, 坂本慎一, “Treatment of FDTD analysis in porous materials using Z-transform”, 日本音響学会講演論文集, pp:1091-1092, 2016.3.

[5] 趙静, 李孝珍, 坂本慎一, “Finite-difference time-domain analysis on sound fields treated with porous materials using Z-transform”, 日本騒音制御工学会秋季研究発表会講演論文集, pp:223-226, 2015.9. (2015年日本騒音制御工学会研究奨励奨).

[6] 趙静, 林碩彦, 李孝珍, 坂本慎一, “In-situ measurement of absorption coefficients of road surface paved with drainage asphalt”,日本音響学会講演論文集, pp:1007-1008, 2014.9.

Acknowledgements

I would like to express my deeply gratitude to those people who have helped me to complete this dissertation.

It is really a long way and a hard time for me to complete this dissertation in the past 7 years. I experienced hope, joy, happiness, pain, disappointment, despair, and struggle in the past 7 years. Thanks to those who have helped me, I can finally complete this dissertation.

Firstly, I would like to express my gratitude to my advisor, Prof. Shinichi Sakamoto. With his valuable instructions and excellent guidance, I can finally complete the thesis. I also want to express my gratitude to all the members of Sakamoto Laboratory, for their kind advices and assistance.

I would like to express my gratitude to researcher Xiaodong Li and Ming Bao, who gave me the most assistance when I experienced the despair in my life. Without their support, I couldn't overcome the despair, and I may give up.

I also want to express my gratitude to Prof.Hong Hou, Prof.JianHua Yang and Prof.Ying Xu in Northwestern Polytechnical University. They give me a lot of valuable suggestions in the past 7 years.

I would like to express my gratitude to my friend, Prof. Ying Fu. She gave me the valuable suggestion in the most desperate moment of my life. Her suggestion changed my life.

I want to express my gratitude to Qingdao Branch of Institute of Acoustics, Chinese Academy of Sciences. They gave me a lot of assistance in the measurement.

I would like to express my love to my family. I want to express my love to my sister, Fang Zhao. Thank you for your support. I also want to express my love to my husband, Zhifei Chen. Thank you for your love, which is the best thing in my life. I especially want to express my deepest love to my daughter, QingYue Chen. Thanks for meeting you in this world, which is the luckiest thing in my life. Because of you, I want to complete this dissertation. Love you!